Homoclinic Snaking of Spatiotemporal Patterns in Reaction Diffusion Systems

by

Timothy Victor Roberts

B.Sc. (Adv Maths) (Honours), University of Sydney; Australia, 2018

A dissertation submitted in partial fulfillment of the

requirements for the degree of Doctor of Philosophy

in The Division of Applied Mathematics at Brown University

PROVIDENCE, RHODE ISLAND

May 2024

This dissertation by Timothy Victor Roberts is accepted in its present form by The Division of Applied Mathematics as satisfying the dissertation requirement for the degree of Doctor of Philosophy.

Date________________ ________________________________

Bjorn Sandstede, Ph.D., Advisor

Recommended to the Graduate Council

Date________________ ________________________________

Margaret Beck, Ph.D., Reader

Date________________ ________________________________

Govind Menon, Ph.D., Reader

Approved by the Graduate Council

Date________________ ________________________________

Thomas A. Lewis, Dean of the Graduate School

Vita

Education

Brown University, Providence, RI — MAY 2024
Ph.D. in Applied Mathematics
Adviser: Dr. Bjorn Sandstede

University of Sydney, NSW, Australia — MAY 2018
Bachelor Science (Advanced Mathematics)(Honours)
University Medal and Joye Prize in Mathematics

Research

AUG. 2020–*present* — **Brown University**
Snaking of defects in reaction diffusion equations. Established a rigorous framework for the prediction of snaking bifurcations of contact defects in (1+1)-dimensional reaction diffusion equations using spatial dynamical systems techniques.

AUG. 2022–*present* — **Brown University**
Existence of radially symmetric patterns in a model of amphiphilic copolymer self-assembly. Proved existence of radially symmetric patterns in a Cahn-Hillard model using geometric singular perturbation theory and found leading order expansions that describe qualitative feature of those solutions as system parameters are varied.

JAN. 2018–SEP. 2019 — **University of Sydney**
The Riccati-Evans function and stability of waves in a model of haptotaxis. Development of a numerical scheme for the computation of linear spectral stability of fronts and pulses using geometric techniques.

DEC. 2015- JAN. 2018 **University of Sydney**
Thermoregulation in a model of mammalian neurons. Determined the bifurcation structure governing the mechanism of thermoregulation in a model of mammalian neurons in the preoptic area and anterior hypthalamus.

Papers

Harley, K. E., Van Heijster, P., Marangell, R., Pettet, G. J., **Roberts, T. V.**, & Wechselberger, M. (2020). (In)stability of Travelling Waves in a Model of Haptotaxis. *SIAM Journal on Applied Mathematics*, 80(4), 1629–1653.

Papers in Preparation

Roberts, T. V., & Sandstede, B. "Snakes and Chutes: Snaking of contact defects in reaction diffusion equations".

Roberts, T. V., & Sandstede, B. "Snaking of source defects in reaction diffusion equations".

Carter, P., **Roberts, T. V.** "Rigorous existence of radially symmetric patterns in a model for amphiphilic copolymer self-assembly".

Teaching, Mentoring and Training

SUMMER 2021 **Instructor** for Brown University's undergraduate summer session
Primary instructor for introductory ordinary differential equations class (APMA0350). Developed syllabus, lectures and assessment.

FALL 2020- SPRING 2021 **Teaching Assistant** for Brown University
Prepared and held recitations, developed problem solving sheets and graded homework and exams for introductory Partial differential equations (APMA0360) and introductory statistics for non-concentrators (APMA0650).

JAN. 2017- NOV 2018	**Tutor** for University of Sydney Prepared and held tutorials, and graded homework and exams for six 1-semester long classes, including: first year calculus (MATH1901, 1003, 1021, 1023), second year vector calculus and differential equations (MATH2921), and third year partial differential equations (MATH3978).
SUMMER 2021	**REU Mentor** Grad Student mentor for a group of seven REU students working in the lab of Dr. Bjorn Sandstede.
FALL 2021- SPRING 2023	**Mentor** for the Applied Math Directed Reading Program Developed and mentored three undergraduate students through reading projects in dynamical systems and ordinary differential equations.
FALL 2020- SPRING 2021	**Teaching Certifications** at Brown's Sheridan Center Completed two certification programs at The Sheridan Center for Teaching and Learning. Certificates: The Sheridan Teaching Seminar - Reflective Teaching (Certificate I) and The Sheridan Course Design Seminar

Honors and Awards

2021-2022 SIAM Brown Student Chapter Certificate of Recognition	MAY 2022
SIAM Travel Award - SIAM Dynamical Systems 2021	MAY 2021
Honourable Mentions for the Von Neumann Prize at AustMS 2018	DEC. 2018
AustMS 2018 Student Support Scheme - Travel Award	DEC. 2018
Science Centenary Fund Supplementary Scholarship	JAN. 2018
Joye Prize in Mathematics	DEC 2017
K E Bullen Memorial Prize in Applied Mathematics	DEC 2017
The University of Sydney Academic Merit Prize	DEC 2017

The University of Sydney Honours Scholarship	JAN 2017
K E Bullen Memorial Scholarship No 1 in Applied Mathematics	DEC 2016
Dean's List of Excellence in Academic Performance	DEC 2016
The University of Sydney Academic Merit Prize	DEC 2016
Denison Mathematics and Statistics Summer Research Scholarship	NOV 2016
Dean's List of Excellence in Academic Performance	DEC 2015
The University of Sydney Academic Merit Prize	DEC 2015
Denison Mathematics and Statistics Summer Research Scholarship	NOV 2015
Dean's List of Excellence in Academic Performance	DEC 2014
The University of Sydney Academic Merit Prize	DEC 2014

Presentations

Roberts, T. V., & Sandstede, B. "Snaking of contact defects". **Boston University Dynamics Seminar**, September 25, 2023.

Roberts, T. V., & Sandstede, B. "Snaking of contact defects". **SIAM DS23 - Minisymposium 50**, May, 2023.

Roberts, T. V., & Sandstede, B. "Snaking of contact defects". **BIRS Workshop - 22w5057**, November, 2022.

Roberts, T. V., & Sandstede, B. "Snaking of contact defects in the Brusselator". **New England Dynamics Seminar**, November, 2022.

Harley, K. E., Van Heijster, P., Marangell, R., Pettet, G. J., Roberts, T. V., & Wechselberger, M. "Stability of Travelling Fronts by the Riccati-Evans Function". **SIAM DS21 - Minisymposium 100**, May, 2021.

Harley, K. E., Van Heijster, P., Marangell, R., Pettet, G. J., Roberts, T. V., & Wechselberger, M. "Using Geometry to Detect Stability: The Riccati-Evans Function". **SIAM DS19 - Minisymposium 158**, May, 2019.

Harley, K. E., Van Heijster, P., Marangell, R., Pettet, G. J., Roberts, T. V., & Wechselberger, M. "(Un)Stable (non)physical waves in a model of tumour invasion". **AustMS 2018 - Special Session for Dynamical Systems and Ergodic Theory**, December, 2018.

Roberts, T. V., & Wechselberger, M. "Neurons, temperature and timescales". **ANZIAM - Contributed Talk**, Febuary, 2018.

Service

Graduate Faculty Liaison for the Division of Applied Math	SUMMER 2022 - SPRING 2024
President, Brown's SIAM Student Chapter	FALL 2022 - SPRING 2024
Organiser, Brown Mathematical Competition for Modelling	FALL 2021 - FALL 2023
Organiser, Graduate Student Seminar	FALL 2021 - FALL 2023
Organiser, Applied Math Directed Reading Program	SPRING 2021 - SPRING 2024
Lead Organiser, Applied Math Graduate Student Retreat	Fall 2022
Vice-President, Brown's SIAM Student Chapter	FALL 2021 - SPRING 2021

Professional Organizations

Society for Industrial and Applied Mathematics

Graduate Course Work

Recent Applications of Probability and Statistics
Graphs and Networks
Interacting Particle Systems
Algebraic Topology
Nonlinear Dynamical Systems
Numerical Solutions to Partial Differential Equations
Theory of Probability
Real and Functional Analysis

Dedication

To my Grandmother, for giving me my first maths book all those years ago.

Preface and Acknowledgments

To my advisor, Bjorn Sandstede. Thank you for all your time and effort. Through your mentorship, conversation and example, there is no doubt I leave Brown a more capable, knowledgeable and experienced mathematician. Thank you for pushing me to succeed and for your guidance as I move into the next stage of my career. But also, thank you for your professional support. All of our discussions, your assistance in my service to the APMA community, and your support of my teaching have been extremely valuable in my development as a professional and a person.

To my committee members Margaret Beck and Govind Menon. Thank you for your patience and your feedback, it is greatly appreciated.

To my fellow fitness astronauts, Gina Grosso, Becky Durst and Meg Wilson. Thank you for being my surrogate family in the US, and making the pandemic slightly more bearable.

To Katie Slyman. Thank you for your job application advice and proof reading so many pages. I'm certain you helped my get my job.

Finally to my office mates, friends and colleagues in the Division of Applied Math. It has been a long and wild ride. Good luck with your studies and whatever comes next for you.

Contents

List of Figures

Chapter One

Introduction

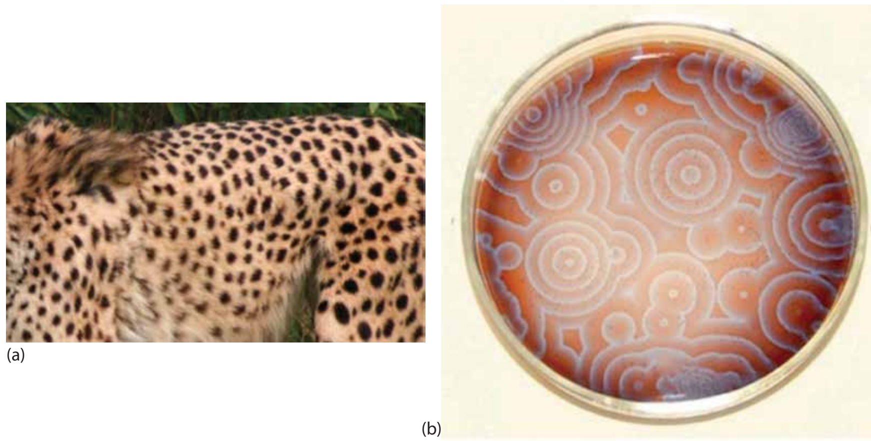

Figure 1.1: Real life examples of spatiotemporal patterns. Photos from Ball (2015). (a) Spots on the coat of a cheetah. (b) Target waves forming in the BZ chemical reaction.

1.1 Motivation - Target and Spiral Patterns

An interesting and pervasive feature of biological and physical models is the formation and interaction of spatiotemporal patterns. For us, patterns are the regular and repeating arrangements of populations in time and space. This might be very simple, such as the spots on the coat of a cheetah as seen in Figure 1.1(a), which are stationary in time. Or they might be more complex, such as target waves in the chemcial reaction seen in Figure 1.1(b). Here the target patterns, formed by outwardly propagating concentric circles are dynamic in time. In either case, there are many questions you could ask about such patterns. How do they form? Are they temporally stable? How do they interact? How do they behave on a growing domain, like the coat of a growing cheetah? Or, many others. Here we will be interested in two particular types of patterns: targets and spirals, which appear and interact in many physical problems driven by diffusion.

A key example being the electrochemical potential in the heart of mammals. In order to pump blood through the body, the muscles of the heart contract in sequence

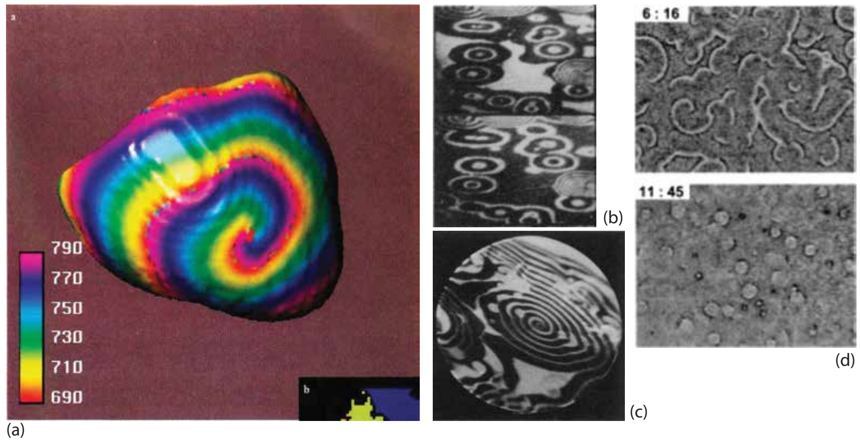

Figure 1.2: Computational and experimental examples of spirals and targets. (a) Computational model of a heart in reentrant tachycardia (Glass, 1996). (b)-(c) Target and spiral waves in oxidation patterns on platinum crystals (Ertl, 1991). (d) Spiral and target waves in populations of slime mold (Lee et al., 1996).

coordinated by a periodic electrical stimulus, or pacemaker potential. When viewed on the surface of the heart this pacemaker takes the form of a target wave - with outwardly propagating concentric circular rings emanating from a core region, in this case the sinus node of the heart (Cross and Hohenberg, 1993). It is possible that this typical behaviour becomes interrupted, leading to severe disease such as tachycardia or fibrillation. An example of this is reentrant tachycardia where damaged heart tissue distorts the pacemaker potential forming spiral patterns (Glass, 1996), see Figure 1.2(a). Similar interactions between target and spiral patterns have been observed in other excitable media such as reproduction and propagation of *Dictyostelium discoideum* amoebae populations (Lee et al., 1996, Lee, 1997) (Figure 1.2(d)) and in oscillatory media such as the oxidation of carbon monoxide on a surface of platinum (Ertl, 1991) (Figure 1.2(b)-(c)). Understanding of the existence, stability, selection and interaction of these patterns is a fascinating and complicated story, which is not fully understood. However, here we aim to add to the understanding of the existence of these patterns in reaction-diffusion systems.

1.2 Reaction Diffusion Equations and Defect Solutions

Throughout this work we will concentrate on reaction-diffusion equations

$$u_t = Du_{xx} + f(u) \tag{1.2.1}$$

where the dependent variable $u = u(x,t)$ takes values in $\mathbb{R}^2$ and is a function of two independent variables $x \in \mathbb{R}^d$ representing space and $t \in \mathbb{R}$ representing time. D is a 2×2 diagonal matrix with strictly positive entries and $f : \mathbb{R}^2 \to \mathbb{R}^2$ is a sufficiently smooth reaction term.

Our prototypical example will be the Brusselator

$$U_t = DU_{xx} + E - (B+1)U + VU^2 \tag{1.2.2}$$

$$V_t = V_{xx} + BU - VU^2 \tag{1.2.3}$$

which has a long and storied history and has been the subject of extensive mathematical study since its development following the work of Turing (1997). In 1952, Turing proposed a mechanism whereby a coupling between temporal activator-inhibitor dynamics and spatial diffusion can produce spatial patterns. Although it would be almost forty more years until the first experimental examples of such patterns would be found in chemical reactions (Epstein, 1991), Turing's ideas would go on to establish the mathematical foundation for studying biological morphogenesis or pattern formation.

The Brusselator is a system of equation representing a theoretical chemical reaction that would provide one of the first analytically tractable examples to study both temporal and spatial bifurcations simultaneously. In a review of results on this system of equations, Tyson (2003) names it the Brusselator after the group of mathematicians at *Université libre de Bruxelles* who proposed and investigated the system initially. Nicholis, a member of this school, and Auchmuty described the Brusselator as: "the simplest stoichiometric reaction which has instability on the thermodynamic branch" and consequently "may be considered as a prototype of any system leading to dissipative structures in a manner analogous to the role of the harmonic oscillator as a prototype in classical or quantum mechanics" (Auchmuty and Nicolis, 1975). In modern language this means the simplest set of equations arising from a chemical reaction that undergoes a Turing bifurcation. While it has not necessarily maintained this status in the minds of mathematicians, it nevertheless does display many of the fundamental properties of pattern formation still under investigation to this day.

Our interest in reaction-diffusion equations (and the Brusselator) is their prevalence as continuous, deterministic models of diffusive processes and the ubiquity of biological, physical and chemical systems driven by diffusive dynamics. Moreover, a key feature of these models is their ability to form spatial patterns - including target and spiral waves. These waves are fundamental point defect patterns found on two-dimensional spatial domains (Cross and Hohenberg, 1993), and at least heuristically, behave exactly as they sound. Target patterns or target waves, as we have seen already, consist of outwardly propagating concentric circles originating at a central point. Spiral waves are similarly generated from a single point in the plane, but instead produce a fixed spiral pattern which rotates rigidly over time. See Figure 1.3.

There is a lot more to say about these patterns, and over the last decade we

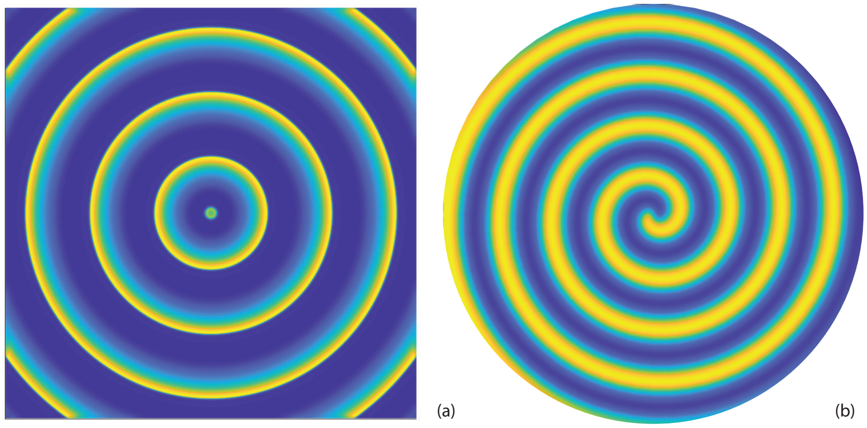

Figure 1.3: Numerical solutions of reaction diffusion equations on the plane. (a) Target waves in the Brusselator which propagate outward over time. (b) Spiral waves in the Rossler model which rotate clockwise over time. Generated by code from Dodson and Sandstede (2019).

have learned much about their properties, instabilities and bifurcations (Sandstede and Scheel, 2023). However, the study of patterns in two spatial dimensions remains difficult, and there are many open problems in existence, stability, selection and interaction of these patterns. So instead of giving a precise definition of them here, we instead look at simpler patterns in one spatial dimension which can be thought of as their one-dimensional analogue.

One-dimensional defect solutions, or defects as we will call them from now on, can be formed from their two-dimensional spiral and target wave counterparts. Imagine drawing a straight line cross-section through the centre of the target wave in Figure 1.3(a). Doing so we see a core region, corresponding to the point defect of the target pattern, separating outwardly propagating wavetrains, see Figure 1.4. Given the radial symmetry of the target waves, these wavetrains must be generated simultaneously on each side of the core, and propagate away at the same speed[1]. We can similarly find a different type of defect by looking at the cross-section of the spiral wave in Figure 1.3(b). In this case we again find a central core region

[1] Add a discussion of space time diagrams here

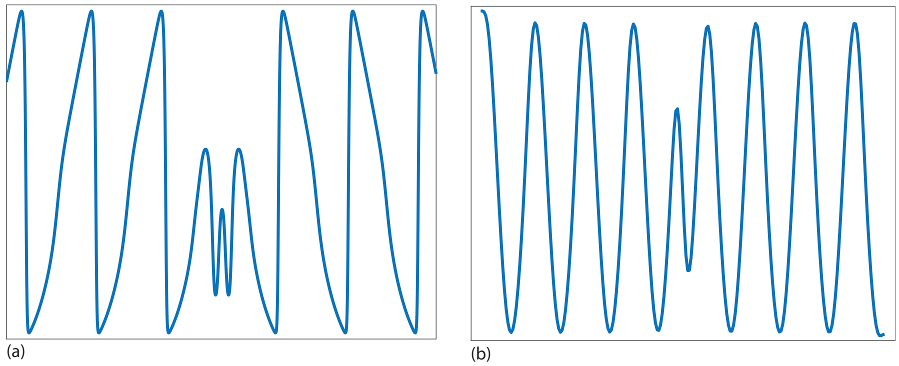

Figure 1.4: Defect solutions corresponding to the 2d patterns in Figure 1.3. (a) Target Defect - in phase background oscillations. (b) Spiral Defect - out of phase background oscillations.

representing the original point defect, however, as the spiral waves are not radially symmetric but formed by rotation of the spiral arm, the wavetrains are generated asynchronously, although they will again propagate away at the same speed. We call these one-dimensional patterns defects as they can be described as a localised interface separating different wavetrains. What defines spirals and targets as special cases of defect solutions is that the asymptotic wavetrains propagate at the same speed and are either in-phase (for targets) or out-of-phase (for spirals). A precise mathematical description of these patterns can be found in Chapter 3.

This reduction from two-dimensional spirals and targets to one-dimensional defects is not an act of mathematical fancy. These one-dimensional analogues have been found in experimental settings. For example the Chlorine-Iodide and Malonic Acid (CIMA) reaction (which was in fact the first chemical system found to exhibit Turing patterns (Epstein, 1991)) was demonstrated to produce one-dimensional spirals when experiments are conducted in the right way (Perraud et al., 1993). Moreover, the authors of this study observe that one-dimensional defect solutions of the Brusselator are a natural starting point for the modelling of these experimental results.

In the remainder of this chapter we explain the starting point of our investigation into the existence and bifurcation of defects in reaction-diffusion systems. We will then give a heuristic summary of the main results of this thesis concerning the snaking bifurcation of defect solutions. We will see that, while simpler than their two-dimensional counterparts, the behaviour of one-dimensional defects is extremely rich and their study requires a very careful and nuanced approach.

1.3 Starting Point - Numerical Observations

We turn our attention to the formation of certain 1-d targets and spirals in reaction diffusion systems. Recent numerical work by Tzou et al. (2013) studying the Brusselator observed the formation of target patterns via a snaking bifurcation. In the Brusselator there is a bistability between Turing (temporally constant, spatially oscillatory) and Hopf (spatially constant, temporally oscillatory) modes due to the presence of a codimension-2 Turing-Hopf bifurcation (Kidachi, 1980). Examination of this codimension-2 point show that the interaction between the Hopf and Turing modes allows for the production of more complex solutions such as mixed-mode oscillations. The work by Tzou et al. provides numerical evidence that in this region of parameter space we can also find a large number of defect solutions which organise themselves into a single coherent bifurcation diagram reminiscent of a snaking bifurcation. That is, the bifurcation curves corresponding to defect solutions wind backward and forward through a tower of saddle-node bifurcations. A segment of the bifurcation diagram they found is shown in Figure 1.5.

The term snaking bifurcation refers to a process in ordinary differential equations whereby a heteroclinic cycle between a background state equilibrium and a reversible

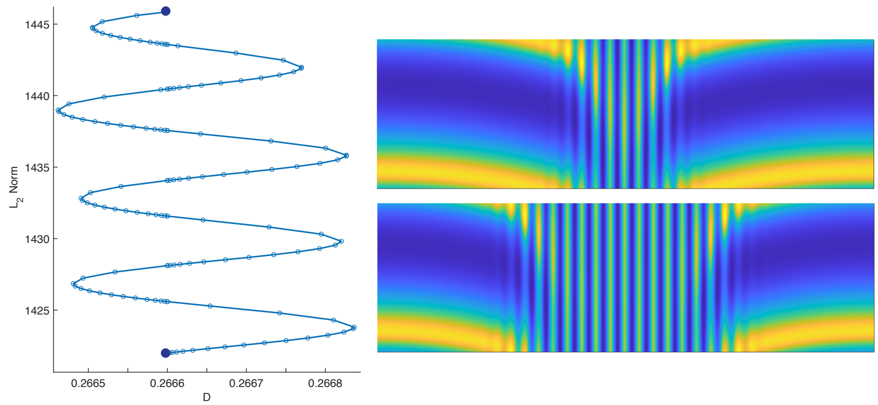

Figure 1.5: A small segment of the bifurcation diagram discovered by Tzou et al. (2013) in which one-dimensional targets are shown to snake. The two defect solutions are from the points indicated on the snaking diagram.

periodic orbit generates families of nearby homoclinic connections to the equilibrium. The word "snaking" was chosen to describe the characteristic feature of the bifurcation diagram where two branches of symmetric homoclinic solutions synchronously wind backward and forward. As you move up the diagram (across saddle-nodes), the core region expands as the homoclinic remains in transit of the periodic orbit for an additional period. These bifurcations have been found and studied extensively in the context of spatially localised patterns in both 1 and 2 dimensions (Beck et al., 2009). In this context it has been shown that the primary symmetric branches are connected by secondary branches of asymmetric solutions which act like rungs of a ladder. A summary of snaking phenomena for localized solutions can be found in Chapter 2.

This is partially what Tzou et al. (2013) observe in their numerics. They find a one-dimensional bifurcation curve of symmetric defect solutions which wind between saddle-node bifurcations. The defects are symmetric in the sense that they have even symmetry at the origin. As you traverse the bifurcation diagram, in particular moving across saddle-nodes, you gain stripes in the inner core region. However unlike the case of localised patterns, they were unable to find the corresponding asymmetric branches.

Our aim is then to prove, under certain general assumptions, that reaction diffusion systems exhibit snaking of contact defects. Our results show that the snaking phenomenon found in this new context is more complicated than its classical counterpart. We demonstrate that, in addition to the symmetric solutions found by Tzou et al. (2013), there exist a large number of asymmetric solutions which are note found in the theory of snaking for temporally stationary patterns. Simultaneously we wish to extend current numerical approaches (Morrissey and Scheel, 2015, Lloyd and Scheel, 2017) to numerically study this snaking diagram in the Brusselator. Although it should be stressed that producing a numerical scheme for the continuation of these patterns is a significant challenge.

1.4 Main Results

In this thesis we provide a rigorous framework describing the existence and continuation of contact defects that undergo snaking bifurcations. We can state our results explicitly for the Brusselator as follows.

Hypothesis 1.4.1. Suppose there exists a smooth function $(z, \kappa^*) : S^1 \to J \times K$ such that for every $\mu{=}z(\varphi)$ in J, there exists a front solution to the Brusselator for diffusion ratio $D = \mu$ which is asymptotic in forward time to the Turing pattern with wavenumber $\kappa^*(\varphi)$ and asymptotic in backward time to the spatially homogeneous oscillation. Furthermore, we assume that this bifurcation family of fronts satisfies genericity conditions corresponding to the transversality and general position of the stable and unstable manifolds of the Turing pattern and homogeneous oscillations respectively.

The formulation of the these genericity conditions is difficult, and a full account of these is given in Chapter 3. Assuming these conditions hold we prove the following two theorems.

Theorem 1.4.2 (Snaking of Symmetric Defects)**.** *Assume Hypothesis 1.4.1 holds. Then there exists $N \in \mathbb{Z}$ and $\eta > 0$ such that, for every integer $n > N$, and phases $\alpha, \varphi_0 \in \{0, \pi\}$, there exists a unique contact defect solution with core width $L = (2\pi n + \varphi_0 - \varphi)/\kappa^*(\varphi) + \mathcal{O}(e^{-\eta n})$ and phase offset α for the parameter value $\mu = z(\varphi) + \mathcal{O}(e^{-\eta n})$.*

Theorem 1.4.3 (Snaking of Asymmetric Defects)**.** *Assume Hypothesis 1.4.1 holds. Then there exists $N \in \mathbb{Z}$ and $\eta > 0$ such that, for every $n > N$, phase $\alpha \in S^1$, and pairs of phases $(\varphi_1, \varphi_2) \in S^1 \times S^1$ where $z(\varphi_1) = z(\varphi_2)$, there exists a unique contact defect with background phase offset α and core width*

$$L = \frac{2\pi n - (\varphi_1 + \varphi_2)}{\kappa^*(\varphi_1) + \kappa^*(\varphi_2)} + \mathcal{O}\left(\frac{\Delta\kappa}{n} + e^{-\eta n}\right) \tag{1.4.1}$$

where $\Delta\kappa = \kappa^*(\varphi_1) - \kappa^*(\varphi_2)$. Moreover, these defects move at a wavespeed $c = \mathcal{O}(\Delta\kappa/n + e^{-\eta n})$, have temporal frequency $\omega = \omega_0 + \mathcal{O}(c^2)$ and connect background wavetrains with spatial wavelengths $k = \mathcal{O}(c^2)$.

We give a qualitative description of these results in the following section, along with the critical intuition through which we can understand them.

These results provide substantial contributions to the areas of homoclinic snaking and spatial dynamical systems. These are the first rigorous, theoretical results pertaining to snaking in infinite-dimensional problems. In particular, the formulation of transversality and general position assumptions becomes complicated and nuanced. However, the main difficulty is not actually in the infinite-dimensional nature of the problem, but the new geometry due to the presence of additional symmetries. As such, while we can use similar arguments to known proofs of snaking in finite-dimensional problems, there are essential differences that much be overcome. The symmetries also fundamentally change the nature of the bifurcation results, and this is the first work to determine the existence of defect solutions with arbitrary phase offsets in their background oscillations. Finally, our results are also far more general than just the case of varying the diffusion ratio in the Brusselator. In Chapter 3 we prove results for a much larger class of reaction diffusion equations that satisfy a set of minimal assumptions. Theorems 1.4.2 and 1.4.3 are then corollaries to Theorems 3.2.1 and 3.2.2 respectively.

1.5 Intuition and Discussion

The challenge in building a rigorous framework to describe the existence and snaking of defects observed by Tzou et al. (2013) is in reconciling two perspectives from disparate areas of dynamical systems: homoclinic snaking and spatial dynamical systems. In this section we will discuss the heuristic arguments provided by these areas, and how they can be resolved. In doing so we will describe the main results of this thesis, which constitute new and highly non-trivial results in the literature of pattern formation and spatial dynamical systems.

Note that the solutions found by Tzou et al. (2013) are combinations of Hopf and Turing modes. As observed above, the Brusselator has a codimension-2 Turing-Hopf bifurcation (Kidachi, 1980): i.e. a point in parameter space at which a Turing and

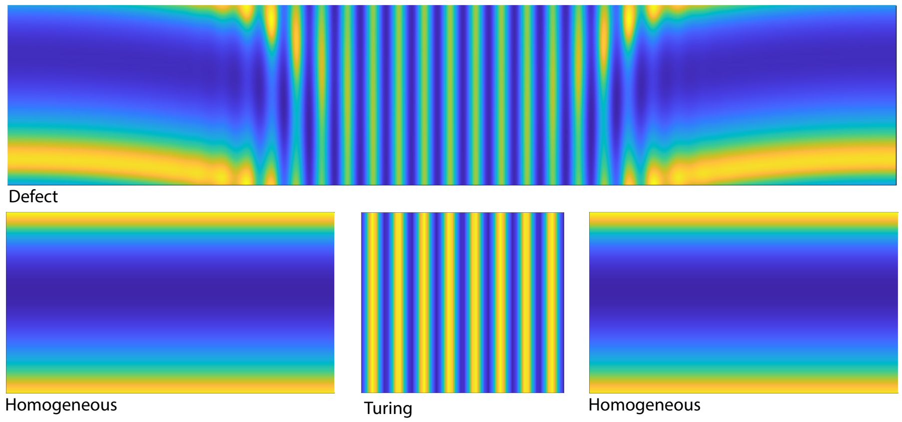

Figure 1.6: Defect solutions of the Brusselator as connections between Hopf and Turing modes.

Hopf bifurcations occur at the same time. As such there are regions in parameter space where there is a bistability between a Hopf mode (spatially homogeneous temporal oscillation) and a Turing pattern (temporally homogeneous spatial oscillation). This allows for the existence of mixed states, which are combinations or superpositions of these two different types of oscillations. In fact our defects are formed by connecting Hopf modes in the background with a Turing pattern core, see Figure 1.6.

Looking at the space-time plots for these defect solutions, we see that the number of "stripes" of the Turing pattern can be chosen arbitrarily in the snaking parameter range. We want to study this problem by analogy to the theory of homoclinic snaking for localized solutions to PDEs.

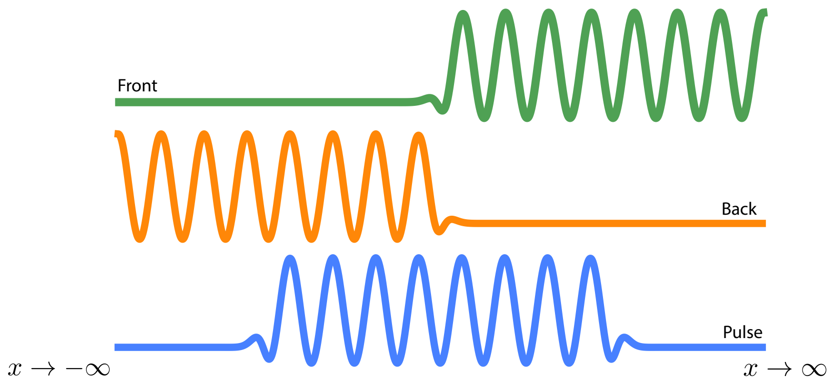

Figure 1.7: Localised pulse solutions of the Swift-Hohenberg equation are formed by gluing fronts and backs.(a) Front solution. (b) Back solutions. (c) Localised pulse.

1.5.1 Homoclinic Snaking and Gluing Fronts

Consider, for example, the quadratic-cubic Swift-Hohenberg equation

$$\partial_t U = -(1 + \partial_x^2)^2 U - \mu U + \nu U^2 - U^3 \tag{1.5.1}$$

where U is a scalar function for $t \geq 0$ and $x \in \mathbb{R}$. For the right choices of parameters μ, ν, this equation has stationary solutions which look very similar to our defects in the Brusselator, see Figure 1.7(a). Indeed they look like the rest state zero has been glued on either side to a spatially periodic core region of "stripes". Moreover, we can use this description to argue heuristically that we should expect to find the corresponding roll solutions. Suppose that we assume the existence of some special solutions called fronts and backs, shown in 1.7(b). By choosing which maxima or minima to glue together we can produce a discrete family of functions which have an arbitrary number of stripes in their core which are reminiscent of the roll solutions.

We cannot chop up existing solutions and expect that gluing them together will form solutions of the underlying PDE, however by using a dynamical systems perspective we can find new solutions to the PDE which are small perturbations of the glued functions. As we are looking for stationary solutions, the time derivative of (1.5.1) is zero and we have an ODE on a 4-dimensional phase space. In that case, the front and back solutions form a heteroclinic cycle between the rest state zero and a periodic orbit. We can use established theory to find nearby homoclinic orbits to the rest state zero which are our rolls, with the number of stripes determined by the number of times the homoclinic orbit transits the periodic orbit.

As a result, the existence of the front and back solutions imply the existence of the homoclinic rolls. A further global assumption on how the front and back continue as a bifurcation parameter, say μ, is changed then gives the existence of one-dimensional curves of symmetric rolls. It is also possible to find additional asymmetric rolls. These rolls have a core which is not centered on a maxima or minima, meaning the rolls do not have even symmetry. A more detailed formulation of this is given in Chapter 2.

We can take a similar perspective in our problem for the Brusselator. We assume the existence of fronts and backs which are the analogous heteroclinic connections between the background Hopf mode and the core Turing pattern. However, unlike the case of the Swift-Hohenberg, we do not have a simplification to an ODE, and hence no finite-dimensional phase space. To overcome this we need to consider the spatial dynamics of reaction diffusion equations, allowing us to consider dynamics on infinite-dimensional phase spaces. Also of interest is that the existing numerics do not give us any evidence for the existence of asymmetric solutions as predicted by this framework.

1.5.2 Spatial Dynamics of Reaction-Diffusion Equations and Defects

The idea from the previous section, of looking at the reaction diffusion system as a dynamical system on the right phase space and analysing our defects as hetero- and homoclinic connections on this space, is very tempting. Indeed, as always we can reduce our second order reaction diffusion equation (1.2.1) as a system first order in space

$$\begin{aligned} u_x &= v, \\ v_x &= D^{-1}(u_t - f(u)). \end{aligned} \tag{1.5.2}$$

Of course, as already noted our solutions of interest are time-periodic (not stationary) and the time derivative cannot be removed. However, looking at our defects in Figure 1.5 we note that for each fixed value of x the profile is a periodic function of a fixed period T uniform in x. Moreover, the front and back solutions are heteroclinic connections in the sense that they are asymptotic in space to the Hopf and Turing solutions. Rescaling the period to be 2π, we consider this as a dynamical system in the variable x where time dependence is captured entirely in the phase space $X = H^{1/2}_{per}(S^1, \mathbb{R}^2) \times L^2_{per}(S^1, \mathbb{R}^2)$ where $S^1 = \mathbb{R}/2\pi\mathbb{Z}$, which is infinite-dimensional. In such a set up, and ignoring technical details for now, we have an exact generalisation of the gluing formulation of the Swift-Hohenberg equations.

Defect solutions have also been studied extensively from this perspective, see for example Sandstede and Scheel (2004). In particular, the robustness properties of defect solutions are well known. It turns out that the existence and robustness of defects depends a lot on certain properties of their asymptotic wavetrains. For now, the important detail in our framework is that defects like those shown in Figure 1.5 are contact defects, and contact defects generically exist in 1-parameter families parameterized by the spatial wavenumber of their background oscillations for any fixed values of their system parameters. That is, for fixed bifurcation parameters, we should see 1-parameter families of defect solutions and not the discrete families observed in the existing numerics or in finite-dimensional homoclinic snaking.

1.5.3 Symmetries and Chutes

From the previous sections, we conclude that the bifurcation diagram in the existing numerics is incomplete. It should include branches of asymmetric solutions and the branches themselves are an entire dimension smaller than we expect for contact defects. The resolution of this is that we are missing many asymmetric solutions. But unlike the case of homoclinic snaking, there is more than one way to be asymmetric.

To see this we consider a transformation of our solutions that is very nearly a symmetry operation. Suppose we take the defect in Figure 1.8(a) and cut it down the line $x = 0$. By translating only the right-hand side forward in time we produce a new profile with out-of-phase background oscillations. Since the Turing patterns are temporally homogeneous and we have a large number of Turing stripes in this solution, this transformation has not significantly changed the core region. So it is reasonable to ask: is this new profile also a defect solution to the Brusselator? As with our previous gluing arguments the answer is no. However, our analysis in Chapter 3 will show these are very close to actual solutions with the given phase offset. In fact, it is possible to create contact defects with any phase offset $\alpha \in S^1$. Unlike their symmetric counterparts, however, these defects will move at a small wavespeed c in the laboratory frame - for reasons we will describe below.

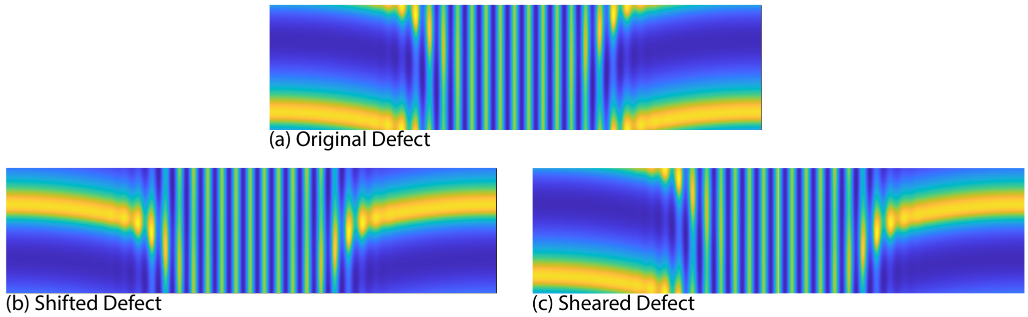

Figure 1.8: (a) A contact defect with in-phase background oscillations. (b) The same defect translated in time. (c) A shear shift of the defect in (a) by $\alpha = \pi/2$.

Theorems 1.4.2 and 1.4.3 predict a snaking bifurcation diagram as shown in Figure 1.9. The symmetric defects form 1-dimensional curves parameterised by the bifurcation parameter as seen in Figure 1.5. However, there are four such curves, with two corresponding to 1-dimensional targets and the others to 1-dimensional spirals. Two of these curves are shown as the symmetric and antisymmetric states in Figure 1.9. These symmetric defects are are also accompanied by a circle of defects parameterised by their phase offset. The cylindrical families of solutions interpolate between these states, with each asymmetric state possibly moving at a nonzero wavespeed c in the laboratory frame.

In addition, we also find the asymmetric branch of solutions predicted by homoclinic snaking. These defect solutions are asymmetric in a different way - they have an asymmetric core, like in the classical case. Again these solutions come in cylindrical families where the circular cross-sections are parameterised by the phase offset in background oscillations. These solutions also move at a small wavespeed in the laboratory frame, with the wave speed determined by both the background phase offset and by a parameter measuring the asymmetry of the core.

One problem remains in this explanation: generically contact defects come in 1-parameter families parameterised by the spatial wavenumber of their asymptotic

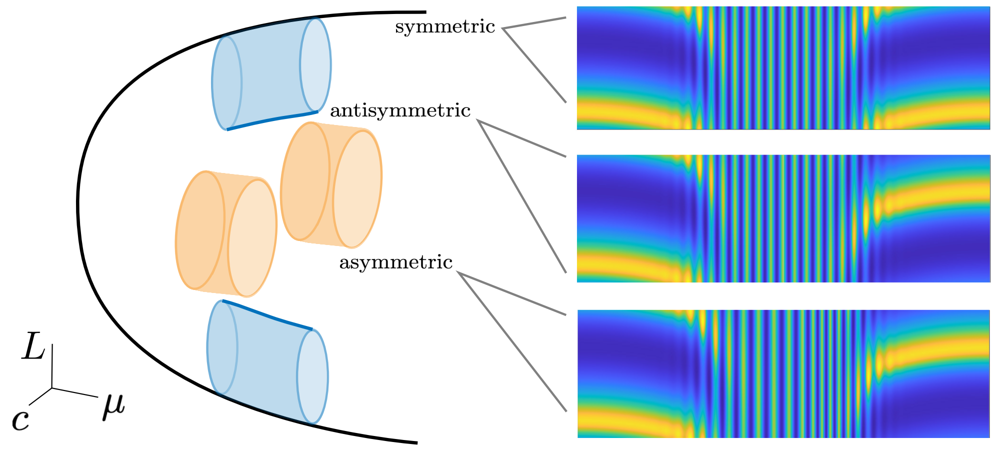

Figure 1.9: A pictorial bifurcation diagram of the Chutes Bifurcation of contact defects away from the saddle-nodes. The third axis c is the wavespeed of the defect in the laboratory frame. Symmetric (target) and anti-symmetric (spiral) defects will be stationary. The other phase offsets then interpolate between these two states forming cylindrical families.

wavetrains. However, in the above we have described the 1-parameter families as parameterised by the phase offset $\alpha \in S^1$. In fact, there is a direct relationship between the background phase offset and the asymptotic spatial wavenumber via the small wavespeed of the oscillations. In order to produce defect solutions with an offset we must allow the defects to move at a small speed. This is to allow modulation of the Turing wavenumber inside the core region. At the same time, for our defects to remain contact defects, this breaks the homogeneity of the background oscillations. They are now legitimate wavetrains which have a small spatial wavenumber. As such, there is a direct correspondence between the phase offset and the asymptotic spatial wavenumber. For more details, see Chapter 3.

1.6 Outline of Thesis

The thesis is organised as follows. In Chapter 2 we give a brief account of the theory for homoclinic snaking of localised patterns. Here we will describe the existence and bifurcation of stationary pulses in model equations such as the Swift-Hohenberg equation that display snaking. We will see that the basic ingredients for snaking are reversibility and the existence of heteroclinic connections, and that the snaking diagram itself can be described qualitatively and quantitatively by a global property of those heteroclinic connections. We will also demonstrate a simple version of the numerical scheme we propose to study contact defects in the Brusselator.

Our main results will then be laid out in full detail in Chapter 3. Here we describe the existence of defect solutions and how global assumptions lead to the formation of snaking bifurcations. This includes necessary spatial dynamical systems background to understand defect solutions, and in particular, contact defect solutions. Along side this, we will propose an extension of the Core-Far Field decomposition to study snaking of contact defects in the Brusselator.

Finally Chapter 4 will discuss avenues for ongoing work, and what further challenges await in understanding snaking for other kinds of defect solutions.

Chapter Two

Homoclinic Snaking of Localized Solutions

2.1 Introduction

Homoclinic snaking refers to a phenomenon in ordinary differential equations where a heteroclinic cycle gives rise to nearby homoclinic orbits. These homoclinic orbits are transverse in general, meaning they can be continued in a bifurcation parameter and form very distinct bifurcation diagrams.

A key example of this behaviour can be found for stationary solutions of the quadratic-cubic Swift-Hohenberg equation:

$$\partial_t U = -(1+\partial_x^2)^2 U - \mu U + \nu U^2 - U^3, \tag{2.1.1}$$

where U is a scalar function and for simplicity we take $t, x \in \mathbb{R}$.

In this case, homoclinic snaking is a property of particular exponentially localized solutions which are stationary in time. These solutions consist of a small patch of stationary spatial oscillations sitting on a homogeneous background corresponding to the rest state zero. For an illustration see the PDE profiles in Figure 2.1. When continued in the bifurcation parameter μ, the bifurcation diagram shows some surprisingly complex but predictable structure. First there are two branches of symmetric solutions which wind backward and forward between infinite towers of saddle-node bifurcations. Here symmetric refers to the face that they have even $x \mapsto -x$ symmetry, which will be explained later in the Chapter. The two branches, which wind out of phase to one another, correspond to localized solutions expressing the two possible configurations which satisfy the symmetry condition: a local minimum or a local maximum at the origin. In Figure 2.1, we see that panel (i) has symmetric branches with a local maximum and local minimum at the origin. In panel (ii) we see that as you move up the diagram, the width of the patterned region

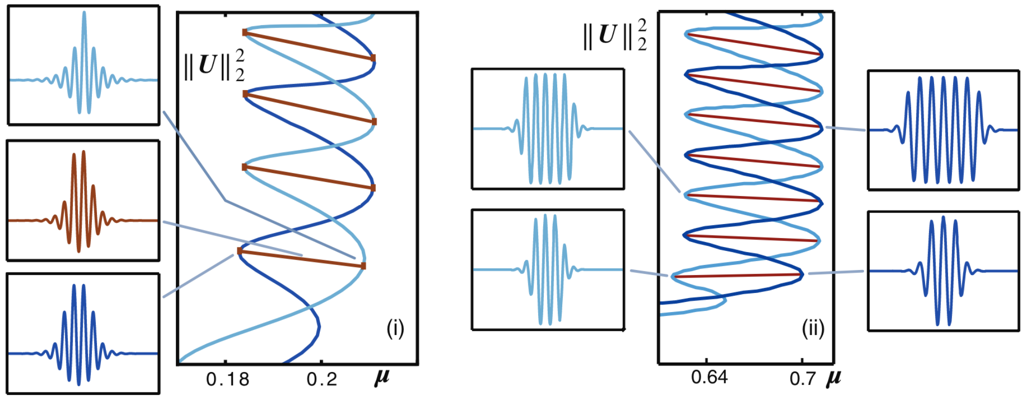

Figure 2.1: Bifurcation diagram of (i) the quadratic-cubic Swift-Hohenberg equation, and (ii) the cubic-quintic Swift-Hohenberg equation. Image from Beck et al. (2009). The snaking diagrams consists of two snaking branches of symmetric solutions connected by rung branches of asymmetric solutions. As you move up the snaking diagram, the width of the snaking region increases.

increases. The L^2-norm used in the bifurcation diagram acts as an indirect measure for the width of the nonzero regime of the profile.

There are additional branches of asymmetric solutions which look like rungs of a ladder, connecting the two symmetric branches near the saddle-nodes. These solutions do not satisfy the even symmetry condition, instead interpolating between the two symmetric states as you move across the branch from one symmetric branch to the other. The value at $x = 0$ moves from a local minimum at the first symmetric branch to a local maximum at the opposite symmetric branch. Given the combination of these two features, the winding snakes and connecting rungs, this is called a snakes-and-ladders bifurcation.

To understand the features of this bifurcation, it is useful to note some properties of (1.5.1). Since we are interested in stationary solutions we will set $U_t = 0$ so that we are concerned with the dynamical properties of a four-dimensional first order

ODE

$$U_1' = U_2, \tag{2.1.2}$$

$$U_2' = U_3, \tag{2.1.3}$$

$$U_3' = U_4, \tag{2.1.4}$$

$$U_4' = -2U_3 - (1+\mu)U_1 + \nu U_1^2 - U_1^3, \tag{2.1.5}$$

where $' = \partial_x$. The advantage of working with this system, is that we can interpret the desired PDE solutions as trajectories in the phase space $\mathbb{R}^4$. In particular, our desired localised patterns are homoclinic connections to the rest state zero. This correspondence between PDE solutions and functions in the spatial phase space is the key feature we exploit throughout this thesis.

The Swift-Hohenberg equation has a number of very nice properties. First note the PDE (2.1.1) has a $\mathbb{Z}_2$-symmetry as it is invariant under the change of variables $x \mapsto -x$. As a result the dynamical system (2.1.2)-(2.1.5) is $\mathcal{R}$-reversible for the map $\mathcal{R} : \mathbb{R}^4 \to \mathbb{R}^4$ defined by $(U_1, U_2, U_3, U_4) \mapsto (U_1, -U_2, U_3, -U_4)$.

Reversibility is a symmetry property of the phase space of certain ODEs. An ODE $\dot{u} = f(u)$ is $\mathcal{R}$-*reversible* if $\mathcal{R}$ is a linear[1] involution on the phase space X of the dynamical system, and $f \circ \mathcal{R} = -\mathcal{R} \circ f$ (where $\circ$ refers to the composition of functions). This symmetry means that movement forward in time is topologically equivalent to movement backward in time with equivalency given by the diffeomorphism $\mathcal{R}$. Or, put another way, by acting on trajectories in phase space by $\mathcal{R}$ we get a new trajectory of the dynamics at the expense of reversing time.

[1] In fact, $\mathcal{R}$ need not be linear, but to avoid a more complicated definition we assume linearity here as it is all we will need. For more information see Devaney (1977).

In reversible systems there is a natural notion for symmetric orbits. An orbit in the phase space of (2.1.2)-(2.1.5) is symmetric as it maps to itself under the action of the reverser $\mathcal{R}$. Due to the equivalence of the $\mathbb{Z}_2$-symmetry of the PDE (2.1.1) and the reversibility of the dynamical system (2.1.2)-(2.1.5), finding an $\mathcal{R}$-reversible (or symmetric) orbit of the dynamical system gives us a PDE profile with a predetermined symmetry. In this case, as the PDE is invariant under a change of variables $x \mapsto -x$, such solutions are even symmetric at the origin.

The Swift-Hohenberg equation is also conservative with an analytic conserved energy. As a result the dynamical system is Hamiltonian with a Hamiltonian function given by

$$\mathcal{H}(U_1, U_2, U_3, U_4) = U_2U_4 - \frac{1}{2}U_3^2 + U_2^2 + \frac{1+\mu}{2}U_1^2 - \frac{\nu}{3}U_1^3 + \frac{1}{4}U_1^4. \tag{2.1.6}$$

Conservativity is not required for snaking, but the presence of a Hamiltonian phase-space does impose additional structure on the snaking phenomenon. We point this out for the Swift-Hohenberg system as in contrast the Brusselator is not conservative, which has implications on the qualitative properties of the snaking bifurcation.

The burning mathematical question is then, how can we explain the existence and robustness of this bifurcation process? This is not a feature exclusive to the quadratic-cubic Swift-Hohenberg equation. Changing the nonlinearity to form the cubic-quintic Swift-Hohenberg equation,

$$U_t = -(1+\partial_x^2)^2U - \mu U + \nu U^3 - U^5, \tag{2.1.7}$$

again presents us with a snaking bifurcation, see Figure 2.1(ii). In this case, the system is again reversible but with a different $\mathbb{Z}_2$-symmetry: namely the operation

$x \mapsto -x$ and $U \mapsto -U$. This allows for symmetric profiles to be either odd or even at the origin, and indeed the snaking bifurcation diagram of this system contains symmetric branches of both even and odd profiles. While this equation is again conservative, we will see that this is not a necessary condition. The two key ingredients are: 1) reversibility, which provides a notion of symmetry and the possibility of symmetric breaking to form the asymmetric branches; and 2) the existence of heteroclinic connections between the underlying rest state and an $\mathcal{R}$-reversible periodic orbit in phase space.

Indeed the existence of localised pulses follows directly from the existence of a heteroclinic loop in phase space. Suppose that a front solution, as depicted in Figure 2.2, exists between the rest state zero and a $\mathcal{R}$-reversible periodic orbit. Here a $\mathcal{R}$-reversible periodic orbit is a periodic orbit which maps to itself under the action of the reverser $\mathcal{R}$. We will call such a connecting orbit a *front*. By acting on this orbit with $\mathcal{R}$ we get a new connecting orbit joining the periodic orbit to the rest state, which we call a *back*. This heteroclinic loop consists of orbits in the intersections of the stable and unstable manifolds of the rest state and periodic orbit. As such, we know that both the unstable and stable manifold of the rest state enter a small neighbourhood of the periodic orbit. This allows for the opportunity of finding homoclinic connections to the rest state that stay close to the periodic orbit for some large amount of time. These are exactly the localised solutions we are looking for as such orbits will shadow the periodic orbit, producing oscillations in space that correspond to the patterned region of the PDE profile.

The phenomenon of homoclinic snaking was first identified in an unfolding of a codimension-2 Hamiltonian-Hopf (or degenerate reversible 1-1 resonance) bifurcation, where the presence of reversibility and conservation allow for a quartet of complex eigenvalues to coalesce at zero (Dias and Iooss, 1996, Woods and Champ-

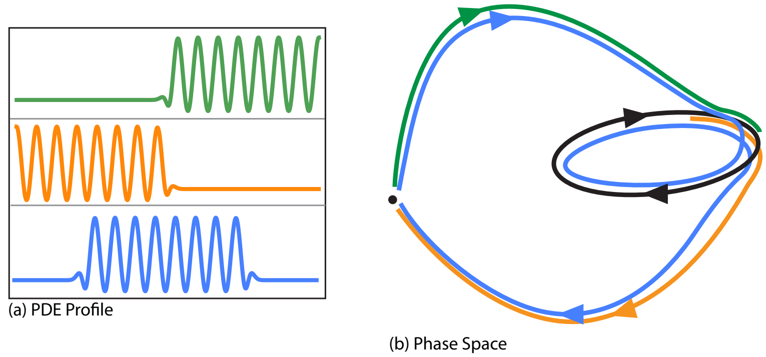

Figure 2.2: (a) Figures of a front, back and localised pulse in the Swift-Hohenberg Equation. (b) The corresponding heteroclinic and homoclinic connections in the 4-dimensional phase space of the stationary dynamical system.

neys, 1999). Such bifurcations are of interest in many physical applications due to the presence of conservative and reversible structure and the presence of homoclinic and heteroclinic connections (Champneys, 1998). However, at the time the full complexity of these bifurcations was not understood. Indeed, for certain normal forms relating to these bifurcations, Iooss and Peroueme (1993) showed the existence of pairs of reversible homoclinic orbits. It was only numerically, that Woods and Champneys (1999) were able to demonstrate snaking of symmetric homoclinic orbits. However, they did correctly identify the base mechanism, heteroclinic cycles, which is central to understanding the process of snaking.

The full structure of these bifurcation diagrams were not determined until the work of Burke and Knobloch (2006, 2007a,b) which discussed the existence and stability of localised solutions in the generalized Swift-Hohenberg equations. Critically, they identified the presence of asymmetric solutions bifurcating at pitch-fork bifurcations from the symmetric branches. They also identified the likely presence of heteroclinic front solutions in the snaking region of parameter space. These ideas were formalised into a predictive theory of snaking by Beck et al. (2009). Under certain global assumptions on the existence of heteroclinic fronts, the resulting snaking diagrams could be described qualitatively and quantitatively up to exponentially small errors. This included the symmetric and asymmetric branches and the locations of the saddle-node bifurcations of symmetric patterns and the symmetry breaking pitchfork bifurcations of asymmetric patterns. It is this framework that we will describe here and aim to extend to defect solutions in Chapter 3.

It should be noted that this theory must make use of global assumptions. The existence of heteroclinic fronts in general is difficult to prove, requiring advanced techniques from validated numerics or other highly nuanced arguments. Analytic results only exist under very specific conditions, such as in the vicinity of codimension-2 bifurcations. Chapman and Kozyreff (2009) used a multiscale analysis to demonstrate snaking without apriori global assumptions, near a degenerate Hamiltonian-Hopf bifurcation. They show the existence of a pair of a heteroclinic front and back in a small region of parameter space, which can be glued together to form pulses. However, their method only guarantees the existence of such fronts in an exponentially thin parameter range. The difficulty is also compounded by the fact that at each polynomial order the slowly modulating envelope of the pulse, and the high frequency oscillations of the patterned region are decoupled. As a result, to any finite order they find a family of solutions that is one dimension too large. These families are not true solutions however, as beyond-all-order analysis shows there is an exponentially small coupling between these scales that causes pinning of the high-frequency oscillations, removing all but a discrete number of pulses corresponding to the symmetric and asymmetric branches we have discussed. There is a significant difficulty in extending these results, so Beck et al. (2009) instead produce a predictive theory that assumes the presence of the global structure, leading to qualitative and quantitative predictions of the snaking curve. In such a way, this method does not constitute a proof of the snaking process, but a framework through which it can be understood.

There are also many other aspects of snaking that we will not discuss here. Snaking bifurcations have been observed in other more complicated situations such as stationary planar pulses (Avitabile et al., 2010), radial solutions (McCalla and Sandstede, 2010) and planar hexagons (Lloyd et al., 2008). The influence of topological properties of the periodic orbit have also been proved to distinguish between true snaking and a very similar formation of towers of isola solutions (Aougab et al., 2019). Stability results have also been formulated by Makrides and Sandstede (2019) where they are able to use spectral properties of the front and back to deduce spectral properties of the localised solutions. Also, as pointed out by Woods and Champneys (1999), under assumptions about the transversality of these homoclinic orbits, the work of Härterich (1998) (for reversible systems) or Devaney (1976) (for conservative systems), would imply the presence of infinitely many N-pulse solutions nearby the known homoclinic orbits. The solutions we have discussed so far are called 1-pulse solutions as there is only a single isolated patch of patterned state. There are also more complex localised solutions to be found in the proximity of the snaking diagram in the form of N-pulse homoclinic connections. Such connections are formed by gluing multiple fronts and backs together to make solutions that return N times to a neighbourhood of the periodic orbit. Unlike their 1-pulse counterparts, these solutions are not found on true snaking diagrams. Instead they seem to form figure-eight isolas which shadow the main snaking branch (Burke and Knobloch, 2009, Knobloch and Wagenknecht, 2008).

In this chapter, we introduce the main ideas needed to understand the snaking of stationary localized patterns in finite-dimensional systems. Instead of giving a complete account of the theory, we instead focus on the heuristic argument and the simplest possible set-up. The finer details, including precise asymptotics for the location of bifurcations and refined qualitative descriptions, can be found in the original work by Beck et al. (2009). We will begin by introducing the general set up, emphasising those properties of the Swift-Hohenberg system which are necessary for snaking. We will use these to prove a partial result of snaking that will resemble our new results in Chapter 3. We then describe how the global results lead to a qualitative and quantitative description of the snaking diagram. Finally, we discuss a robust way to numerically compute heteroclinic fronts and pulses in the Swift-Hohenberg equations, which we will then adapt later in our investigation of defect solutions.

2.2 Set Up and Heuristics

We begin by describing the key features of Swift-Hohenberg that allow us to describe snaking bifurcations in the simplest setting. While we pose this discussion around the Swift-Hohenberg equation and understanding Figure 2.1, the theory itself translates to any system on $\mathbb{R}^4$ of the form,

$$\dot{u} = f(u, \mu), \quad u \in \mathbb{R}^4, \ \mu \in J \subset \mathbb{R} \tag{2.2.1}$$

where the solutions of interest are 1-pulse homoclinic orbits and the dynamics have a number of basic properties. As such, we will use the example of Swift-hohenberg to motivate these properties, by then collect them hypotheses about the dynamical system (2.2.1).

These properties can be divided into three groups: symmetry, structural and global. The local, structural assumptions allow us to describe the dynamics nearby the fixed point and periodic orbit. While the global assumptions will tell us how solutions move from a neighbourhood of the fixed point to a neighbourhood of the periodic orbit. We can then use this understanding for form trajectories that asymptote to the fixed point while transiting the periodic orbit for a large amount of time. The eventual bifurcation diagram will have structure based on the symmetry and global assumptions.

2.2.1 Symmetry Assumptions

First we note that Swift-Hohenberg is both reversible and conservative. These properties give the equations a large amount of structure which we can exploit in getting our results.

Hypothesis 2.2.1.
- Equation (2.2.1) is reversible. That is, there exists a mapping $\mathcal{R} : \mathbb{R}^4 \to \mathbb{R}^4$ such that $\mathcal{R}^2 = I$, $\mathrm{Fix}(\mathcal{R})$ is 2-dimensional and $f(\mathcal{R}u, \mu) = -\mathcal{R}f(u, \mu)$ for all $u \in \mathbb{R}^4$ and $\mu \in J$.
- Equation (2.2.1) is conservative. That is, there exists a function $\mathcal{H} : \mathbb{R}^4 \to \mathbb{R}$ such that $\langle \nabla_u H(u, \mu), f(u, \mu) \rangle = 0$ for all $u \in \mathbb{R}^4$ and $\mu \in J$.
- Furthermore, the energy H is invariant under $\mathcal{R}$. That is, $\mathcal{H}(\mathcal{R}u, \mu) = \mathcal{H}(u, \mu)$ for all $u \in \mathbb{R}^4$ and $\mu \in J$.

Using reversibility we say that a solution $u(x)$ is $\mathcal{R}$-symmetric if $u(0) \in \mathrm{Fix}(\mathcal{R})$ as then we have $u(x) = \mathcal{R}u(-x)$ for all $x \in \mathbb{R}$.

In order to consider the continuation of patterns in the bifurcation parameter μ we must ask that these phase-space properties hold for values of $\mu \in J$ that covers our region of parameter space. For us we will consider the interval J to be non-empty with a non-empty interior. Note for Swift-Hohenberg we have already seen this is true in Section 2.1.

2.2.2 Structural Assumptions

Now we look at the main building blocks in phase space we need to produce the localised patterns in Figure 1.7. These properties are summarised in Figure 2.3.

Hypothesis 2.2.2. There is a hyperbolic saddle equilibrium at the origin with exactly two positive and negative eigenvalues for each $\mu \in J$. Moreover, the spectrum is bounded uniformly away from the origin for $\mu \in J$.

We assume only the existence of a hyperbolic equilibrium for each value of $\mu \in J$. Without loss of generality we translate that equilibrium to zero and we normalise the energy function so that $H(0, \mu) = 0$ for all μ. By reversibility, the spectrum of the equilibrium is invariant under multiplication by -1, so a hyperbolic equilibrium must have two stable and unstable eigenvalues.

Next we note that the Swift-Hohenberg equation has a symmetric periodic orbit which will correspond to the oscillatory motion in our localised patterns.

Hypothesis 2.2.3. For each $\mu \in J$ there exists a periodic orbit $\gamma(x, \mu)$ so that:

- the family $\gamma(\cdot, \mu)$ is smooth in μ,
- each γ is a symmetric periodic orbit (i.e. $\gamma(0, \mu) \in \mathrm{Fix}(\mathcal{R})$),
- each γ is in the zero energy level set and is non-degenerate in that $\mathcal{H}_u(\gamma(x, \mu), \mu) \neq 0$, and

- each γ has exactly two positive Floquet multipliers given by $e^{\pm 2\pi\alpha(\mu)}$.

By rescaling time and using the smoothness of the family $\gamma(\cdot,\mu)$, without loss of generality we assume that each periodic orbit has minimal period 2π to simplify our notation. Symmetry of the periodic orbits also means that on each γ there is exactly two points for which $\gamma(x,\mu)$ lies in the fixed space $\mathrm{Fix}(\mathcal{R})$ and these must be precisely $x = 0, \pi$ for all $\mu \in J$ due to rescaling.

The existence of periodic orbits inside the zero energy level set for each μ is the generic behaviour for small μ. In conservative systems, periodic orbits are generically found in one-parameter families parameterised by the energy $\mathcal{H}$ (Devaney, 1977, Vanderbauwhede and Fiedler, 1992). This will be true for us here as we have made the non-degeneracy assumption $\mathcal{H}_u(\gamma(x,\mu),\mu) \neq 0$ (which if true for one value of x, must be true for all values of x). As you vary the parameter μ, this family of periodic orbits persist by the Implicit Function Theorem, including the particular periodic orbits in the zero energy level set (for sufficiently small changes in μ).

Finally, we again note that the Floquet spectrum described in this hypothesis is also generic. There is a non-trivial center-subspace due to the presence of conservativity (or equivalently the presence of the family of periodic orbits described above). The remaining two Floquet multipliers are again symmetric in that the corresponding principal Floquet exponents are symmetric after multiplication by -1 and so have the form $\pm 2\pi\alpha(\mu)$.

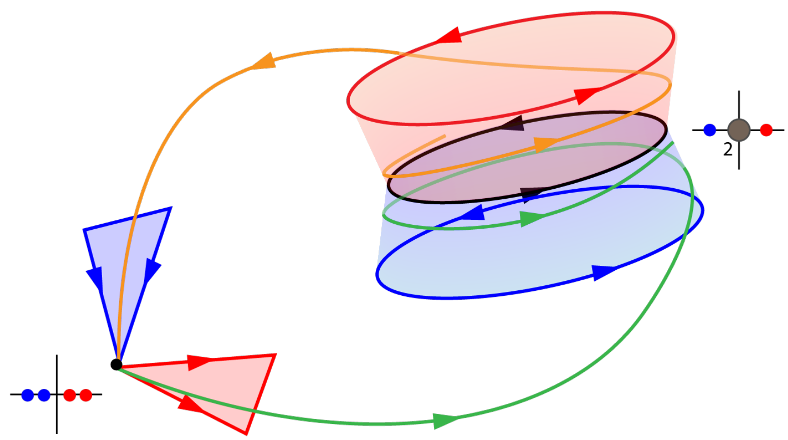

Figure 2.3: The key geometrical features of the Swift-Hohenberg equation for any $\mu \in J$. There is a hyperbolic equilibrium at zero, with two-dimensional stable and unstable manifolds. There is also a symmetric periodic orbit γ, with a two-dimensional center-manifold and three-dimensional center-stable and center-unstable manifolds. These two invariant sets are connected in a heteroclinic loop by the front and back solutions.

2.2.3 Global Assumptions

We now want to make assumptions on the existence of a heteroclinic connection from the origin to the periodic orbit. Before doing that, it is helpful to first consider why this is a reasonable assumption, and what implications this has on the geometry of phase space.

A heteroclinic back connection is an intersection between the stable manifold $W^s(0)$ of the rest state zero and the center-unstable manifold $W^{cu}(\gamma(\cdot, \mu))$ of the periodic orbit. By Hypotheses 2.2.2 and 2.2.3 we know the size of these manifolds, and hence, the size of a generic intersection of these manifolds. Indeed, the dimension of a generic transverse intersection of these manifolds is $2 + 3 - 4 = 1$, since they are two- and three-dimensional and the phase space is $\mathbb{R}^4$. Since we are looking for the intersection to form a 1-dimensional trajectory in phase space, this is good news.

Assuming we have a connection, that connection will generically be transverse.

However, calculation ignores the fact that this system is conservative by Hypothesis 2.2.1. This is possibly a problem as the presence of a conserved Hamiltonian $\mathcal{H}$ means that all dynamics are constrained to the 3-dimensional invariant level sets of $\mathcal{H}$. This does not change the dimension of the manifolds for the equilibrium. Since its stable and unstable manifolds are invariant and have the property that they converge to the equilibrium, they must be fully contained in the zero energy level set. This is not true for the periodic orbit. The center manifold of the periodic orbit is two-dimensional because it contains both the periodic orbit γ and the family of periodic orbits parameterised by the value of the energy $\mathcal{H}$. It is not enough to ask that we have a connection to the family of periodic orbits as would be the case if we include the full two-dimension center manifold. Instead, we must require we have to the specific periodic orbit γ on the zero energy level set. Thankfully, this is also taken care of for us by the invariance of this level set, which implies that our homoclinic connection must exist inside the level set of the rest state. Moreover, looking at the intersection of $W^s(0)$ and $W^{cu}(\gamma(\cdot,\mu))$ inside the energy level set we have a generic dimension $2+2-3=1$. So again, assuming that we have a homoclinic connection it should be generic.[2]

As described above, the presence of a heteroclinic connection from the periodic orbit to zero, and the symmetry of the periodic orbit, means we also have the reverse heteroclinic connection joining zero to the periodic orbit. The idea is to track the unstable manifold $W^u(0)$ from the origin into a small neighbourhood of the periodic orbit and match it to the stable manifold $W^s(0)$ of the origin, thereby forming a

[2]This perspective will become important later as genericity of the intersection in the larger ambient space generalises to cases where you do not have a conservation law pinning solutions to the smaller level set. Thus, our intuition from Swift-Hohenberg can be used in the non-conservative setting, assuming we can account for this additional degree of freedom. See Chapter 3 for more details.

homoclinic connection and our desired localised profile. To do so, we need to be able to track solutions through a small neighbourhood of the the periodic orbit.

Using Hypothesis 2.2.3, we can use normal hyperbolicity of the periodic orbit (inside the zero energy level set) to write the local dynamics in a normal form Fenichel (1979). Using the theory of Fenichel, there exists a smooth change of coordinates under which we can flatten the stable and unstable manifolds, and the resulting dynamics are linear to leading order.

Lemma 2.2.4 (Beck et al. (2009, Lemma 2.1))**.** *Assume Hypotheses 2.2.1-2.2.3 are met. There exist a $\delta > 0$ small enough, a smooth reversible change of coordinates nearby $\gamma(\cdot, \mu)$, and smooth real-valued functions h^c, h^s_j and h^u_j for $j = 1, 2$ such that* (2.2.1) *restricted to the zero energy level set has the form*

$$v^c_x = 1 + h^c(v, \mu)v^s v^u, \tag{2.2.2}$$

$$v^s_x = -(\alpha(\mu) + h^s_1(v, \mu)v^s + h^s_2(v, \mu)v^u)v^s, \tag{2.2.3}$$

$$v^u_x = +(\alpha(\mu) + h^u_1(v, \mu)v^s + h^u_2(v, \mu)v^u)v^u, \tag{2.2.4}$$

for $v = (v^c, v^s, v^u)$ in the annular neighbourhood $\mathcal{V} = S^1 \times [-\delta, \delta] \times [-\delta, \delta]$ and the reverser $\mathcal{R}$ acts on these coordinates by

$$\mathcal{R}(v^c, v^s, v^u) = (-v^c, v^u, v^s). \tag{2.2.5}$$

These coordinates are often called Fenichel or Shil'nikov variables. We can ask for reversibility of these coordinates by exploiting the reversibility of the original system. Since we are looking for local coordinates around the periodic orbit γ, we consider the variational equation,

$$v_x = f_u(\gamma(x;\mu),\mu)v, \tag{2.2.6}$$

which has Floquet spectrum described in Hypothesis 2.2.3. In particular, there exists two non-trivial solutions

$$v^s(x) = e^{-\alpha(\mu)x}p^s(x,\mu), \quad v^u(x) = e^{\alpha(\mu)x}p^u(x,\mu), \tag{2.2.7}$$

where p^s and p^u are 2π-periodic functions of x which are eigenfunctions of the Floquet spectral problem. Moreover, by applying the reverser $\mathcal{R}$ to v^s we see that we can choose $v^u(x) = \mathcal{R}v^s(-x)$. We then use these solutions in the construction of the new coordinate system, thereby building in the $\mathcal{R}$-reversibility of our Fenichel normal form, and giving us exactly the relationship described in (2.2.5).

The reason for reducing to these coordinates is that we can now more easily exploit the saddle structure of the periodic orbit. Denote $\Sigma_- = S^1 \times \{v^s = \delta\} \times [-\delta,\delta]$ and $\Sigma_+ = S^1 \times [-\delta,\delta] \times \{v^u = \delta\}$ the "faces" of the annular neighbourhood $\mathcal{V}$. These are transverse section of the dynamics and will necessarily capture the incoming stable and unstable manifolds, $W^s(0)$ and $W^u(0)$, of zero as they connect to the periodic orbit $\{(\varphi,0,0) : \varphi \in S^1\}$. The center-stable manifold $W^{cs}(\gamma(\cdot,\mu))$ of the periodic orbit is exactly $\{v = (v^c, v^s, 0)\}$, while the center-unstable manifold $W^{cu}(\gamma(\cdot,\mu))$ is $\{v = (v^c, 0, v^u)\}$ in these coordinates. Moreover, the center variable corresponds to the phase or the periodic orbit γ, meaning the strong stable and strong unstable fibers are the sets $W^{ss}(\gamma(\varphi,\mu),\mu) = \{v = (\varphi, v^s, 0)\}$ and $W^{uu}(\gamma(\varphi,\mu),\mu) = \{v = (\varphi, 0, v^u)\}$.

Assuming we start close to the incoming stable manifold, the saddle structure guarantees we will leave the neighbourhood close to the unstable manifold. More precisely we have the following Exchange Lemma.

Lemma 2.2.5 (Beck et al. (2009, Lemma 3.1))**.** *There exist positive constants L_0 and η so that for all $L > L_0$ and $\varphi \in S^1$ there is a unique solution $v(x) = v(x, \varphi)$ of* (2.2.1)*, defined on $x \in [-L, L]$ so that*

$$v(-L) \in \Sigma_-, \quad v(L) \in \Sigma_+, \; v^c(0) = \varphi, \quad v(x) \in \mathcal{V} \; \forall x \in [-L, L], \tag{2.2.8}$$

and the solution has asymptotics

$$v(-L) = \left(\varphi - L + \mathcal{O}(e^{-\eta L}), \; \delta, \; \delta e^{-2\alpha(\mu)L}(1 + \mathcal{O}(e^{-\eta L}))\right), \tag{2.2.9}$$

$$v(0) = \left(\varphi, \; \delta e^{-\alpha(\mu)L}(1 + \mathcal{O}(e^{-\eta L}), \; \delta e^{-\alpha(\mu)L}(1 + \mathcal{O}(e^{-\eta L}))\right), \tag{2.2.10}$$

$$v(L) = \left(\varphi + L + \mathcal{O}(e^{-\eta L}), \; \delta e^{-2\alpha(\mu)L}(1 + \mathcal{O}(e^{-\eta L}), \; \delta\right). \tag{2.2.11}$$

Moreover, the family of solutions is smooth in (φ, μ, L) and the error estimates can be differentiated. Finally the family is also invariant under the action of the reverser since,

$$v(x, -\varphi) = \mathcal{R}v(-x, \varphi) \tag{2.2.12}$$

for all $\varphi \in S^1$ and $|x| < L$.

The Exchange Lemma is a central result in geometric singular perturbation theory concerning normally hyperbolic manifolds, and was first proved by Jones, Kaper, and Kopell (1996). It has since been extended to much more general systems, such as the one we have here, see for instance Schecter (2008a,b), and is an incredibly useful result when constructing connecting orbits.

Note we have reversibility here due to the uniqueness of the solutions $v(x, \varphi)$ and the reversibility of the Fenichel normal form. Moreover, (2.2.12) gives us a precise characterisation of exchange solutions that are symmetric: that they have $\varphi = 0$ or π.

Using this result we can precisely track the movement of the unstable manifold $W^u(0)$ nearby the front solution through the annular neighbourhood $\mathcal{V}$. All that remains is to understand what the manifolds $W^u(0)$ and $W^s(0)$ look like upon entry and exit through $\Sigma_\pm$. Since we have reversibility in $\mathcal{V}$ given by equation (2.2.5), and the fact that the sections $\Sigma_\pm$ are mapped bijectively to each other by $\mathcal{R}$, it suffices to study just one of these intersections. We choose $W^s(0) \cap \Sigma_+$.

Define the two sets

$$G = \{v = (\varphi, v^s, \delta) \in \Sigma_+ : |v^s| < \varepsilon,\ v \in W^s(0, \mu)\}, \tag{2.2.13}$$

$$B = \{(\varphi, \mu) \in S^1 \times J :\ W^s(0, \mu) \cap W^{uu}(\gamma(\varphi, \mu), \mu) \neq \varnothing\}. \tag{2.2.14}$$

The set G is the intersection of the stable manifold $W^s(0)$ with the outgoing section Σ_+. For small enough ε, this set will be a graph over one of its variables. The set B encodes the existence of a heteroclinic back connection between the periodic orbit γ and the rest state zero. By assumption, this set must be non-empty for our framework of snaking. For the moment, we will make the simplest possible assumptions on these two sets. We will return to the implications and validity of these assumptions in Section 2.4.

Hypothesis 2.2.6. The set B is not empty. That is, there exists a heteroclinic back between $\gamma(\cdot, \mu^*)$ and zero which intersects Σ_+ at the point $v = (\varphi^*, 0, \delta)$ for $\mu = \mu^*$. Moreover, there exists a smooth function $g : S^1 \times J \to [-\delta, \delta]$ such that

- $p \in G$ if, and only if, $p = (\varphi, v^s = g(\varphi), \delta)$ for some $\varphi \in S^1$, and

- $g_{\varphi}(\varphi^*, \mu^*) \neq 0$.

Note that since G must contain the point $(\varphi, 0, \delta)$ corresponding to the known heteroclinic back, and since the heteroclinic back lies in the unstable manifold $W^{cu}(\gamma(\cdot, \mu^*))$ where $v^s = 0$, connecting backs correspond exactly to the roots of g: i.e. $g(\varphi^*, \mu^*) = 0$.

Using this assumption, we have an explicit parameterization of the stable manifold $W^s(0)$ in Σ_+ and can use this curve to match against exchange solutions inside $\mathcal{V}$.

2.3 Existence Argument for Symmetric Pulses

Our claim is that nearby the known back at $\mu = \mu^*$ we can find a countably infinite family of homoclinic solutions to the origin that spend a long time near the periodic orbit γ. We can also be precise about the amount of time they spend there, and the qualitative features of the resulting PDE profiles.

Theorem 2.3.1 (Existence of Symmetric Pulses)**.** *Assume Hypotheses 2.2.1-2.2.3 and 2.2.6 hold. Then there exists a constant integer $N_0 > 0$ large enough and constant $\eta > 0$ so that for every integer $n > N_0$ and $\varphi_0 = 0$ or π, there exists a symmetric homoclinic solution $u(x) = u(x; n, \varphi_0)$ with*

- *$u(x) \to 0$ as $|x| \to \infty$,*
- *$u(x) \notin \mathcal{V}$ for any $|x| > L$,*
- *$u(x) \in \mathcal{V}$ for all $|x| < L$, and*

- *$u(0)$ lies close to $\gamma(\varphi_0, \mu^*)$;*

where $L = \varphi^* - \varphi_0 + 2\pi n + \mathcal{O}(e^{-\eta n})$.

For a moment, consider only those points which are found for $\varphi_0 = 0$. Thinking of this result in terms of the snaking diagram, the existence of the heteroclinic front and back generates a discrete family of points in a tower, see Figure 2.4. Moreover, the vertical position of these points corresponds to $2L$, the total amount of time the solutions remain inside the neighbourhood $\mathcal{V}$. Since the solutions will be exponentially small as they converge in forward and backward time to zero, this time is a measurement of the width of the patterned region. Similarly, up to a constant multiple, this will also be a leading order estimate of the L^2 norm, as was plotted in Figure 2.1. The family is parameterised by $n \in \mathbb{Z}$ which successively adds a factor of 2π to the width L, which given that the periodic orbit has minimal period 2π, means that we add a stripe to the outside of the patterned region as we move up the tower. These will eventually become the countable family of branches making up the winding snakes of the diagram described earlier.

The second family of solutions, found for $\varphi_0 = \pi$ are similar but distinct from the first. Note that they have lengths L that sit in between the members of the first tower, offset by a phase difference of π. Moreover, we see that the phase of solutions at their midpoint is π, not 0. These two families represent the two possible ways to be $\mathcal{R}$-symmetric at the origin. For example, in the Swift-Hohenberg equation, one family would have minima at $x = 0$ and the other would have maxima at $x = 0$.

The idea of the proof is quite simple. We are looking to find an exchange solution $v(x)$ from Lemma 2.2.5 that satisfies the following matching conditions in Σ_- and

Σ_+ :

$$v(x) \in \mathcal{V} \quad \text{for} \quad |x| < L, \tag{2.3.1}$$

$$v(-L) \in W^u(0) \cap \Sigma_-, \tag{2.3.2}$$

$$v(L) \in W^s(0) \cap \Sigma_+, \tag{2.3.3}$$

and is $\mathcal{R}$-symmetric. By equation (2.2.12), we know an exchange solution is symmetric if, and only if, $v(0)$ has center coordinate $\varphi_0 \in \{0, \pi\}$. Moreover, in this case the reversibility then guarantees that $v(-L) \in W^u(0) \cap \Sigma_-$ if, and only if, $v(L) \in W^s(0) \cap \Sigma_+$. This reduces the matching conditions to

$$v(x) \in \mathcal{V} \quad \text{for} \quad |x| < L, \tag{2.3.4}$$

$$v(0) \in \mathrm{Fix}(\mathcal{R}), \tag{2.3.5}$$

$$v(L) \in W^s(0) \cap \Sigma_+. \tag{2.3.6}$$

We can solve these conditions using the asymptotics provided by the Exchange lemma and Hypothesis 2.2.6.

Proof. Let $\varphi_0 \in \{0, \pi\}$ and $L \in \mathbb{R}$ be large. Then using the Exchange lemma we can characterise exchange solutions v that spend time $2L$ in $\mathcal{V}$ and using Hypothesis 2.2.6 we can characterise points in the intersection $W^s(0) \cap \Sigma_+$. We want to find φ and L so that the exchange solution v lies in $W^s(0)$ by solving:

$$(\varphi_0 + L + \mathcal{O}(e^{-\eta L}), \mathcal{O}(e^{-\eta L}), \delta) = v(L) = (\varphi, g(\varphi), \delta). \tag{2.3.7}$$

This boils down to two equations:

$$\varphi_0 + L + \mathcal{O}(e^{-\eta L}) = \varphi \qquad \mod 2\pi, \tag{2.3.8}$$

$$g(\varphi) = \mathcal{O}(e^{-\eta L}). \tag{2.3.9}$$

Let $\varphi = \varphi^* + \bar{\varphi}$ so we can expand g about its known root φ^* corresponding to the heteroclinic back. This gives the system:

$$\varphi_0 + L + \mathcal{O}(e^{-\eta L}) = \varphi^* + \bar{\varphi} \qquad \mod 2\pi, \tag{2.3.10}$$

$$g_\varphi(\varphi^*)\bar{\varphi} + R(\bar{\varphi}) = \mathcal{O}(e^{-\eta L}) \tag{2.3.11}$$

where R is a smooth remainder term from Taylor's theorem and $R(x) = \mathcal{O}(x^2)$ as $x \to 0$. Hypothesis 2.2.6 assumes that the derivative is non-zero, so by the Implicit Function Theorem we can solve equation (2.3.11) for $\bar{\varphi}$ in the limit as $L \to \infty$. Then by (2.3.11), we find that the order estimate $\bar{\varphi} = \mathcal{O}(e^{-\eta L})$.

So we need to find a value of L for which equation (2.3.10) holds. Substituting our asymptotics for $\bar{\varphi}$ we have

$$\varphi_0 - \varphi^* + L = \mathcal{O}(e^{-\eta L}) \qquad \mod 2\pi, \tag{2.3.12}$$

so setting $L = 2\pi n + l$ for some $n \in \mathbb{Z}$ and $l \in S^1$ we find that

$$l = \varphi^* - \varphi_0 + \mathcal{O}(e^{-2\pi n \eta}) \tag{2.3.13}$$

where the equation is no longer modulo-2π and the higher order terms depend on l. By applying the Implicit Function Theorem in the limit as $n \to \infty$, we conclude that there exists an $l = l(n)$ that is given by (2.3.13) and the exponentially small terms are independent of l. As such,

$$L = 2\pi n + \varphi^* - \varphi_0 + \mathcal{O}(e^{-2\pi n\eta}) \tag{2.3.14}$$

completing the proof. □

We can significantly strengthen this result by using properties discussed in the previous section, thereby completing the diagram found in Figure 2.4. Recall we argued that generically the front and back constitute transverse intersections of the relevant stable and unstable invariant manifolds. Thus, without loss of generality, we should expect that we can replace Hypothesis 2.2.6 with the following Hypothesis.

Hypothesis 2.3.2. The set B is a 1-dimensional manifold close to $\mu = \mu^*$ and can be parameterised as a graph over the phase coordinate φ. That is, there exists a smooth function $z : S^1 \to J$ so that if (φ, μ) is close enough to (φ^*, μ^*), $(\varphi, \mu) \in B$ if, and only if, $\mu = z(\varphi)$.

Moreover, there exists a smooth function $g : S^1 \times J \to [-\delta, \delta]$ such that

- $p \in G$ if, and only if, $p = (\varphi, v^s{=}g(\varphi, \mu), \delta)$ for some $\varphi \in S^1$, and
- $g_\varphi(\varphi, z(\varphi)), g_\mu(\varphi, z(\varphi)) \neq 0$.

In this case, the single points we found in Theorem 2.3.1 can be extended branches of symmetric branches as depicted in Figure 2.4, and we have the existence of countably many branches of symmetric solutions. By assuming that g_μ is not zero at the front, we can use another application of the Implicit Function Theorem to show that, for each point φ^* in the proof of Theorem 2.3.1, we can find a family of nearby solutions parameterised by μ. Moreover, by uniqueness of solutions from the Implicit

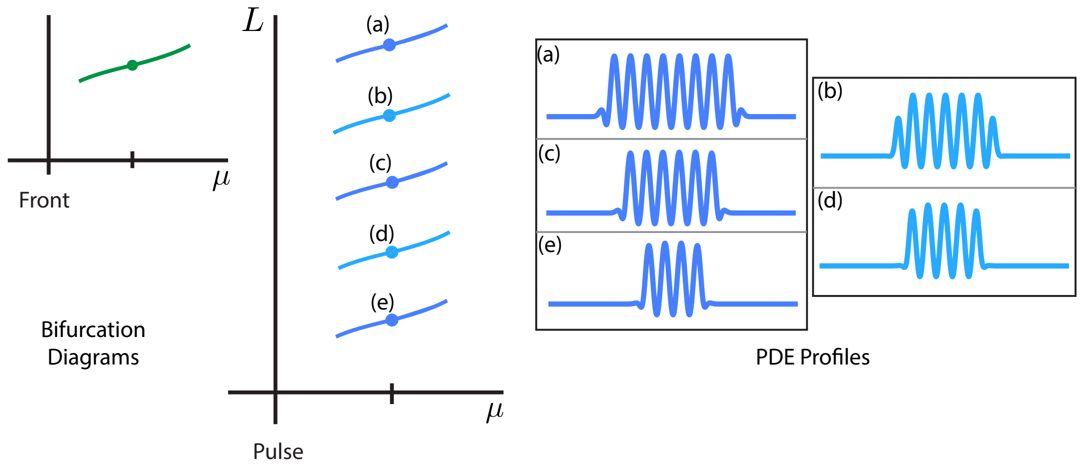

Figure 2.4: Step 1 of constructing the snaking diagram from the skeleton function z. Existence of a front/back generates a countably infinite family of homoclinic orbits sitting in a tower. The L^2-norm will be an indirect measure the time $2L$ spent in the neighbourhood $\mathcal{V}$. Persistence of the fronts/backs is reflected in the persistence of the countable families.

Function Theorem, these solutions must agree with those found in Theorem 2.3.1 for each individual value of φ^*. This completes the bifurcation diagram in Figure 2.4. However, note that this still does not give the full snaking picture we described earlier.

There is one final remark to make about this proof. In its current form we must assume that g_φ is not zero to apply the Implicit Function Theorem. This is important because if this derivative is zero, it flags a quadratic tangency between the manifolds $W^s(0)$ and $W^{cu}(\gamma(\cdot, \mu))$, see Figure 2.5. Such a tangency is a feature of a saddle-node bifurcation of the underlying front, at which point there are two fronts coalescing and disappearing. In fact, we need such points to be able to recover the full snaking diagram in Figure 2.1, as they will become saddle-nodes for the pulse solutions allowing for the characteristic snaking curves to emerge. Beck et al. (2009) use a slightly different approach to avoid this issue that only requires that g_μ be

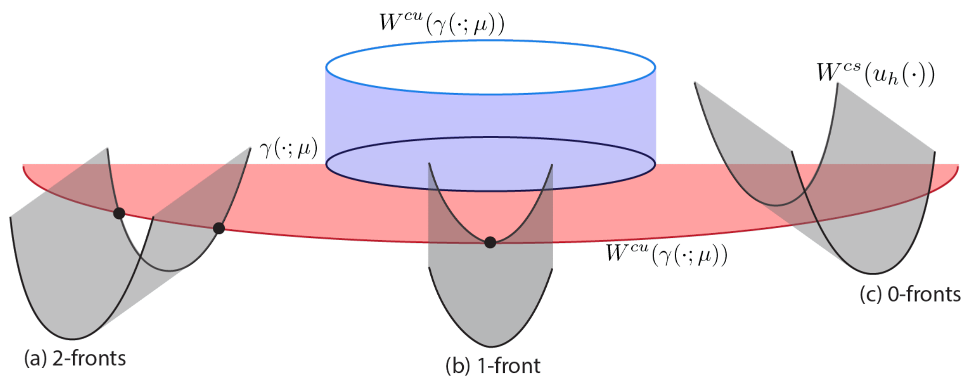

Figure 2.5: Unfolding of a quadratic tangency as μ is varied in our coordinates $\mathcal{V}$. It is by understanding this behaviour that we are able to build the full snaking diagram.

non-zero. In doing so they obtain leading order estimates for the location of the saddle-node bifurcations which are accurate to exponentially small errors.

2.4 Snaking and Notes on Global Assumptions

What we have seen so far is that the existence of fronts determines the existence of countably many branches corresponding to pulses of increasing length. To make the final jump to the full snaking diagram, we need to make assumptions on the structure of the front bifurcation diagram B, or equivalently on the skeleton function z.

We expect to find periodic behavior in the snaking diagram, so we assume periodic structure for the front bifurcation diagram. In particular, we ask that the front lie on an isola. So we replace Hypothesis 2.3.2 with the following.

Hypothesis 2.4.1. The set B is not empty and can be written as a graph of a smooth function $z : S^1 \to J$. The skeleton function z has the following non-degeneracy conditions:

- $z'(\varphi) = 0$ implies $z''(\varphi) \neq 0$, and
- $z(\varphi_1) = z(\varphi_2)$ and $z'(\varphi_1) = z'(\varphi_2) = 0$ implies that $\varphi_1 = \varphi_2 \mod 2\pi$.

Moreover, nearby this front we have that G is the graph of a smooth function $g : S^1 \times J \to [-\delta, \delta]$, and $g_\varphi(\varphi, z(\varphi))$ and $g_\mu(\varphi, z(\varphi))$ are uniformly bounded away from 0.

In words, the non-degeneracy conditions for z enforce that local minima and maxima are simple and do not share their values with other minima and maxima. This is needed to rule out higher codimension phenomena such as resonances. We also need to distinguish between the global extrema as the local extreme may not persist through to the final bifurcation diagram. The prototype skeleton function for the Swift-Hohenberg equation is found in Figure 2.6.

Once again, we note that the backs are represented by zeros of the function g as the backs lie in the unstable manifold of the periodic orbit given by $\{v^s = 0\}$.

As a consequence of this assumption, this periodicity of the front curve is inherited by the snaking diagram. The countable family of symmetric branches found in Figure 2.4 join together to form two snakes that wind backward and forward. We now have the structure seen in Figure 2.6. Note that the curves join up so that all solutions on one branch have the same even symmetry at the origin.

But more importantly, now any value of μ away from the global extrema of z, there are more than one front/back pair in phase space. This means there is a secondary means to produce homoclinic orbits - by following a front and back from

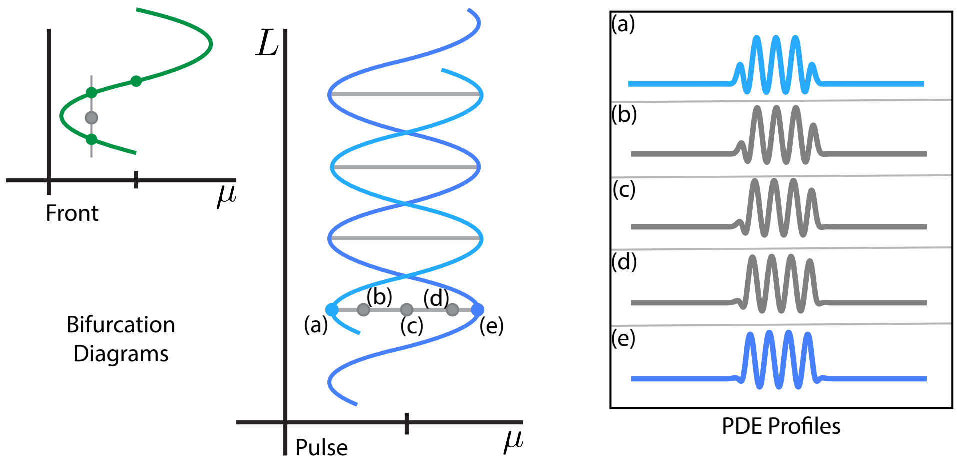

Figure 2.6: Final construction of the snaking diagram from the skeleton function z. Assuming periodicity of the front bifurcation diagram, the countable many families found in Figure 2.4 join up in a snake. They are also cross-connected by asymmetric rung branches which are formed by gluing fronts and backs which are not reversible pairs.

different $\mathcal{R}$-reversible pairs. The result is a homoclinic orbit that is not even at the origin and sits in between the symmetric homoclinics in the bifurcation diagram. This produces the asymmetric rungs. This gives us the complete snaking diagram depicted in Figure 2.6.

Theorem 2.4.2. *Assume Hypotheses 2.2.1-2.2.3 and 2.4.1 hold. Then there exists a constant integer $N_0 > 0$ large enough and constant $\eta > 0$ so that for every integer $n > N_0$ and $\varphi_1, \varphi_2 \in S^1$ for which $z(\varphi_1) = z(\varphi_2)$, there exists a homoclinic solution $u(x) = u(x; n, \varphi_1, \varphi_2)$ with*

- $u(x) \to 0$ *as* $|x| \to \infty$,
- $u(x) \notin \mathcal{V}$ *for any* $|x| > L$,
- $u(x) \in \mathcal{V}$ *for all* $|x| < L$, *and*

- *$u(0)$ lies close to $\gamma(\varphi, z(\varphi_1))$*

where $2\varphi = \varphi_1 - \varphi_2 \mod 2\pi$ and $L = (\varphi_1 + \varphi_2)/2 + 2\pi n + \mathcal{O}(e^{-\eta m})$.

As for the proof for the existence of symmetric orbits, we are interested in finding an exchange solution $v(x)$ satisfying the matching conditions

$$v(x) \in \mathcal{V} \quad \text{for} \quad |x| < L, \tag{2.4.1}$$

$$v(-L) \in W^u(0) \cap \Sigma_-, \tag{2.4.2}$$

$$v(L) \in W^s(0) \cap \Sigma_+. \tag{2.4.3}$$

So far we have not directly assumed anything about the shape of $W^u(0)$ in Σ_-. Thankfully, the reverser helps us again with this. From our characterisation, we know that a point p (close to the back solution) is in $W^s(0) \cap \Sigma_+$ if, and only if,

$$p = (\varphi, g(\varphi, \mu), \delta) \tag{2.4.4}$$

for some $\varphi \in S^1$. However, acting on p by the reverser $\mathcal{R}$ we must obtain a new point $\mathcal{R}p$ which lies in the opposite intersection $W^u(0) \cap \Sigma_-$ since when we restrict $\mathcal{R}$ to be functions $\Sigma_+ \to \Sigma_-$ and $W^s(0) \to W^u(0)$, it is bijective. Recall from equation (2.2.5) that

$$\mathcal{R}(v^c, v^s, v^u) = (-v^c, v^u, v^s).$$

As a result, we can use the function g to parameterise the unstable manifold as well. That is, $q \in \Sigma_- \cap W^u(0)$ nearby the front if, and only if,

$$q = \mathcal{R}(\varphi, g(\varphi, \mu), \delta) = (-\varphi, \delta, g(\varphi, \mu)) \tag{2.4.5}$$

for some $\varphi \in S^1$. From here we can use a similar strategy for the symmetric pulse case.

Proof. Using the Exchange Lemma asymptotics and our parameterizations for the unstable and stable manifolds in $\Sigma_{\pm}$, the matching equations (2.4.1)-(2.4.3) become

$$(\varphi - L + \mathcal{O}(e^{-\eta L}),\ \delta,\ \mathcal{O}(e^{-\eta L})) = v(-L)\ = (-\varphi_2,\ \delta,\ g(\varphi_2, \mu)), \tag{2.4.6}$$

$$(\varphi + L + \mathcal{O}(e^{-\eta L}),\ \mathcal{O}(e^{-\eta L}),\ \delta) = v(L)\ = (\varphi_1,\ g(\varphi_1, \mu),\ \delta), \tag{2.4.7}$$

for unknowns $\varphi, L, \varphi_1, \varphi_2$ and μ. We expect solutions in a 1-parameter family, and we will determine the solution as a function of φ_1. Suppose $\varphi_1^*, \varphi_2^* \in S^1$ so that $z(\varphi_1^*) = z(\varphi_2^*)$, as assumed in the theorem and let $\varphi_1 = \varphi_1^*$, $\varphi_2 = \varphi_2^* + \bar{\varphi}_2$ and $\mu = z(\varphi_1^*) + \bar{\mu} = z(\varphi_2^*) + \bar{\mu}$. Then equations (2.4.6) and (2.4.7) become the system of equations:

$$\varphi - L + \mathcal{O}(e^{-\eta L}) = -\varphi_2^* - \bar{\varphi}_2 \mod 2\pi, \tag{2.4.8}$$

$$\varphi + L + \mathcal{O}(e^{-\eta L}) = \varphi_1^* \mod 2\pi, \tag{2.4.9}$$

$$g(\varphi_1^*, z(\varphi_1^*) + \bar{\mu}) = \mathcal{O}(e^{-\eta L}), \tag{2.4.10}$$

$$g(\varphi_2^* + \bar{\varphi}_2, z(\varphi_2^*) + \bar{\mu}) = \mathcal{O}(e^{-\eta L}). \tag{2.4.11}$$

Again we can expand the function g around its known roots $(\varphi_j^*, z(\varphi_j^*))$ for $j = 1, 2$ in which case the final two equations become

$$g_\mu(\varphi_1^*, z(\varphi_1^*)\bar{\mu}) + R_1(\bar{\mu}) = \mathcal{O}(e^{-\eta L}), \tag{2.4.12}$$

$$g_\varphi(\varphi_2^*, z(\varphi_2^*))\bar{\varphi}_2 + g_\mu(\varphi_2^*, z(\varphi_2^*))\bar{\mu} + R_2(\bar{\varphi}_2, \bar{\mu}) = \mathcal{O}(e^{-\eta L}), \tag{2.4.13}$$

where R_1 and R_2 are again quadratic error terms from the Taylor expansion. By Hypothesis 2.4.1, the linear operator on the left-hand side is invertible and we can use the Implicit Function Theorem in the limit as $L \to \infty$ to solve for $\bar{\varphi}_2$ and $\bar{\mu}$ as functions of L, φ, φ_1^* and φ_2^*. Moreover, we find that $\bar{\varphi}_2$ and $\bar{\mu}$ are $\mathcal{O}(e^{-\eta L})$.

Substituting these solutions into the first two matching equations we find:

$$\varphi - L = -\varphi_2^* + \mathcal{O}(e^{-\eta L}) \mod 2\pi, \tag{2.4.14}$$

$$\varphi + L = \varphi_1^* + \mathcal{O}(e^{-\eta L}) \mod 2\pi. \tag{2.4.15}$$

an identical argument from the symmetric proof via the Implicit function theorem in the limit as L goes to infinity now works here. Let $L = l + 2\pi n$ and $\varphi = \Phi + 2\pi k$ for $l, \Phi in S^1$ and $n, k \in \mathbb{Z}$. Then in our new variables we are look for a solution (l, Φ) to the system:

$$\Phi - l = -\varphi_2^* + \mathcal{O}(e^{-2\pi\eta n}), \tag{2.4.16}$$

$$\Phi + l = \varphi_1^* + \mathcal{O}(e^{-2\pi\eta n}) \tag{2.4.17}$$

which we can solve in the limit as $n \to \infty$ by the Implicit Function Theorem. In terms of the original variables we have asymptotics

$$L = \frac{\varphi_1^* + \varphi_2^*}{2} + \pi n + \mathcal{O}(e^{-2\pi\eta n}), \tag{2.4.18}$$

$$\varphi = \frac{\varphi_1^* - \varphi_2^*}{2} + k\pi + \mathcal{O}(e^{-2\pi\eta n}), \tag{2.4.19}$$

completing the proof. □

In the proof we never use that φ_1^* and φ_2^* are different points. In fact, putting $\varphi_1^* = \varphi_2^*$ we find that $\varphi \in \{0, \pi\}$ and $L = \varphi_1^* + \pi n$ to leading order which recovers our results from the symmetric proof exactly.

Also note that φ comes in families parameterised by an integer k which is decoupled from the integer n denoting the location of our point in the snaking tower. This is not an accident as it flags that asymmetric solutions come in pairs with the same length L. Recall that φ is the phase of the solution when it reaches its midpoint in $\mathcal{V}$. Moreover $\varphi + \pi \equiv -\varphi \mod 2\pi$, and so we see that these solution pairs will be reversible reflections of each other.

Finally we note that the position of the asymmetric branches can be found as the midpoint between the symmetric states on either side to leading order, with only exponentially small errors. This means that they should bifurcate very near the saddle-node points. Beck et al. (2009) shows that these bifurcations are pitchforks, explaining why we find a pair of bifurcating solutions and why this generically breaks the symmetry induced by $\mathcal{R}$. They also use a very elegant global argument to show the asymmetric branches continue across the snaking diagram to the opposite symmetric branch. This is reflected in the variable φ which will continuously move from 0 (when $\varphi_1^* = \varphi_2^*$) to π (when $\varphi_1^* = \varphi_2^* + \pi$). These might not be the only asymmetric branches, however, as if z has local minima or maxima which are not global maxima, there can also be cases in which isolas of asymmetric solutions form.

2.5 Numerical Case Study - Swift-Hohenberg

We look at numerical approaches to approximate heteroclinic fronts on finite domains. We take a dynamical systems perspective and are interested in a numerical bifurcation analysis of the solutions. Our aim is to compute the approximations as regular roots of an appropriate nonlinear function which we can then continue in bifurcation parameters.

From a dynamical systems perspective there are many known ways to compute these solutions as heteroclinic and homoclinic connections. In particular, there are numerical implementations of Lin's method (see Krauskopf and Rieß (2008) for example) which are very efficient when paired with the pseudo-arclength continuation package AUTO (Champneys et al., 1996). Such a method would implement an idea very similar to the theoretical proof we demonstrated in the previous sections. We avoid such a method here as it is not clear whether such a numerical scheme is practical in the case of contact defects. Instead, we look to implement a Core-Far Field decomposition scheme similar to those introduced by Lloyd and Scheel (2017), Morrissey and Scheel (2015). The problem of finding fronts in the Swift-Hohenberg equation is a perfect test bed for this scheme as we look to extend it to the case of contact defects in Chapter 3.

For the Swift-Hohenberg equation, the computation of the pulse solutions is significantly easier, as the solutions converge to the rest state zero as $|x| \to \infty$. We concentrate on the method for determining the fronts, and in particular, determining the spatial wavenumber of the periodic core.

2.5.1 Core-Far Field Decomposition for Fronts

We are looking to find a solution to the stationary Swift-Hohenberg equation,

$$-(1+\partial_x)^2 U - \mu U + \nu^2 U - U^3 = 0, \tag{2.5.1}$$

which is asymptotic to the rest state zero as $x \to -\infty$ and asymptotic to the periodic oscillation as $x \to \infty$. For simplicity, we can write (2.5.1) as

$$LU + N(U) = 0, \tag{2.5.2}$$

where L is the linear operator $-(1+\partial_x)^2 - \mu$ and N is the nonlinearity $\nu^2 U - U^3$.

Eventually we want to determine a method for finding approximations of this solution on a finite domain, but it is instructive to first consider how you might find such a solution defined on the real line. The idea provided by Morrissey and Scheel (2015), Lloyd and Scheel (2017) is to recast the problem with the following ansatz. Let $U = \chi_+ U_+ + W$, where χ_+ is a smooth cut-off function and U_+ is the periodic oscillation we want to form our background state at positive infinity. Suppose we choose χ_+ to have support contained in $\{x > d\}$ and which is one for all $x > d + 1$. Then by enforcing that W be exponentially localised, we ensure that the solution U is a front solution.

Rewriting equation (2.5.2) in terms of W we then have

$$\begin{aligned} 0 &= LW + L\chi_+ U_+ + N(W + \chi_+ U_+) && (2.5.3) \\ &= LW + [L\chi_+ U_+ + N(\chi_+ U_+ + W)] + [N(W + \chi_+ U_+) - N(\chi_+ U_+)]. && (2.5.4) \end{aligned}$$

Assuming we evaluate the residuals for a localised W we see that each of the three terms here are also localised. We expect that as long as we choose initial data which is sufficiently localised, the scheme will provide us with a localised result.

The only detail we have to be careful about is ensuring is that we choose the correct periodic orbit as our background state at positive infinity. In the case of the Swift-Hohenberg equation, we can do this without too much thought as we are able to verify that our periodic orbit has zero energy. In non-conservative settings, however, we need a way to select the correct periodic orbit out of the family. We can again look back at our dynamical systems intuition. Based on our ansatz, the function W is exactly the displacement between the rest state zero (for $x \ll -1$) or the periodic orbit (for $x \gg 1$). So we need to ask that W lies in the correct stable or unstable manifold.

For $x \ll -1$, this is easy as the equilibrium at zero is hyperbolic and we can require convergence through the unstable manifold by enforcing that W should have bounded L^2-norm on $(-\infty, 0]$. For $x \gg 1$ this is harder as we have to contend with the center-stable manifold of the periodic orbit, including its two center directions. In particular, we need to enforce that our solution W converges through the strong stable fibers of the manifold and thereby converges exponentially quickly. To do so, we introduce an auxiliary integral phase condition which will enforce exponential convergence to the periodic orbit γ of wavenumber k. The residuals in equation (2.5.3) will ensure that we chose the correct wavenumber k[3].

To construct the wavenumber phase condition we use a Melnikov integral computation. Consider the linearization of the Swift-Hohenberg equation about the periodic orbit $\gamma(\cdot;\mu,k)$ where we now also parameterise the family by their spatial wavenumber,

$$0 = -(1+\partial_x^2)^2 U - \mu U + N'(\gamma(x;\mu,k))U. \tag{2.5.5}$$

[3]In previous sections we assumed without loss of generality by rescaling x that all the zero energy level sets had spatial wavenumber 2π. We now relax this assumption and parameterise the family by their true wavenumbers. It is equally valid to parameterise by the Hamiltonian energy $\mathcal{H}$

We can rewrite the linearization as a system of first order system

$$\begin{pmatrix} U_1 \\ U_2 \\ U_3 \\ U_4 \end{pmatrix}' = \begin{pmatrix} 0 & 1 & 0 & 0 \\ 0 & 0 & 1 & 0 \\ 0 & 0 & 0 & 1 \\ A & 0 & 2 & 0 \end{pmatrix} \begin{pmatrix} U_1 \\ U_2 \\ U_3 \\ U_4 \end{pmatrix}, \tag{2.5.6}$$

where $A = -(1+\mu) + 2\nu\gamma - 3\gamma^2$. The corresponding adjoint variational equation is

$$\begin{pmatrix} U_1 \\ U_2 \\ U_3 \\ U_4 \end{pmatrix}' = - \begin{pmatrix} 0 & 0 & 0 & A \\ 1 & 0 & 0 & 0 \\ 0 & 1 & 0 & 2 \\ 0 & 0 & 1 & 0 \end{pmatrix} \begin{pmatrix} U_1 \\ U_2 \\ U_3 \\ U_4 \end{pmatrix}. \tag{2.5.7}$$

Since the periodic orbit has a geometrically simple Floquet exponent at zero, this equation will have a unique bounded solution $\psi^+ = \psi^+(x)$. Moreover, this solution will have the property that $\psi^+ \cdot E_0(x) = 0$, where $E_0(x)$ is the spatial Floquet eigenfunction of (2.5.6) with Floquet exponent zero. Our desired phase condition is then,

$$\int_M^\infty \psi^+(x) \cdot \mathbf{W}(x)\mathrm{d}x = 0, \tag{2.5.8}$$

where $\mathbf{W} = (W, \partial_x W, \partial_x^2 W, \partial_x^3 W)$. The dot product ensures that W does not move in a direction that modulates the wavenumber of the periodic oscillations, instead locking on to the one value of k. We integrate over an interval of values for x for numerical purposes, on the real line we only need to evaluate the integrand at a single point.

For conservative systems, this phase condition is equivalent to looking at the dot product between $\mathbf{W}$ and the gradient of the energy functional $\mathcal{H}$. Meaning the phase condition is zero only when the trajectory W lies inside an energy level set.

To formalize that this numerical scheme is well-posed one can show that our front solution is a regular zero of the nonlinear function defined in (2.5.3). A necessary condition for this is that the linearization of (2.5.2) about the front solution should be Fredholm with index zero. Spatial dynamical systems arguments show that this is not the case when the system is posed on $L^2(\mathbb{R})$ due to the presence of the center-manifold of the periodic orbit. By using Weyl sequences it is possible to show that the linearization is not closed, and hence not Fredholm.

This is partially rectifiable by the introduction of exponential weights. Let $L^2_\eta(\mathbb{R})$ be the space of square integrable functions with respect to the norm

$$||u||_\eta := \left(\int_{\mathbb{R}} e^{\eta|x|}|u(x)|^2 \mathrm{d}x\right)^{1/2}, \tag{2.5.9}$$

for some small positive $\eta \in \mathbb{R}$. This norm has the effect of penalising convergence that is not fast enough in the tails. As such, only functions u that have tails which converge faster than $e^{-\eta|x|}$ will have finite L^2_η-norm. By posing our linearization on this space, we exclude convergence through a center-manifold, which decays at only algebraic speeds. As a result the linearization is now Fredholm and its index is the difference between the Morse Indices of linearizations about the background states. A simple computation shows that this index is -1, but introduction of the phase condition and the parameter k then returns the Fredholm index to zero.

To summarize, in our numerical scheme we look for a solution (W, k) for the system

$$LW + L\chi_+ U_+ + N(W + \chi_+ U_+) = 0, \tag{2.5.10}$$

$$\int_M^\infty \psi^+(x) \cdot \mathbf{W}(x) \mathrm{d}x = 0, \tag{2.5.11}$$

which is sufficiently smooth and has finite L^2_η-norm (for small positive η). The function U_+ is the periodic orbit $\gamma(\cdot;\mu,k)$ and ψ^+ is its corresponding unique bounded solution to the adjoint variational equation (2.5.7).

2.5.2 Implementation on Bounded Domains

To actually implement this scheme in practice, we now need to consider how to adapt the scheme to look for solutions on bounded domains $[-L, L]$. In doing so, we must be careful to set up the problem in such a way that W remains localised, and to determine a method for finding U_+ and ψ^+ given a value of k.

On a finite domain we can no longer directly enforce localization with norms since all norms are equivalent. Instead, we replace the norm conditions by boundary conditions that will ensure convergence in the correct way. Again for $x = -L$, this is easy as the rest state zero is hyperbolic and convergence is exponentially fast. We need to be careful on the right boundary at $x = L$. Just as in the situation on the real line, we need to determine how localisation might fail. There are two ways: the solution converges to the incorrect periodic oscillation; or, the solution converges to the correct periodic oscillation but with a different phase offset than U_+.

We have already accounted for the first problem with our wavenumber phase condition. To account for the second problem we need impose Neumann boundary conditions on both U_+ and W. By applying Neumann boundary conditions to W we ensure that the interface cannot be translated in x against the background oscillations U_+. We also apply Neumann conditions to exclude asymptotics of the form $W \sim \partial_x U_+$ for large x, since $\partial_x U_+$ is the generator of spatial translations for the linearized dynamics near the periodic oscillations.

Finally, we need to determine a method for finding the functions U_+ and ψ_+ given a wavenumber k. The periodic oscillation is a solution to the equation

$$-(1 + k^2\partial_x^2)^2 U_+ - \mu U_+ + \nu U_+^2 - U_+^3 = 0, \tag{2.5.12}$$

$$\partial_x U_+(0) = \partial_x U_+(2\pi) = \partial_x^3 U_+(0) = \partial_x^3 U_+(2\pi) = 0, \tag{2.5.13}$$

where we apply Neumann conditions due to the argument above. The choice of Neumann conditions actually helps us here, since it removes the ability for the solutions to translate in x. Determining the bounded solution to the adjoint variational equation is slightly harder. Recall that this is a solution to an equation of the form

$$\partial_x \psi = -DF^T(U_+(x))\psi, \tag{2.5.14}$$

where $DF(U_+)$ is the matrix found in equation (2.5.7). However, ψ^+ is not any solution of this equation, but the unique bounded solution. This is possible by looking for periodic solutions that satisfy Neumann boundary conditions, as for our equation for U_+. Directly computing solutions to (2.5.14) can be difficult as numerical errors have a tendency to break boundedness of the solution. We can augment this equation by adding an inhomogeneous perturbation to obtain

$$\partial_x \psi = -DF^T(U_+(x))\psi + \varepsilon F(U_+(x)). \tag{2.5.15}$$

Solving for ψ and ε we get the same bounded periodic solution ψ^+ and $\varepsilon = 0$. However, the scheme is significantly more stable as when ε is nonzero, the inhomogeneity has the effect of breaking the bounded periodic orbit. Finally we note that the adjoint variational equation is linear and will have a family of solutions $\lambda\psi^+$ for $\lambda \in \mathbb{R}$. So we also need to add a phase condition that selects only a single scalar multiple λ. A condition using the squared L^2-norm of ψ, such as $||\psi^+||^2 - 1 = 0$ would achieve this.

To summarize the scheme on a bounded domain, we are looking for a solution (W, k) to the equations:

$$LW + L\chi_+ U_+ + N(W + \chi_+ U_+) = 0, \tag{2.5.16}$$

$$W(-L) = W(L) = \partial_x^2 W(-L) = \partial_x^2 W(L) = 0, \tag{2.5.17}$$

$$\int_M^\infty \psi^+(x) \cdot \mathbf{W}(x) \mathrm{d}x = 0; \tag{2.5.18}$$

subject to first finding a solution $(U_+, \psi^+, \varepsilon)$ to the auxiliary equations:

$$-(1 + k^2\partial_x^2)^2 U_+ - \mu U_+ + \nu U_+^2 - U_+^3 = 0, \tag{2.5.19}$$

$$\partial_x U_+(0) = \partial_x U_+(2\pi) = \partial_x^3 U_+(0) = \partial_x^3 U_+(2\pi) = 0, \tag{2.5.20}$$

$$\partial_x \psi^+ = -DF^T(U_+(x))\psi^+ + \varepsilon F(U_+(x)), \tag{2.5.21}$$

$$\partial_x \psi^+(-L) = \partial_x \psi^+(L) = 0, \tag{2.5.22}$$

$$\int_0^{2\pi} \psi(x)^2 \mathrm{d}x - 1 = 0. \tag{2.5.23}$$

2.5.3 Results

We implemented the scheme above in MATLAB using a combination of fsolve and an implementation of the Newton-GMRES algorithm modified from code created by Avitabile (2016).

The auxiliary equations (2.5.19)-(2.5.23) were computed on a domain $[0, 2\pi]$ consisting of a single wavelength a using spectral scheme via a discrete cosine transform. We do not use a Fourier decomposition, as that would enforce periodic boundary conditions. By using a discrete cosine transformation of type-1, we impose even symmetry on both endpoints of the domain which is equivalent to Neumann boundary conditions. The advantage of using Fourier type methods is that it is easy and very accurate to form the periodic extension of a single wavelength onto the full domain.

The full residuals (2.5.16)-(2.5.18) are computed on the full domain $[-L, L]$. We use a mixed scheme with Fourier spectral differentiation matrices in time and 4-th order finite differences with Neumann boundary conditions in space. The smooth cut off function $\chi+$ is chosen to be an appropriate hyperbolic tangent function which is close to 1 on the right quarter of the domain. This leads to a discrete system that is relatively sparse, and allows us to use Krylov subspace methods to run an inexact Newton iteration in conjunction with a basic secant continuation code.

Our results are shown in Figure 2.7. The bifurcation diagram for the fronts appears to snake as the bifurcation parameter is varied. This is not surprising, as we assume the the bifurcation diagram is periodic. Note that the diagram does not connect into an isola because we plot the diagram against the L^2-norm of the interface solution $w(x)$. As you vary μ and traverse a period of the bifurcation diagram, the front invades the domain, as seen in Figure 2.7(b)-(c). On the real line, the result of this would be that you obtain the same front translated to the left by one spatial oscillation. This is the basis of the periodic assumption in the our framework for snaking.

We can also compare the selected wavenumber k of the fronts to the known zero-energy periodic oscillations for each μ, Figure 2.7(d). We see that these agree very well. Also note that the interface solutions pictured in 2.7(b)-(c) are very well localised on right side of the domain. Taking these observations together we conclude that our phase condition works very well. This is promising as it indicates that we should be able to extend this method to find front contact defects in the future.

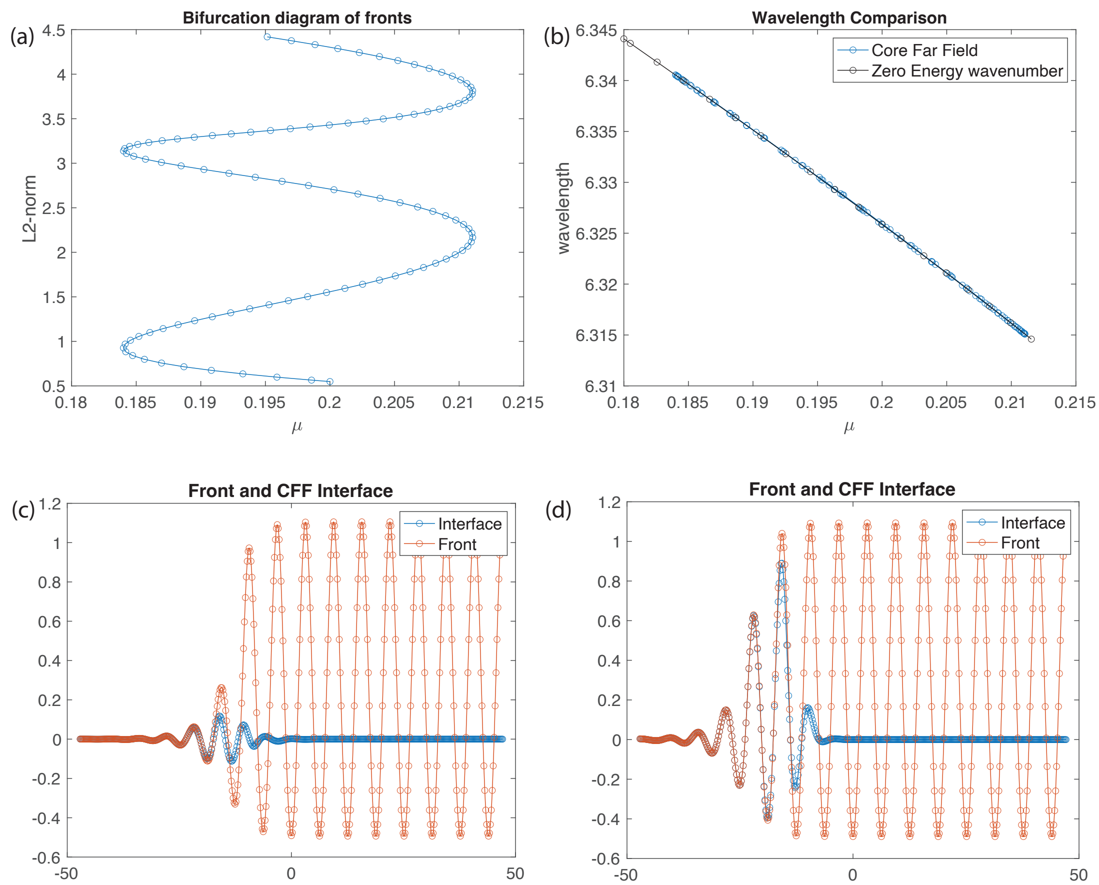

Figure 2.7: Numerical results using core-far field decomposition of fronts in Swift-Hohenberg. (a) Bifurcation diagram of the fronts. (b) A comparison of the selected wavelength $2\pi/k$ with the known wavelength of the zero energy periodic orbit for each μ.(c)-(d) Example fronts at the points marked in (a).

Chapter Three

Snaking of Contact Defects in the Brusselator

3.1 Introduction

Now we return to the snaking of pattern solution in reaction-diffusion systems. Recent numerical studies by Tzou et al. (2013) have collected numerical evidence for a new bifurcation processes for defects in reaction-diffusion equations, in particular the Brusselator. They numerically observed that symmetric contact defects exist in the neighbourhood of a codimension-2 Turing-Hopf bifurcation and that they appear to snake as the diffusion ratio is swept through a narrow region of parameter space. The contact defects themselves are a mixed state where the core region is a temporally homogeneous Turing pattern and the background oscillations are the spatially homogeneous Hopf mode. Their studies indicate that in a narrow region of parameter space there exists a tower of saddle-node bifurcations joining a countably infinite number of branches of contact defects. Moreover, as you traverse the tower the inner core region is allowed to grow.

A defect solution (Sandstede and Scheel, 2004) consists of a central core region mediating between two time-periodic background states, as seen in Figure 3.2. Such solutions have been observed experimentally (Perraud et al., 1993) and studied both numerically and analytically in many applications. In particular, they provide a 1-dimensional analogue of spiral and target waves for reaction-diffusion equations. For our purposes here, we will focus on *contact defects*, which are defects asymptotic to wave trains with specific group velocity properties. Our prototypical example of these patterns are defect solutions asymptotic to spatially homogeneous, temporal oscillations. For a complete discussion of defect solutions, see Sandstede and Scheel (2004).

As we have seen in Chapter 2, the theory of homoclinic snaking in the case of localized patterns can be understood through the lens of homoclinic and heteroclinic bifurcations. One assumes the presence of fronts: a solution that is asymptotic in backward time to the rest state zero and in forward time to a spatially periodic orbit. By reversibility this implies the existence of a commensurate back solution found by reversing the spatial coordinate. That is, asymptotic in backward time to the oscillating state and in forward time to zero. One then asks whether, if you were to cut these solutions at the right places, they could be glued together to form an exponentially localised solution with a spatially oscillating core region. In the conservative setting, for example the quadratic-cubic or cubic-quintic Swift-Hohenberg equation (Beck et al., 2009), the is answer is affirmative. Moreover, if you assume that the fronts exist and continue in a bifurcation parameter (and make a global assumption about the shape of the corresponding front bifurcation diagram - that it is an isola), then you can qualitatively and quantitatively predict the resulting bifurcation diagram. There are two branches of symmetric solutions each of which winds back and forth through the bifurcation interval at a countable succession of saddle nodes, see for example Figure 3.1. Moving up through each saddle node bifurcation the inner core region grows. These symmetric branches are connected at periodic intervals by branches of asymmetric solutions like rungs of a ladder. The shape of the snaking diagram can be predicted, up to exponentially small errors, using only the bifurcation diagram of the front solutions.

Here we present a rigorous framework for the existence and continuation of contact defects in general reaction-diffusion systems with reversible symmetry. Moreover, we show that these patterns undergo snaking bifurcations, and the snaking bifurcation diagrams found have oppositely winding symmetric branches connected by asymmetric branches. In contrast to the case of stationary localised pulses, the bifurcation diagrams have a number of new intriguing features, including tubular

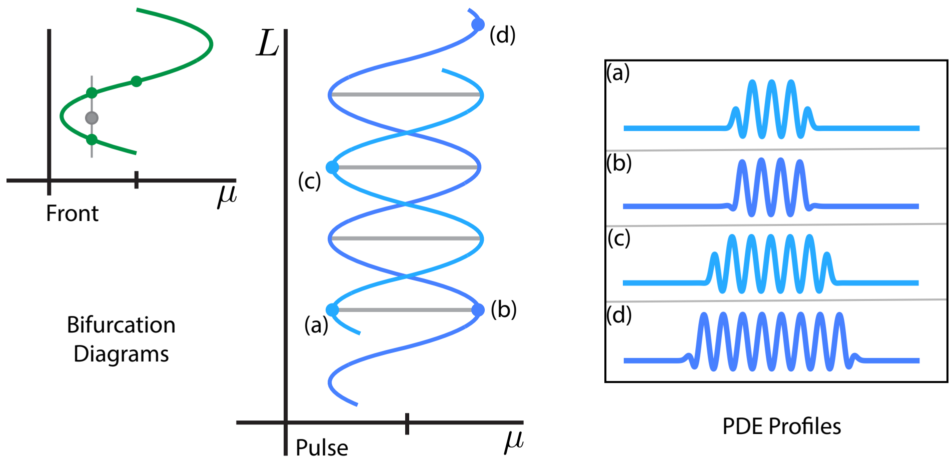

Figure 3.1: (a) The bifurcation diagram for the isola of fronts. (b) The bifurcation diagram of exponentially localised homoclinics. The shape of the snaking diagram can be predicted (up to exponentially small terms in the width of the striped region) by the periodic function for the isola.

families of asymmetric defects. These results constitute the first fully rigorous results on homoclinic snaking in infinite-dimensional systems, and demonstrate surprising features that depart from similar results in the classical setting.

Our main results, applied directly to the Brusselator, can be formulated in the following way.

Hypothesis 3.1.1. Suppose there exists a smooth function $(z, \kappa^*) : S^1 \to J \times K$ such that for every $\mu{=}z(\varphi)$ in J, there exists a front solution to the Brusselator for diffusion ratio $D = \mu$ which is asymptotic in forward time to the Turing pattern with wavenumber $\kappa^*(\varphi)$ and asymptotic in backward time to the spatially homogeneous oscillation. Furthermore, we assume that this bifurcation family of fronts satisfies genericity conditions corresponding to the transversality and general position of the stable and unstable manifolds of the Turing pattern and homogeneous oscillations respectively.

The formulation of the these genericity conditions is difficult, and a full account of these is given in Section 3.4. Assuming these conditions hold we prove the following two theorems.

Theorem 3.1.2 (Snaking of Symmetric Defects)**.** *Assume Hypothesis 3.1.1 holds. Then there exists* $N \in \mathbb{Z}$ *and* $\eta > 0$ *such that, for every integer* $n > N$*, and phases* $\alpha, \varphi_0 \in \{0, \pi\}$*, there exists a unique contact defect solution with core width* $L = (2\pi n + \varphi_0 - \varphi)/\kappa^*(\varphi) + \mathcal{O}(e^{-\eta n})$ *and phase offset* α *for the parameter value* $\mu = z(\varphi) + \mathcal{O}(e^{-\eta n})$*.*

Theorem 3.1.3 (Snaking of Asymmetric Defects)**.** *Assume Hypothesis 3.1.1 holds. Then there exists* $N \in \mathbb{Z}$ *and* $\eta > 0$ *such that, for every* $n > N$*, phase* $\alpha \in S^1$*, and pairs of phases* $(\varphi_1, \varphi_2) \in S^1 \times S^1$ *where* $z(\varphi_1) = z(\varphi_2)$*, there exists a unique contact defect with background phase offset* α *and core width*

$$L = \frac{2\pi n - (\varphi_1 + \varphi_2)}{\kappa^*(\varphi_1) + \kappa^*(\varphi_2)} + \mathcal{O}\left(\frac{\Delta\kappa}{n} + e^{-\eta n}\right) \tag{3.1.1}$$

where $\Delta\kappa = \kappa^*(\varphi_1) - \kappa^*(\varphi_2)$*. Moreover, these defects move at a wavespeed* $c = \mathcal{O}(\Delta\kappa/n + e^{-\eta n})$*, have temporal frequency* $\omega = \omega_0 + \mathcal{O}(c^2)$ *and connect background wavetrains with spatial wavelengths* $k = \mathcal{O}(c^2)$*.*

A full discussion of these results is given in the subsequent section. However, we note that there are a large amount more asymmetric solutions than are predicted in the theory of homoclinic snaking for stationary patterns. These solutions come in the form of defects with arbitrary background phase offsets, and add substantial complexity to the snaking bifurcation structure. As such these results constitute a significant step forward in our understanding of homoclinic snaking. We are also not aware of any previous results demonstrating the existence of defects with arbitrary phase offsets in the literature, making these novel results in the area of spatial dynamical systems as well.

It is tempting at first to believe that these new features, and additional complexity, is due only to the new infinite-dimensional setting. However, the fundamental difficulty is the introduction of an additional symmetry generated by translations in time. These symmetries are present in any finite-dimensional model of the snaking process, in particular the minimal 6-dimensional model discussed in Section 3.2.2, and are not themselves infinite-dimensional. These symmetries have a profound impact on the nature of our existence result. As demonstrated in Figure 3.2, we can shift any defect solution in time and we have a new solution. This means that however we construct our defect solutions we must be able to find each solution and all its time-translates. The geometry of the problem, and the resulting bifurcation equations, becomes significantly more complex with this addition.

By itself this is already nontrivial, but it leads to a more surprising observation. We can also act on a solution by a shear-shift. That is, by shifting only one half of the pattern cut directly down the center of the core region. Looking at the resulting spatiotemporal profile, the core region is essentially unchanged - it is still a temporally homogeneous Turing pattern of the correct wavelength. It is natural to ask if this is again a solution. The answer is no, but it will be very close to one which moves at a very small but *nonzero* wave speed. For contact defects, the shear shift by any angle will give you a profile close to a slowly moving defect with the same phase offset in background oscillations. Accounting for and dealing with this symmetry and near-symmetry is the key, novel result of this work.

The infinite-dimensional nature of the problem does present technical challenges of its own. For example, we need to understand the geometry of the infinite-dimensional phase space, and coherently account for the symmetries described above

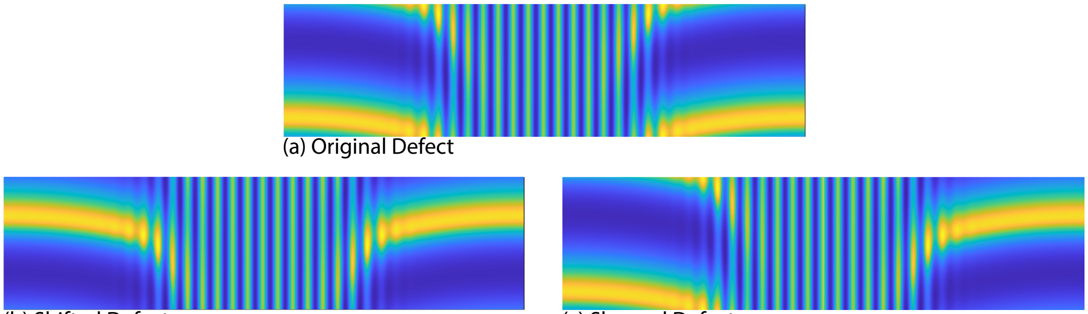

Figure 3.2: A diagram depicting the effects of translation. (a) A contact defect for the Brusselator. (b) The defect time translated by half a wavelength. (c) The defect shear translated by half a wavelength.

while formulating the right notions of transversality and general position for that geometry. This is non-trivial, and requires essential changes to the set-up and proof of the existence results here in comparison to previous work in homoclinic snaking. In accomplishing this, we present a framework that applied to general reaction diffusion equations that satisfy a set of minimal equations. Theorems 3.1.2 and 3.1.3 are then corollaries of these more general results.

In Section 3.2 we introduce the key intuition that underlies our results and analysis. We will recall the intuition obtained in the previous chapter for snaking for stationary, localised patterns, and contrast that to the new scenario. We will also state the main results of our work, which apply to general reaction diffusion equations satisfying certain minimal assumptions, and expand on the qualitative features of such bifurcations. Section 3.3 then gives a basic introduction to the tools of spatial dynamics that we use in building our intuition and justifying our assumptions. This includes a summary of the spatial spectral properties of wavetrains, homogeneous oscillations and Turing patterns. We also discuss the formal definition and properties of contact defects. Section 3.4 details the rigorous set up and Hypotheses we use to study snaking in reaction-diffusion systems. Sections 3.5 and 3.6 then prove Theorems 3.2.1 and 3.2.2 which constitute our new, novel results. Finally 3.7 details a new numerical scheme to compute and continue contact defects in the Brusselator, extending previous schemes by Morrissey and Scheel (2015) and Lloyd and Scheel (2017).

3.2 Intuition and Main Results

Here we lay out the intuition behind the snaking process in reaction diffusion systems and formally state our main results. Before discussing this intuition for contact defects, we summarise the intuition that leads to snaking of stationary localised pulses in Swift-Hohenberg described in Chapter 2. In doing so, we point out the similarity and essential differences in the set-up that produce our new, more complicated bifurcation diagrams.

3.2.1 Finite Dimensional Analogue and Intuition

Recall the term snaking bifurcation comes from studies of exponentially localised solutions in reversible ODEs. As a model for the snaking process consider the scalar quadratic-cubic Swift-Hohenberg equation

$$U_t = -(1 + \partial_x^2)^2 U - \mu U + \nu U^2 - U^3 \tag{3.2.1}$$

although the exact details of the equation are less important than its properties. We wish to look for exponentially localised solutions which are stationary in time and asymptotic to the rest state zero. After setting $U_t = 0$ the task becomes locating homoclinic connections to the origin in a four dimensional phase space with dynamics

$$u_x = f(u; \mu). \tag{3.2.2}$$

We can immediately verify the following facts for a non-empty open interval of values J for $\mu > 0$. Equation (3.2.2) is both conservative and reversible. Here reversible means that there exists a $\mathbb{Z}_2$-symmetry operation which, combined with a reversal of time, leaves the dynamics unchanged. The trivial rest state at zero is a saddle point with spectrum consisting of four real eigenvalues - two stable and two unstable. There also exists a reversible periodic orbit, $\gamma(x; \mu)$, which has two Floquet exponents at zero (corresponding to conservation) and two hyperbolic exponents one stable and one unstable. Note here, reversibility of the periodic orbit requires the $\mathbb{Z}_2$-symmetry maps the periodic orbit to itself. This is drawn schematically in Figure 3.3.

The key property leading to the existence of localised patterns is the assumed existence of fronts. We assume that there exists a heteroclinic connection between the rest state zero in backward x and the periodic orbit in forward x. While such a connection can be found numerically using approximation techniques, no formal proof of these structures currently exists. However, their presence is not unexpected. Looking inside the 3-dimensional zero energy level set, we have a 2-dimensional unstable manifold $W^u(0)$ and a 2-dimensional center-stable manifold $W^{cs}(\gamma(\cdot; \mu))$ which will have a 1-dimensional intersection generically. Meaning that if we have such an non-empty intersection for one value of μ this persists on a non-empty open interval.

By virtue of the reversibility, we also have a back solution. That is, a heteroclinic connection between the periodic orbit γ in backward x and the rest state in forward x. So we can naturally ask whether we can find a nearby homoclinic solution to

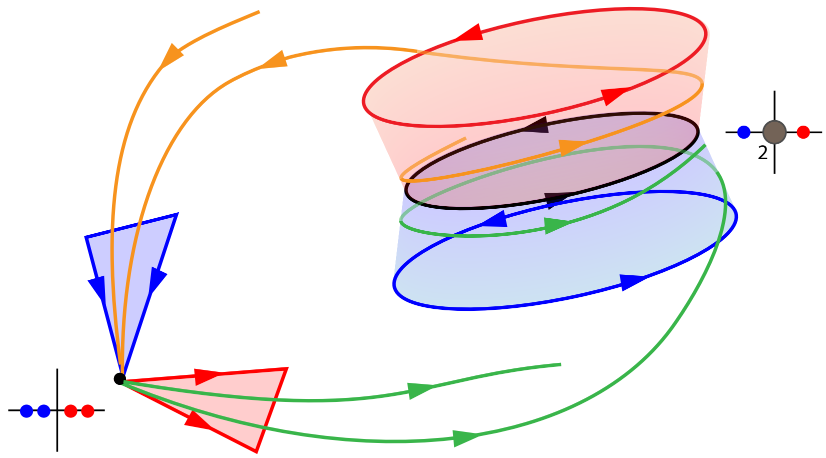

Figure 3.3: A schematic diagram of the fronts and backs in the scalar Swift-Hohenberg equation. In black are the rest state 0 and the periodic orbit u_{Tur} along with there stable and unstable manifolds in blue and red. The front and back are colored green and orange respectively.

zero that first follows the front into a neighbourhood of the periodic before leaving to follow the back and returning to the origin. Again by dimension counting we see that this constitutes an intersection between the two 2-dimensional manifolds $W^u(0)$ and $W^s(0)$ inside the 3-dimensional zero energy level set. Such an intersection is 1-dimensional generically, so we expect that such a homoclinic connection exists and can be continued in the bifurcation parameter μ.

Indeed, this turns out to be the case and, for fixed $\mu \in J$, you can find a discrete set of such homoclinic orbits indexed by an integer n (for n sufficiently large) corresponding to the number of revolutions the homoclinic connection makes while in transit of the periodic orbit. As already described these homoclinics are transverse and so persist under small variations in μ. To determine the global behaviour of the bifurcations, i.e. how these countably many branches connect together as we vary μ, we need to make global assumptions on the nature of the fronts. In particular, we assume that the bifurcation diagram of the fronts is periodic (and satisfying non-degeneracy conditions), in which case we observe snaking. Moreover, the snaking diagram can be qualitatively and quantitatively predicted (up to exponentially small terms) using the bifurcation diagram of the heteroclinic fronts.

This is not the full picture. Once we have made this global assumption on the existence of fronts, we can see that for each value of μ (away from the saddle-nodes) there are in fact two fronts and backs. Thus, we can also ask for homoclinic connections that follow one front and the other back (or vice versa). Doing so we find additional asymmetric homoclinic branches bifurcating at pitchfork bifurcations from the symmetric branches. Note that these pitchfork bifurcations are generic as they result from breaking the reversible symmetry. Continuing these branches globally, you find that that they in fact connect the two oppositely winding symmetric branches like rungs of a ladder. Again there is a simple algebraic condition using the bifurcation diagram of the fronts that qualitatively and quantitatively describes the behaviour of these branches, up to exponentially small errors.

Looking forward to the Brusselator, we need to consider whether the conservativity of the Swift-Hohenberg equation is essential. By considering the geometry already set up, we can see that this is not the case. If we ignore the conservative structure of the equation, then we see that a generic intersection of the 2-dimensional unstable manifold of the origin and the 3-dimensional center-stable manifold of the periodic orbit will be 1-dimensional. So even without the conservative structure, the front and back are generic connections and will have the same existence and robustness properties that we have assumed already. The difference is that to make those connections we have to use the second center-direction which parameterizes the family of periodic orbits. When looking for localised pulses, you need to be able to account for this additional degree of freedom.

3.2.2 Infinite Dimensional Problem

We can now extend this approach to the infinite dimensional case by treating the defects as heteroclinic connections between Turing and Hopf modes.

We consider reaction-diffusion equations of the form

$$u_t = Du_{xx} + f(u) \tag{3.2.3}$$

where the dependent variable $u \in \mathbb{R}^2$, D is a diagonal matrix with strictly positive entries and f is some suitable nonlinear function. We will give particular attention to the Brusselator in Section 3.7 which is the motivating example for this discussion.

Our main tool is to think of defect solutions as connecting orbits in a spatial dynamical system. In (3.2.3), we set $w = \partial_x u$ to find

$$\begin{aligned} u_x &= w \\ w_x &= D^{-1}(u_t - f(u)) \end{aligned} \tag{3.2.4}$$

a dynamical system on the phase space $X = H^{1/2}_{per}(S^1, \mathbb{R}^2) \times L^2_{per}(S^1, \mathbb{R}^2)$ where $S^1 = \mathbb{R}/2\pi\mathbb{Z}$. This is not well-posed as an initial value problem, however, we can construct exponential dichotomies and invariant manifolds to the Turing and Hopf modes (see for instance Sandstede and Scheel (2004)). Taking this perspective, defect solutions become heteroclinic connections between equilibria which lie near heteroclinic fronts and backs.

Using the spatial coordinate x as the independent variable, we are able to describe (at lease schematically) the geometry of the problem in the same terms as the localised pulses. The asymptotic wavetrains become circles of relative equilibria, topologically S^1, with an S^1-symmetry given by translations in time. Moreover from Sandstede and Scheel (2004) we know precisely the spectrum of the background wavetrains depending on their group velocities. For contact defects these circles have a two dimensional centre subspace and all other spectrum bounded away from the imaginary axis.

Simultaneously the family of Turing patterns become families of periodic orbits sitting in the subspace of temporally constant functions. In particular this means they are in the fixed space of the time-translation operator. Also we know that generically Turing patterns (viewed as periodic orbits of a reversible system) come in a one parameter family parameterized by their wavelength (Vanderbauwhede and Fiedler, 1992, Devaney, 1977). This is reflected in their spectrum as a second Floquet exponent at zero. So we get an invariant cylinder of patterns representing candidate core regions for our defect solution.

We then assume that we have heteroclinic connections joining the background oscillations and the Turing patterns (and vise versa) which we will call fronts (and backs) from now on. Now we are in the set up of homoclinic snaking. Defect solutions correspond to homoclinic connections in close proximity to the heteroclinic cycle of fronts and backs. However, at this point we need to take careful note of the geometry.

To build some intuition, we first look at a simpler situation where we imagine truncating the dimensions of our problem to keep only the bare essentials, see Figure 3.9. For our purposes this will mean considering the 6-dimensional subspace consisting of the 6 "weakest" directions. Intuitively speaking, assuming no higher codimension bifurcations occur, all important information is contained in these central dimensions. When it comes to actually proving our results, we must be careful as the problem is truly infinite-dimensional and we cannot hope to reduce the prob-

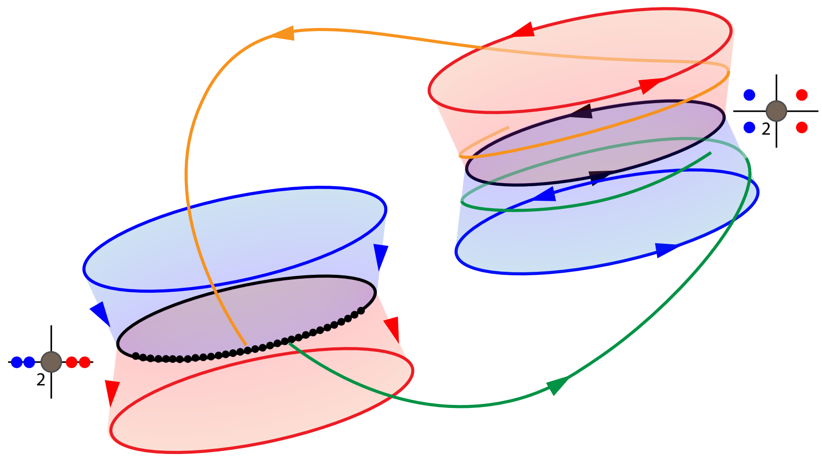

Figure 3.4: A schematic diagram of the fronts and backs in the reaction-diffusion case when looking for contact defects. In black are the rest state equilibria (Hopf modes) and a single periodic orbit (Turing pattern) u_{Tur} along with their stable and unstable manifolds in blue and red. Representative fronts and backs are colored green and orange respectively.

lem to a finite-dimensional system in general. However, the intuition of this model is essential in formulating the transversality and general position assumptions in our rigorous framework. Now that we are in finite dimensions we are able to employ dimension counting arguments.

First consider the symmetric contact defect case. Note that we expect the existence of a 1-parameter family of fronts. Indeed we have a 4-dimensional center-unstable manifold of the homogeneous oscillation intersecting the 4-dimensional center-stable manifold of the Turing patterns in $\mathbb{R}^6$. Such an intersection generically has dimension 2. Thus, we have a 1-parameter family of fronts where we expect the family to be parameterised by time translations. At the same time we expect that defect solutions to also come in 1-parameter families as both the center-stable and center-unstable manifolds of the homogeneous oscillations are 4-dimensional.

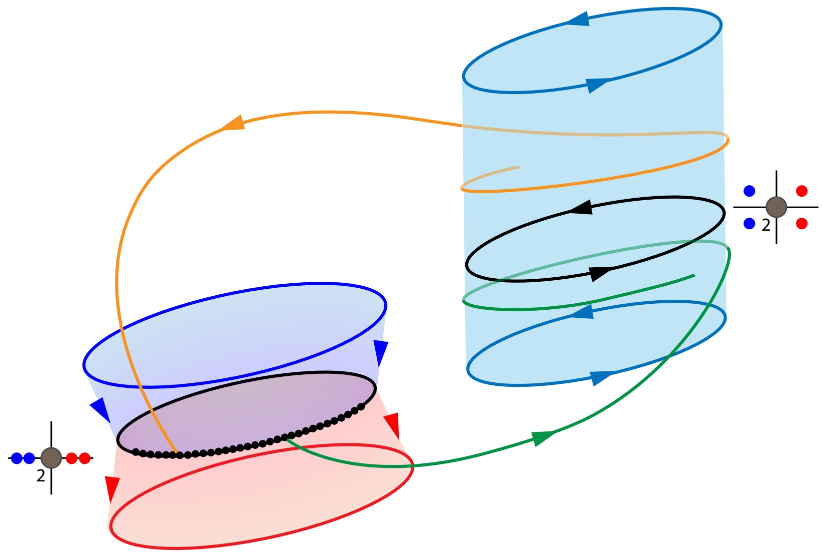

Figure 3.5: A schematic diagram of phase space when making connections between fronts and back selecting different Turing wavenumbers κ. The Turing patterns form an invariant cylinder with each horizontal slice a Turing pattern. Heteroclinic connections will generically select different Turing patterns without additional structure.

We can then imagine trying to find asymmetric connections between two distinct fronts as in the Swift-Hohenberg case. However, here we find a problem. Generically fronts at different points on the bifurcation diagram will have core regions with different wavenumbers, as pictured in Figure 3.5. As demonstrated above, our generic intersection for the fronts includes the center direction corresponding to the Turing wavenumber, meaning we should expect the fronts to have different core wavenumbers. The problem is that in the stationary laboratory frame, the dynamics on this cylinder are trivial, consisting of invariant circles of fixed wavenumber. So there is no way to move from a front with one wavenumber to a back with a different wavenumber. We have to move to a new co-moving frame for some small, to be determined, wave number c in order to make such a connection. This means that our generic intersection will have additional dimension, not corresponding time translation. Instead this corresponds to shear translations. So we find a family of asymmetric contact defects, parameterised by the phase offset of the background oscillations.

From a spatial dynamical systems viewpoint this is both unexpected and a critical feature. It is unexpected because in most applications one does not find defect solutions with arbitrary phase offsets. The typical scenario is that there is a weak coupling between the background oscillations that pin their phases to either be in-phase or our of phase by exactly half a wavelength, thereby producing only target and spiral defects. In this case, we actually find that there are solutions corresponding to each phase offset which interpolate between the spiral and target states.

On the other hand, this observation is also critical it making these results consistent with the robustness properties of contact defects. When c becomes non-zero, we also perturb the dynamics of the asymptotic homogeneous oscillations, as well as on the family of Turing patterns. That is, by moving into a comoving frame, we must now allow ω to vary so that we still have a contact defect. See Section 3.3 for a discussion of this phenomenon. Consequently, the background states become wavetrains with a well-defined but small spatial wavenumber k which will be parameterised by the phase offset. This is important because Sandstede and Scheel (2004) showed that contact defects are found in 1-parameter families generically, indicating that we should expect that there are many more solutions than were found in the numerical experiments by Tzou et al. (2013). Locally near the core region, the background oscillations will look like homogeneous oscillations due to their very large spatial wavelength. This will be explained in more detail below.

These observations lead to our main results on contact defects.

Theorem 3.2.1 (Symmetric Contact Defects)**.** *Suppose Hypotheses 3.4.1, 3.4.3, 3.4.4, 3.4.7 and 3.4.8 hold. In particular, there are periodic functions* $z : S^1 \mapsto J$ *and* $\kappa^* : S^1 \to K$ *for interval* $J, K \subset \mathbb{R}$ *describing the bifurcation diagram of the front and the selected core Turing wavenumber selected by each front respectively. Then for*

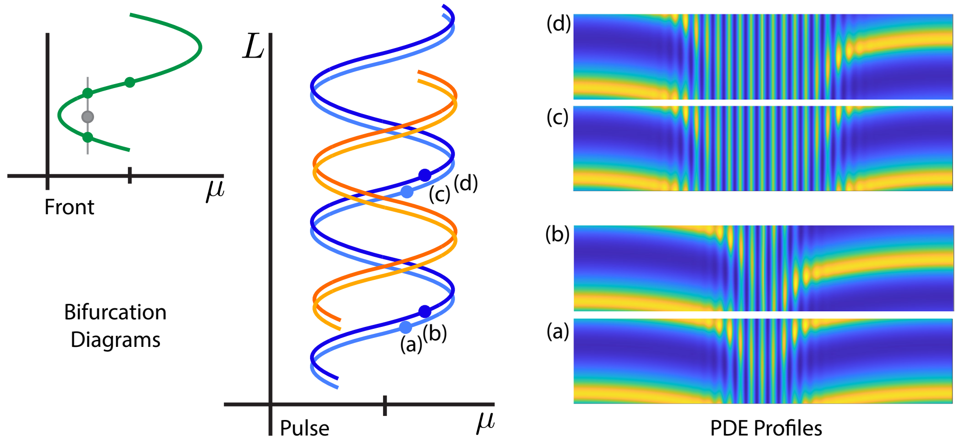

Figure 3.6: The bifurcation diagram for symmetric contact defects. There are two pairs symmetric branches that snake as the bifurcation parameter is varied. One pair are 1-dimensional targets and the other are 1-dimensional spirals. These branches differ from each other only exponentially small terms.

every $n \in \mathbb{Z}$ large enough, $\varphi \in S^1$ and $\varphi_0 \in \{0, \pi\}$ there exists a unique symmetric defect solution with core region of width $(2\pi n + \varphi_0 - \varphi)/\kappa^*(\varphi)$ for parameter value $\mu = z(\varphi) + \bar{\mu}$ where $\bar{\mu} = \mathcal{O}(e^{-\eta n})$ for some $\eta > 0$.

The bifurcation diagram of the symmetric contact defects consists of four distinct branches. One pair of these branches correspond to the symmetric branches found for the Swift-Hohenberg equation. Each branch is a copy of the periodic extension of the bifurcation diagram of the fronts up to terms exponentially small in the width of the core region, but are offset by half a period. As such, the branches consist of a tower of saddle-node bifurcations produced by the local minima and maxima of the function z.

The other pair of branches correspond to the same snaking diagram but with a second reversible symmetry. There are two distinct reversible symmetries in our problem formed by composing the first reverser with a translation in time by half a wavelength, as we will discuss in Section 3.4. Theorem 3.2.1 applies to both reversers individually meaning we in fact have four distinct symmetric branches. In the Brusselator, the first two have even symmetry at the origin while the second have odd symmetry and background oscillations out of phase by half a period.

Theorem 3.2.2 (Asymmetric Contact Defects)**.** *Again suppose Hypotheses 3.4.1, 3.4.3, 3.4.4, 3.4.7 and 3.4.8 hold. In addition also assume Hypothesis 3.4.9 holds. In particular we again have the function z and κ^*, but also we can find pairs of phases $\varphi_1, \varphi_2 \in S^1$ such that $z(\varphi_1) = z(\varphi_2)$. Then for every $n \in \mathbb{Z}$ large enough, (φ_1, φ_2) sufficiently far from the local minima and maxima of z, and $\alpha \in S^1$, there exists a unique asymmetric defect solution whose core region has width L and which has a phase offset of α in their background oscillations. These defects will exist for a parameter value $\mu = z(\varphi_1) + \bar{\mu}$ where $\bar{\mu} = \mathcal{O}(\Delta\kappa/L + e^{-\eta L})$, will move at a speed $c^*(\Delta\kappa, \alpha) = \Delta\kappa/2L + \mathcal{O}(e^{-\eta L})$ and have temporal frequency $\omega = \omega_0 + Bc^2 + \mathcal{O}(c^4)$ where $\Delta\kappa = \kappa(\varphi_2) - \kappa(\varphi_1)$ is the difference in wavenumber between the selected front and back, ω_0 is the temporal frequency of the homogeneous oscillation and B is an $\mathcal{O}(1)$-constant.*

When we add the asymmetric solutions to the bifurcation diagram we obtain Figure 3.7, where we plot only a single half period of the snaking diagram for clarity. In addition to the symmetric solutions we have already found, there are four tubular families of asymmetric defects. Two of these families contain the symmetric defects, with the circular cross-section being parameterised by the phase offset $\alpha \in S^1$. Each defect will travel at a wavespeed which is exponentially small in the length of the core region L, but only the symmetric defects are guaranteed to have wavespeed zero. These families interpolate between the 1-dimensional target and spiral patterns. The remaining two families correspond to the asymmetric rung solutions found in the case of stationary localised patterns. These patterns will travel at a wavespeed

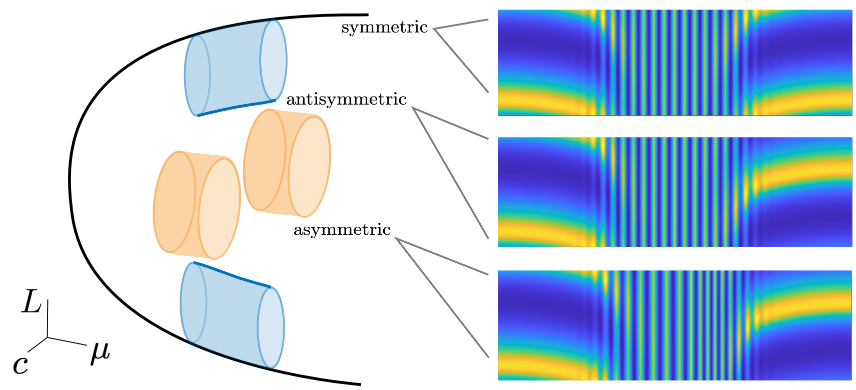

Figure 3.7: A segment of the bifurcation diagram for asymmetric contact defects away from the symmetric saddle-nodes. There are four tubular families of asymmetric defect solutions with the circular cross-sections parameterised by the defect phase offset α. Two of these families correspond to the symmetric branches already found which interpolate between the spiral and target defects. The other two have asymmetric cores and correspond to the asymmetric rung branches in the Swift-Hohenberg equation.

proportional to the difference in spatial wavenumber of the selected Turing pattern and inversely proportional to width of the core region. This means as you approach the symmetric saddle-nodes, or move up the snaking diagram, the wavespeed of the asymmetric defects tends to zero.

3.3 Spatial Dynamics of Wavetrains and Defects

In the previous section, we noted that the essential information concerning snaking bifurcations comes from looking at a reduced 6-dimensional model equation. Of particular importance is the identification of the spatial spectra of the wavetrains and Turing patterns from which we derive our geometrical understanding of this problem. In this section, we summarize the rigorous mathematical results underpinning this discussion. We also highlight the relevant properties of the underlying wavetrains that will be important in formalising the full asymmetric defect problem.

3.3.1 Wavetrains and Homogeneous Oscillations

We start by considering wavetrain solutions in reaction diffusion systems which represent the asymptotic background states of our defects. Recall our reaction diffusion equation is

$$u_t = Du_{xx} + f(u).$$

A wavetrain solution is a 2π-periodic solution $u_{\mathrm{wt}}(\phi)$ solving the equation

$$k^2 D\partial_{\phi\phi}u - \omega\partial_\phi u + f(u) = 0 \tag{3.3.1}$$

where k is the wavenumber and ω is the temporal frequency. By using the coordinate frame $\phi = kx - \omega t$, this generates a solution to the reaction diffusion equation $u(x,t) = u_{\mathrm{wt}}(kx - \omega t)$.

Under generic assumptions on the spectra of such a wavetrain found for $(k,\omega) = (k_0,\omega_0)$, there is a nearby smooth family of wavetrains $u_{\mathrm{wt}}(\phi;k)$ such that $u_{\mathrm{wt}}(\phi;k_0)$ is the original wavetrain with frequency ω_0 and the family have frequencies determined by $\omega = \omega_{nl}(k)$. The function ω_{nl} is called the nonlinear dispersion relation of the wavetrains u_{wt}, and from it we can obtain the phase and group velocities $c_{\mathrm{p}} = \omega_{nl}/k$ and $c_{\mathrm{g}} = \partial_k\omega_{nl}(k)$ respectively. The phase velocity is the natural speed at which the pattern moves as a whole. The group velocity is the natural speed at which localised perturbations propagated by the wavetrain. These quantities are deeply related to the temporal and spatial spectrum of the wavetrains.

The associated linearization of the reaction diffusion system in the coordinates

$\phi = kx - \omega t$ about the wavetrain is then given by

$$u_t = k^2 D \partial_{\phi\phi} u - \omega \partial_\phi u + f'(u_{\mathrm{wt}}(\phi; k))u. \tag{3.3.2}$$

The linear operator defined by the right-hand side, $\mathcal{L}_0$, is not Fredholm on $L^2(\mathbb{R})$ since by differentiation one can show that $\partial_\phi u_{\mathrm{wt}}(\phi; k)$ is a bounded solution in its kernel, hence, the operator is not closed by Weyl-sequence arguments. Instead, spatial Floquet theory (Mielke, 1996, Peterhof et al., 1997) shows that you can compute the spectrum through a Fourier-Bloch ansatz. That is, we substitute $u(\phi) = \exp(\nu\phi/k)v(\phi)$ where v is a 2π-periodic function to obtain

$$\mathcal{L}_\nu v := k^2 D(\partial_\phi - \nu/k)^2 v - \omega(\partial_\phi - \nu/k)v + f'(u_{\mathrm{wt}}(\phi, k))v. \tag{3.3.3}$$

For each $\nu \in i\mathbb{R}$, $\mathcal{L}_\nu$ is a closed operator on $L^2_{per}(S^1)$ densely defined on $H^2_{per}(S^1)$. As such it has a compact resolvent and its spectrum is discrete. The temporal Floquet exponents $\lambda \in \mathbb{C}$ of $\mathcal{L}_0$ are then determined to lie exactly on a discrete number of curves $\lambda_j(\nu)$ of the complex plane which correspond exactly to situations where the temporal eigenvalue problem, $\mathcal{L}_\nu v = \lambda v$, has a spatial Floquet exponent on the imaginary axis. Moreover, assuming that $\mathcal{L}_0$ has a simple eigenvalue exponent at the origin, exactly one such curve has $\lambda(0) = 0$. For small values of $\nu \in i\mathbb{R}$ we call this curve the linear dispersion relation λ_{lin}.

Using Taylor expansion arguments (Doelman et al., 2009) one can show that the linear and nonlinear dispersion relations are related through the group velocity c_{g} as

$$\omega_{nl}(k) = \omega(k_0) + c_{\mathrm{g}}(k_0)k + \mathcal{O}(k^2) \tag{3.3.4}$$

$$\lambda_{lin}(\nu) = (c_{\mathrm{p}} - c_{\mathrm{g}}(k_0))\nu + d_{||}^2\nu^2 + \mathcal{O}(\nu^3) \tag{3.3.5}$$

for k close to k_0 and ν close to 0. The c_p term in the expansion of λ_{lin} appears as we have computed the dispersion relation in the comoving frame $\phi = kx - \omega t = k(x - c_\mathrm{p} t)$.

Through equation (3.3.5) we see that there is a direct link between the temporal stability properties of the wavetrain, its phase and group velocities, and its spatial Floquet exponents. This connection can be used to characterise the spatial spectrum of wavetrains based on their group velocities. This is essential information, as it shows that defects will have very different properties based on their group velocities.

We will return to the spatial spectrum, in a moment. First we consider a special case of wavetrains which are central to our discussion here - spatially homogeneous oscillations.

A spatially homogeneous oscillation is a solution $u_h(t)$ which satisfies

$$\omega u_t = f(u), \quad u(0) = u(2\pi) \tag{3.3.6}$$

where we have rescaled the time variable by the minimal period $T = \omega^{-1}$. By definition such a solution also solves (3.3.1) with spatial wavenumber $k = 0$ and frequency ω equal to the true temporal frequency of the periodic profile. We claim that nearby such a spatially homogeneous oscillation, we can find a family of wavetrain solutions with small wave numbers k.

Lemma 3.3.1. *Assuming the periodic orbit u_h has a simple temporal Floquet multiplier $\rho = 1$, then there exists a family of wavetrain solutions nearby the homogeneous oscillation. Moreover, the Taylor expansion formulas* (3.3.4)*and* (3.3.5) *hold, and* *due to the* $k \mapsto -k$ *symmetry of* (3.3.1)*, we have*

$$\omega_{nl}(k) = \omega_0 + \omega_0'' k^2 + \mathcal{O}(k^4) \tag{3.3.7}$$

$$\lambda(\nu) = d_{||}^2 \nu^2 + \mathcal{O}(\nu^3) \tag{3.3.8}$$

Equation (3.3.1) is singularly perturbed in the limit as k tends to zero, so the natural strategy to prove this result is though geometric singular perturbation theory (Fenichel, 1979). The original periodic orbit is hyperbolic and lies in the critical manifold for $k = 0$. One can use this to reduce the problem to a first order flow on a slow manifold which can be treated using regular perturbation theory. Interestingly, we are not aware of any elementary proof of this lemma that avoids singular perturbation theory. This is due to equation (3.3.1) being singularly perturbed in the limit as k tends to 0. Or put another way, homogeneous oscillations are wavetrains with infinite phase velocity. They can be continued using perturbative techniques, but such perturbations are no longer regular and require additional machinery from Fenichel Theory.

Of particular note is that the nonlinear dispersion relation is quadratic in k near zero and the linear dispersion relation is quadratic in ν. Note also, in this case we compute the linear dispersion relation in the stationary frame, as c_p is not defined in the limit as k tends to zero. Thus, homogeneous oscillations (and more generally any situation where group and phase velocity are zero) have distinct spectral properties.

Finally we note that we are ultimately interested in solutions to the reaction-diffusion equation with a uniform transport term found by changing variables into a comoving frame,

$$u_t = Du_{xx} + c_d u_x + f(u), \tag{3.3.9}$$

as we will need to allow our defect patterns to move at a non-zero wave speed c_d for the purposes of matching. Note that a wavetrain solution of (3.3.1) (including a homogeneous oscillation) will also generate a periodic wavetrain solution of the reaction diffusion equation in the comoving frame given by $u(x,t) = u_{\mathrm{wt}}(kx - (\omega - c_d k)t; k)$, with spatial wavenumber k. The wavetrain now has a different nonlinear dispersion relation given by $\omega_d = \omega_{nl}(k) - c_d k$, and as such a new phase and group velocity: $\tilde{c_{\mathrm{p}}} = c_{\mathrm{p}} - c_d$ and $\tilde{c_{\mathrm{g}}} = c_{\mathrm{g}} - c_d$. However, the relative difference between these quantities remains invariant.

3.3.2 Exponential Dichotomies and Invariant Manifolds

So far we have described the spectral properties of periodic solutions to reaction diffusion equations. However, we have done so in the parabolic formulation of the problem. In order to leverage dynamical systems arguments, we need access to dynamical information of the elliptical formulation,

$$u_x = w, \tag{3.3.10}$$

$$w_x = D^{-1}(\omega_d u_\tau - c_d w - f(u)), \tag{3.3.11}$$

where we recall that the relevant phase space is $X = H^{1/2}_{per}(S^1, \mathbb{R}^2) \times L^2_{per}(S^1, \mathbb{R}^2)$ and we have rescaled time to $\tau = \omega_d t$ to ensure we have 2π-periodic solutions in τ.

The temporal Floquet problem for the linearization of this system around our known wavetrain solution, $(u_{\mathrm{wt}}(kx - \tau), k u_{\mathrm{wt}}(kx - \tau))$, is

$$u_x = w, \tag{3.3.12}$$

$$w_x = D^{-1}(\omega_d \partial_\tau u - c_d v - f'(u_{\mathrm{wt}}(kx - \tau; k))u + \lambda u). \tag{3.3.13}$$

Again calling on spatial Floquet theory (Sandstede and Scheel, 2004, Mielke, 1996), for every $\lambda \in \mathbb{C}$ the dynamical system (3.3.12)-(3.3.13) posed on the phase space X, has an exponential trichotomy. That is, there exist smooth projection maps $P^u_{\rm wt}(x_0,\lambda)$, $P^s_{\rm wt}(x_0,\lambda)$ and $P^c_{\rm wt}(x_0,\lambda)$ mapping $X \to X$ such that

- $P^u_{\rm wt} + P^s_{\rm wt} + P^c_{\rm wt} = I$,
- $Rg(P^u_{\rm wt}(x_0,\lambda))$ is the set of initial conditions at $x = x_0$ for which the dynamical system (3.3.12)-(3.3.13) converges to 0 as $x \to -\infty$,
- $Rg(P^s_{\rm wt}(x_0,\lambda))$ is the set of initial conditions at $x = x_0$ for which the dynamical system (3.3.12)-(3.3.13) converges to 0 as $x \to \infty$, and
- $Rg(P^c_{\rm wt}(x_0,\lambda)$ is the set of initial data at $x = x_0$ for which the dynamical system (3.3.12)-(3.3.13) remains bounded for all $x \in \mathbb{R}$.

Moreover, the ranges of $P^u_{\rm wt}$ and $P^s_{\rm wt}$ are infinite-dimensional, while the range of $P^c_{\rm wt}$ is finite-dimensional.

Also note that when $\lambda = 0$ the temporal Floquet problem is really just the linearization of the wavetrain itself. So this establishes the existence of exponential trichotomies for the wavetrain. In particular, by using exponential weighting arguments as needed, it is possible to construct centre-stable and center-unstable manifolds to the wavetrain $u_{\rm wt}(kx - \tau; k)$, both of which are infinite-dimensional.

The infinite dimension of these manifolds is essential and results from the fact that the elliptic problem (3.3.11) is ill-posed as an initial value problem on the phase space X. In order to recover the finite-dimensional model system described in Section 3.2.2, we need to be careful.

Excluding higher-codimension bifurcations occurring, we should expect that our defects converge to their asymptotic wavetrains along their weakest stable and unstable directions. So while the center-stable and center-unstable manifolds are infinite-dimensional, we should expect that all the information about our bifurcation can be captured by a finite-dimensional submanifold corresponding to said weakest directions. This is part of what we will show in the following sections. To get an accurate picture of the system, we need to understand the structure of the spatial Floquet exponents closest to the imaginary axis.

Note that τ parameterizes a temporal phase shift of the wavetrain, and for each $\tau \in S^1$ the wavetrain defines a relative fixed point of the elliptic problem (3.3.11) with S^1-symmetry provided by the temporal translation. This will correspond to a spatial Floquet exponent of zero, and any center manifold will include all time translates of the base wavetrain. The question is then, what are the next closest spatial Floquet exponents.

The answer depends on the group velocity of the wavetrain, c_{g}, and the defect wavespeed c_d.

Lemma 3.3.2 (Sandstede and Scheel (2004) Lemma 3.6)**.** *Assume the following generic conditions on the wavetrain u_{wt} are met:*

- *the origin $\lambda = 0$ is an algebraically simple eigenvalue of $L^2_{per}(S^1)$ with eigenfunction $\partial_\phi u_{\mathrm{wt}}$,*
- *the linear dispersion relation has $d_{||} > 0$,*
- *the wavetrain is temporally stable i.e. with the exception of the spectrum near $\lambda = 0$ (given by the linear dispersion relation) its spectrum is contained in the open left half-plane, and*

- *the nonlinear dispersion relation is genuinely nonlinear i.e.* $\omega''_{nl}(k_0) = \omega''_0 \neq 0$.

Then the spatial dynamical system (3.3.12)-(3.3.13) *has a geometrically simple Floquet exponent* $\nu = 0$ *for* $\lambda = 0$. *This Floquet exponent is also algebraically simple if* $c_d \neq c_{\mathrm{g}}$, *while it has algebraic multiplicity two if* $c_d = c_{\mathrm{g}}$.

A direct result of this Lemma is that, near the origin, we have the spatial Floquet spectrum pictures shown in Figure 3.8. With the exception of the first zero Floquet exponent and the second closest Floquet exponent, which moves across zero as c_d is varied through the group velocity, the remaining Floquet spectra are distributed evenly in the right and left half-planes. They also remain bounded away from the imaginary axis.

The set up for the proof of this Lemma is technical, but is based on the following idea. It can be shown that you can obtain the spatial Floquet spectrum for $\lambda = 0$ by using a homotopy argument from a fixed reference λ^* with very large real part. A rescaling of x in (3.3.12)-(3.3.13) by a factor λ^* shows that the inhomogeneous parts are strongly dominated by the autonomous contributions, and the spatial spectrum can be computed analytically in this case. What remains is to determine how many spatial Floquet exponents cross zero during the homotopy. This can be achieved using Fredholm properties of specific projection operators. The stability assumption on the wavetrain heavily curtails when and how these exponents can cross the imaginary axis, and this results in the Figures displayed in Figure 3.8.

The results of the Lemma also holds for homogeneous oscillations, if we replace the first assumption with the condition assumed in Lemma 3.3.1. That is, that the homogeneous oscillation has a simple temporal Floquet exponent at zero. Since this also implies the existence of nearby wavetrains with small spatial wavenumber, this

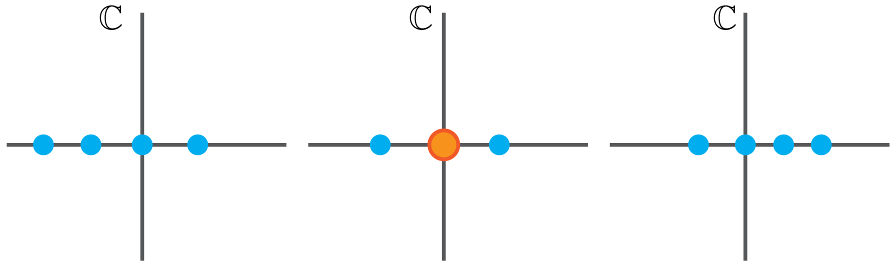

Figure 3.8: The spatial spectrum of wavetrains near the origin for the three cases: (a) $c_{\mathrm{g}} < c_d$, (b) $c_{\mathrm{g}} = c_d$ and (c) $c_{\mathrm{g}} > c_d$.

means that for any small enough wavespeed c_d we can find a wavetrain u_h with spatial number k and temporal frequency $\omega(k)$ with group velocity c_d.

Lemma 3.3.3. *Assume that the hypothesis of Lemma 3.3.2 hold for the homogeneous oscillation u_h. Then for every c close enough to zero there exists a wavenumber k such that $u_h(\cdot;k)$ is a wavetrain with temporal frequency $\omega(k)$ and group velocity c. Moreover, we have leading order expansions*

$$k = \frac{c}{2\omega_0''} + \mathcal{O}(c^2), \tag{3.3.14}$$

$$\omega(c) = \omega_0 + \frac{c^2}{4\omega_0''} + \mathcal{O}(c^4). \tag{3.3.15}$$

Proof. From Lemma 3.3.1, we know that the nonlinear dispersion relation of the family of wavetrains generated near the homogeneous oscillation is given by

$$\omega(k) = \omega_0 + \omega_0'' k^2 + \mathcal{O}(k^4), \tag{3.3.16}$$

and differentiating with respect to k we obtain the group velocity

$$c_{\mathrm{g}}(k) = 2\omega_0'' k + \mathcal{O}(k^3). \tag{3.3.17}$$

We solve the equation $c_{\mathrm{g}} = c$ using the Implicit Function Theorem which also yields the expansions state above. $\square$

This is the crucial property that will allow us to construct asymmetric contact defects, as the additional center-direction produced by the group velocity condition is necessary for necessary for their formation.

3.3.3 Geometry and Robustness of Contact Defects

Recall that we have loosely defined a defect solution to (3.3.9) to be a solution asymptotic to wavetrains for $x \to \infty$. Formally, this is a solution $u = u_d(x, \tau)$ which is 2π-periodic in $\tau = \omega_d t$ and for which there exist asymptotic wavenumbers $k_\pm$ and asymptotic phase functions $\theta_\pm : \mathbb{R} \to S^1$ such that

$$|u_d(x, \tau) - u_{\mathrm{wt}}(k_\pm x - \tau + \theta_\pm(x); k_\pm)| \to 0 \tag{3.3.18}$$

as $x \to \pm\infty$. Note that we allow the defects to be asymptotic to wavetrains with distinct wavenumbers $k_\pm$ and we require the phase function $\theta_\pm$ to allow for the asymptotic wavetrains to be phase shifted against each other. Suppose that we find $\theta_\pm$ to be constants for the moment. In the parlance of spiral and target waves, $\theta_+ - \theta_- = 0$ modulus 2π gives a 1-dimensional target pattern, while $\theta_+ - \theta_- = \pi$ modulus 2π gives a 1-dimensional spiral wave. However, we will see that we cannot ask these functions to be constant in general. We will return to this in a moment.

Using the results of the previous section, we can think of defects as being heteroclinic orbits in the phase space X which connect different wavetrain solutions. What we have also seen is that the spatial spectrum closest to the origin is determined by the difference between the group velocity of the wavetrains and the defect wavespeed. This allows us to classify the generic forms of defects based on the group velocities of their asymptotic wavetrains (Sandstede and Scheel, 2004). For our discussion here, we are interested in contact defects, which have $c_{\mathrm{g}}^{\pm}$ equal to the defect speed c_d.

From the previous section, such wavetrains will have a spatial spectrum as shown in Figure 3.8(b), that is an algebraic multiplicity-2 Floquet exponent zero with balanced stronger spectrum. The defect solution then corresponds to a homoclinic connection to the family of wavetrains as shown in Figure 3.9. They are also saddle-node homoclinic connections in the sense that they are formed in the two-dimensional center manifold of the circle of relative equilibria.

This observation is made rigorous by the analysis in Sandstede and Scheel (2004). It has two implications for us. First, analysis of the convergence of contact defects to their asymptotic wavetrains shows at best algebraic decay and requires that the phase function θ be an unbounded, monotonically increasing function Sandstede et al. (2004). In fact, $\theta(x)$ is asymptotically logarithmic. This is an important consideration when constructing a numerical scheme to approximate these patterns.

Second, this also means that the center direction is involved in both the unstable and stable dynamics, and counts towards both in the intersection. As a result, in our 6-dimensional model, we see that contact defects come in robust 1-parameter families for fixed system parameters. Moreover, generically they can be shown to be families parameterised by the asymptotic wavenumber $k = k_{\pm}$ (Sandstede and Scheel, 2004, Lemma 5.6).

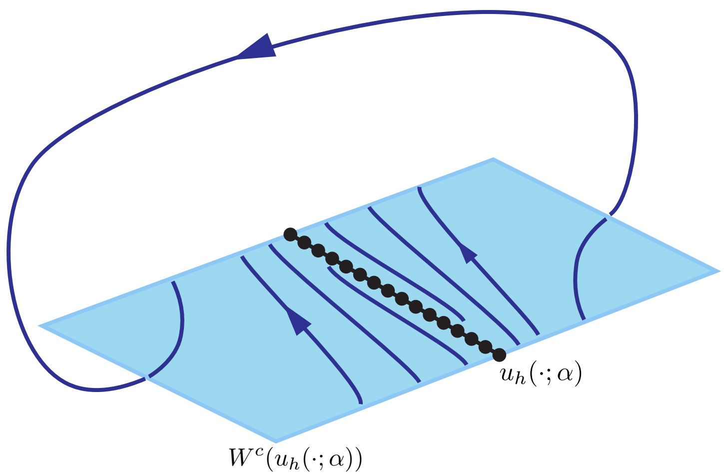

Figure 3.9: The geometry of contact defects in the phase space X. Contact defects are homoclinic connections to the invariant circle of relative equilibria made through the two-dimensional center manifold.

3.3.4 Turing Patterns

Finally we also note the existence and spatial spectrum properties of Turing patterns. Turing patterns are temporally homogeneous, spatial oscillations that solve

$$0 = Du_{xx} + f(u) \tag{3.3.19}$$

and are periodic in x. Let κ denote the spatial wavenumber of the Turing pattern. This equation is symmetric under the mapping $x \mapsto -x$ and hence reversible. Any periodic orbit in x, or Turing pattern, will generically be found in a 1-parameter family of periodic orbits parameterised by their wavenumber κ due to reversibility (Devaney, 1977, Vanderbauwhede and Fiedler, 1992). Note to distinguish between the spatial wavenumber of the background oscillations and and the spatial wavenumber of the Turing patterns we label them k and κ respectively.

We want to know the spatial Floquet spectrum as a solution to the elliptic problem on the phase space X. Linearizing our reaction-diffusion equation (3.3.9) with wavespeed $c_d = 0$, we find

$$u_x = w, \tag{3.3.20}$$

$$w_x = D^{-1}(\omega_d \partial_\tau u - f'(u_{\mathrm{Tur}}(x;\kappa))u) \tag{3.3.21}$$

which a spatial Floquet exponent zero with geometric multiplicity one with a bounded eigenfunction $(u'_{\mathrm{Tur}}, \kappa u''_{\mathrm{Tur}})$. This exponent has algebraic multiplicity 2 which creates a Jordan block corresponding to the family of Turing patterns. Hence, the center-manifold is 2-dimensional. We can determine the remaining Floquet exponents by using a Floquet ansatz, $(u, w) = e^{\lambda x}(\bar{u}, \bar{w})$ for $2\pi/k$-periodic functions $\bar{u}$ and $\bar{w}$. That is, we want to solve

$$\bar{u}_x = \bar{w} - \nu \bar{u} \tag{3.3.22}$$

$$\bar{w}_x = D^{-1}(\omega \partial_t - f_u(u_{Tur}(x;\kappa)))\bar{u} - \nu \bar{w} \tag{3.3.23}$$

for $(\bar{u}, \bar{w})$ as $2\pi/k$-periodic functions. We can simplify these equations by taking a temporal Fourier transform which decouples the system into countably many, 4-dimensional subproblems for the Fourier coefficients of each order. The identified center Floquet multipliers lie in the temporally homogeneous subspace.

When we move into the co-moving frame, things look different. While it is true that we can find solutions of the form $u(x, \tau) = u_{\mathrm{Tur}}(x + c\tau/\omega_d; \kappa)$ of the reaction diffusion equation (3.3.9), they are no longer 2π-periodic in τ and, hence, not in the phase space X. Instead we note that the 2-dimensional center manifold is normally hyperbolic when $c_d = 0$, and so will perturb to a new invariant 2-dimensional manifold for small c_d, whose dynamics we can express using a Fenichel Normal form. The resulting manifold will no longer be made up of periodic orbits, but will generate a modulational drift in the Turing wavenumber that will allow us to produce asymmetric defects.

3.4 Set up and Hypotheses

We begin by setting the ground for the proofs of Theorems 3.2.1 and 3.2.2. These can broadly be divided into two groups: local assumptions on the Turing family and background states; and global assumptions on the how the background states interact with a neighbourhood of the Turing family via their invariant manifolds. For the remainder of this section we will simplify our notation so that (3.2.4) is written as

$$\mathbf{u}_x = F(\mathbf{u}; \mu, c, \omega) =: A(\mu, c, \omega)\mathbf{u} + N(\mathbf{u}; \mu) \tag{3.4.1}$$

where $\mathbf{u} = (u, w)^T$, A is the linear part, N the remaining nonlinear terms and μ is our primary bifurcation parameter. The system parameters c and ω will be chosen in neighbourhoods of 0 and ω_0 respectively. We will consider μ to take values in a interval of $\mathbb{R}$ with non-empty interior J.

Hypothesis 3.4.1 (Exponential Dichotomies)**.** We assume there exists a constant C such that

$$||(ik - A(\mu, c, \omega))^{-1}||_{L(X)} \leq \frac{C}{|k| + 1} \tag{3.4.2}$$

for all $k \in \mathbb{R}$. We also assume that there exists a $\delta > 0$ such that $|\Re\lambda| > \delta$ for all $\lambda \in \sigma(A)$.

Hypothesis 3.4.1 is a technical assumption required to guarantee the existence, continuation and perturbation of exponential dichotomies (Peterhof et al., 1997) as described in Section 3.3. All our following results, including existence of invariant manifolds, Fenichel normal form and exchange lemma, require the presence of exponential dichotomies and hence this assumption. We will not directly use this in our analysis.

To begin in earnest we note that our system (3.2.4) is spatially-reversible and temporally-equivariant under two distinct symmetry operations which will play key roles for our framework, so we give precise definitions below.

Definition 3.4.2 (Reversibility and Equivariance)**.** The dynamical system (3.4.1) is **reversible** if there exists an involution $\mathcal{R} : X \to X$ such that $F(\mathcal{R}\mathbf{u}; \mu) = -\mathcal{R}F(\mathbf{u}; \mu)$ for all $\mathbf{u} \in X$. The dynamical system (3.4.1) is **equivariant** with respect to a family of transformations $\Gamma_\alpha : X \to X$ for $\alpha \in S^1$ if $F(\Gamma_\alpha \mathbf{u}; \mu) = \Gamma_\alpha F(\mathbf{u}; \mu)$ for all α in S^1 and $\Gamma_\alpha \circ \Gamma_{\tilde{\alpha}} = \Gamma_{\alpha+\tilde{\alpha}}$ for all $\alpha, \tilde{\alpha}$ in S^1.

As Equation (3.2.4) is a reaction diffusion equation written as a first order spatial dynamical system, this system is reversible with $\mathcal{R}$ defined by $(u, w) \mapsto (u, -w)$ and equivariant with respect to the temporal shift operator $[\Gamma_\alpha \mathbf{u}](t) := \mathbf{u}(t + \alpha)$. The combination of these symmetries also generates a second reverser for equation (3.4.1). The map $\mathcal{R}\Gamma_\pi = \Gamma_\pi \mathcal{R}$ satisfies the above condition for reversibility. We will see this plays an important role in constructing multiple symmetric defect branches.

Hypothesis 3.4.3 (Background Oscillations)**.** For every $\mu \in J$ there exists a circle of homogeneous oscillations $u_h(t; \alpha)$ for $\alpha \in S^1$, with temporal period ω_0. These homogeneous oscillations satisfy the assumptions of Lemma 3.3.2 so that they have a spatial Floquet spectrum with two zero-eigenvalues followed by $\pm\lambda_1$ and $\pm\lambda_2$ with $0 < \lambda_1(\mu), \lambda_2(\mu)$ uniformly in μ and all other spectrum bounded uniformly outside of this spectrum. The homogeneous oscillations are also accompanied by families of wavetrains $u_h(\phi; k, \omega, c, \mu)$ which have $\omega = \omega_0 + \omega_0'' k^2 + \mathcal{O}(k^4)$.

By equivariance, translation in time Γ_α parameterizes the invariant circle in phase space:

$$u_h(t; \alpha) = u_h(t + \alpha; 0) = [\Gamma_\alpha u_h](t; 0). \tag{3.4.3}$$

Throughout our discussion, we must be careful to keep track of the symmetry implications of this equivariance.

Hypothesis 3.4.4 (Turing Family)**.** For every $\mu \in J$ there exists a family of periodic orbits $u_{Tur}(x; \kappa, \mu)$ smooth in (κ, μ) and $\mathcal{R}-$reversible. The weakest spatial Floquet spectrum of these states consist of two zero Floquet exponents, and two pairs of complex conjugate exponents $\pm\rho(\kappa, \mu) \pm i\beta(\kappa, \mu)$ with real parts bounded uniformly away from zero. All other spectrum is bounded uniformly away from this spectrum. Moreover, we assume the eigenspaces corresponding to the weak stable and unstable exponents only intersect the space of time homogeneous functions trivially at zero.

We get a 1-parameter family due to reversibility as noted in Section 3.3. The final assumption about the eigenspaces is also essential to the following analysis as it allows us to prescribe how the equivariance Γ_α operates on the stable and unstable fibers of the Turing family. Recall from Section 3.3, the Floquet eigenspaces can be identified with the temporal Fourier modes of solutions to the linearized problem. The system is decoupled so our assumption on eigenspaces is that the weakest directions do not correspond time independent functions. We will see that numerical analysis of this decoupled problem for the Brusselator shows that the time-independent functions are not the weakest stable or unstable directions, so we adopt this assumption here.

Importantly for us this has implications on how the equivariance behaves in a neighbourhood of the Turing patterns, even though these patterns themselves are temporally homogeneous. Let the eigenfunction corresponding to the weakest stable Floquet exponent $\nu = -\rho + i\beta$ be given by $(\bar{u}, \bar{w})$ (and its complex conjugate). By our assumption, these functions are not constant and by the set up described above we can express this function as $\zeta_0(x)e^{(-\rho+i\beta)x}e^{2\pi nit}$ for some n where ζ_0 is a spatially periodic function. We can act on this eigenfunction by our equivariance operator Γ_α. Time dependence is captured entirely by the exponential prefactor $e^{2\pi int}$ meaning Γ_α is a rigid rotation of period $2\pi/n$ in the stable subspace. In particular, this means that we can exactly prescribe the action of Γ_α as a 2π-periodic rigid rotation in the weakest stable subspace (and similarly in the weakest unstable subspace). Note that in principle we do not make any assumption on 2π being the minimal period of the rotation, only that it is a period. Without loss of generality, we will assume that the weakest direction is in the $n = 1$ subspace and consequently that the period of Γ_α is 2π.

With these local assumptions on the Turing family we can construct a Fenichel normal form and exchange lemma which will provide the framework for our proof.

Lemma 3.4.5 (Fenichel Normal Form)**.** *Assume Hypotheses 3.4.1, 3.4.2 and 3.4.4. In a neighbourhood of the Turing family $u_{Tur}(\cdot;\cdot,\mu)$, $\mathcal{V}$, there exists a smooth, $\mathcal{R}$-reversible and equivariant change of coordinates, uniform in ω, such that the leading* *order dynamics are given by*

$$
\begin{aligned}
\dot{\varphi} &= \kappa \\
\dot{\kappa} &= c \\
\dot{v}^s &= \begin{pmatrix} -\rho & -\beta \\ \beta & -\rho \end{pmatrix} v^s \\
\dot{v}^{ss} &= A^{ss} v^{ss} \\
\dot{v}^u &= \begin{pmatrix} \rho & \beta \\ -\beta & \rho \end{pmatrix} v^u \\
\dot{v}^{uu} &= A^{uu} v^{uu}
\end{aligned} \tag{3.4.4}
$$

where $\varphi, \kappa \in \mathbb{R}$ are the center coordinates (periodic phase and spatial wavenumber), $v^s, v^u \in \{z \in \mathbb{R}^2 : |z| < \delta\}$ are the weakest stable and unstable directions and $v^{ss}, v^{uu} \in Y$ are the remaining strong stable and unstable directions. Moreover, the reverser is given by

$$\mathcal{R}(\varphi, \kappa, v^s, v^{ss}, v^u, v^{uu}) = (-\varphi, \kappa, v^u, v^{uu}, v^s, v^{ss}) \tag{3.4.5}$$

and the time-shift is given by

$$\Gamma_\alpha(\varphi, \kappa, v^s, v^{ss}, v^u, v^{uu}) = (\varphi, \kappa, R_\alpha v^s, T_\alpha v^{ss}, R_\alpha v^u, T_\alpha v^{uu}). \tag{3.4.6}$$

for all $\alpha \in S^1$ where R_α is the rotation matrix through an angle α in $\mathbb{R}^2$ and T_α is a 2π-periodic operator on the strong stable and unstable directions.

The proof of this statement can be found in Beck et al. (2009), where we note the form of the spatial Floquet exponents described above mean we can enforce the actions of $\mathcal{R}$ and Γ_α described in (3.4.5) and (3.4.6). For $c = 0$ the first two equations are the center-manifold reduction of the Turing family where we see that the Jordan block is expressed as a change in the spatial wavenumber of the oscillations in the family. When $c \neq 0$ we use that the center-manifold is normally hyperbolic to find a new 2-dimensional invariant manifold whose dynamics are a regular perturbation $\mathcal{O}(c)$-close to the original center dynamics. A Melnikov integral computation shows that for c close to zero, the wavenumber κ is adjusted directly by c.

It is important to note that this system is legitimately infinite-dimensional. While we have written these coordinates in a form that exposes the six weakest directions, we cannot ignore the higher order terms. What we will show in the following analysis is that, under subsequent assumptions on the transversality and general position of the incoming manifolds from the homoegeneous oscillations, the infinite-dimensional higher order modes v^{ss} and v^{uu} can be solved for by the Implicit Function Theorem.

In this coordinate system the Turing family itself is the set $\{v^s = v^u = v^{ss} = v^{uu} = 0\}$ with φ the direction of motion around the Turing family and κ the spatial wavenumber. When considering defect solutions that do not transport in the laboratory frame, $\dot{\kappa} = 0$ indicating that there are no dynamics joining Turing patterns of different wavenumber. However, if we move into a co-moving frame with some non-zero constant speed c then the invariant manifold becomes dynamic with a monotone increase or decrease in wavenumber over time. In order to produce symmetric defects it suffices to keep $c = 0$. However, asymmetric defects join fronts and backs associated with Turing patterns of different wavenumber, necessitating a nonzero wavespeed c.

The center-stable and center-unstable manifolds of the Turing family are given by the sets $\{v^u = v^{uu} = 0\}$ and $\{v^s = v^{ss} = 0\}$ respectively. Also the two subspaces

$$\begin{aligned}\Sigma^s &= \{|v^s| = \delta\}\\ \Sigma^u &= \{|v^u| = \delta\}\end{aligned} \tag{3.4.7}$$

form transverse sections to the flow of system (3.4.1) and will be critical in our construction of defect solutions. As a result of Lemma 3.4.5 we can construct a family of solutions joining these two sections which stay close to these center-stable and center-unstable manifolds for large times L.

Lemma 3.4.6 (Exchange Lemma)**.** *Assume Hypotheses 3.4.1, 3.4.2 and 3.4.4. Then for every $\mu \in J$, $c \in C$, $\kappa_0 \in K$, angles $\varphi_0, \theta_0^s, \theta_0^u \in S^1$, $v_0^{ss}, v_0^{uu} \in Y$ and $L > 0$ sufficiently large there is a unique solution $v(x) = v(x; \mu, c, \kappa_0, \varphi_0, \theta_0^s, \theta_0^u, v_0^{ss}, v_0^{uu})$ such that*

$$\begin{aligned}&v(x) \in \mathcal{V} \quad \textit{for all} \quad x \in [-L, L],\\ &v(-L) \in \Sigma^s, \quad \textit{and}\\ &v(L) \in \Sigma^u.\end{aligned} \tag{3.4.8}$$

and with the asymptotics

$$v(-L) = (\varphi_0 - \kappa_0 L + \frac{1}{2}cL^2 + \mathcal{O}, \kappa_0 - cL + \mathcal{O}, \delta\hat{e}(\theta_0^s), v_0^{ss} + \mathcal{O}, \mathcal{O}, \mathcal{O}) \tag{3.4.9}$$

$$v(L) = (\varphi_0 + \kappa_0 L + \frac{1}{2}cL^2 + \mathcal{O}, \kappa_0 + cL + \mathcal{O}, \mathcal{O}, \mathcal{O}, \delta\hat{e}(\theta_0^u), v_0^{uu} + \mathcal{O}) \tag{3.4.10}$$

where $\hat{e}(\alpha)$ is the unit vector in $\mathbb{R}^2$ making angle α with the first component axis and $\mathcal{O} = \mathcal{O}(e^{-\eta L})$ and all such error estimates are smooth and differentiable.

This is a central result stemming from geometric singular perturbation theory (Jones et al., 1996), and extended more generally to any normally hyperbolic sets

(Schecter, 2008a,b). For a proof of this result in the context of spatial dynamics on infinite-cylinders see Beck et al. (2009).

Now we need to make global assumptions on the intersection of the stable and unstable manifolds of the background states with the sections Σ^s and Σ^u. From this we can shoot from the unstable manifold to the stable manifold by way of our exchange lemma and enact a Lin's method matching argument to prove the existence of our defect solutions.

Hypothesis 3.4.7 (Fronts and Invariant Manifolds)**.** For $c = 0$ and $\omega = \omega_0$, there exists a bifurcation family of heteroclinic connections between the homogeneous oscillations $u_h(\cdot;\alpha,\mu)$ and the Turing patterns $u_{Tur}(\cdot;\cdot,\mu)$ as μ is varied through J. By equivariance, for each fixed μ there is an invariant circle of such connections obtainable by the action of Γ_α on any single member of the family.

Moreover, we assume that there is a smooth periodic function $(z,\kappa^*,v^{ss}_*) : S^1 \to J \times K \times Y$, $\varphi \mapsto (z,\kappa^*,v^{ss}_*)(\varphi)$ so that $(\varphi,\kappa,v^{ss},\mu) \in \mathcal{B}$ with

$$\mathcal{B} := \{(\varphi,\kappa,v^{ss},\mu) \ : \ W^{cu}_-(u_h(\cdot;\mu)) \cap W^{cs}_+(u_{Tur}(\cdot;\cdot,\mu)) \cap \Sigma^s \neq \emptyset\} \tag{3.4.11}$$

if, and only if, $\mu = z(\varphi)$, $\kappa = \kappa^*(\varphi)$ and $v^{ss} = T_\alpha v^{ss}_*(\varphi)$ for some $\alpha \in S^1$.

Finally we also assume that the intersection of the incoming manifold $W^{cu}_-(u_h(\cdot;\cdot))$ with the section Σ^s can be parameterized as a graph g over $(\varphi,\theta^s,\kappa,v^{uu},\mu,c,\omega)$. That is, $p \in W^{cu}_-(u_h) \cap \Sigma^s$ nearby the fronts if, and only if,

$$p = (\varphi,\kappa,\delta e^{i\theta^s},g^{ss}(q),g^u(q),v^{uu}) \tag{3.4.12}$$

where $q = (\varphi,\theta^s,\kappa,v^{uu},\mu,c,\omega)$. We assume that the function g and its first derivatives are uniformly bounded in μ.

The function z encodes the bifurcation diagram for the fronts. The fact that it can be written as a periodic function is the feature that determines the snaking of defect solutions. The existence proofs that follow can be weakened to show that the presence of a front necessitates nearby defect solutions. However, the continuation of these solutions and the qualitative features of the snaking diagram require the stronger periodic assumption.

The function $g = (g^u, g^{ss})$ describes the expected behaviour of the incoming and outgoing stable and unstable manifolds. Observe that g^u takes values in $\mathbb{R}^2$ (isomorphic to the unstable manifold of the Turing family) and g^{ss} values in Y (isomorphic to the strong stable fibres of the Turing family). There are many various assumptions one can make here in which the function g and its domain and range have a different graph structure. This particular choice of chart for the manifolds should remain valid for all μ in the bifurcation interval. However, when solving the matching equations it requires a slightly stronger condition on the derivatives of g (see Hypothesis 3.4.8 below) than is necessary. This allows us to use a single setup to globally construct the snaking diagram. It is possible that such a parameterization would fail at some values of μ. For example, the fast stable and unstable directions may become involved in the bifurcation. We should think of this as non-generic behaviour as it would signal the presence of secondary, higher-codimension bifurcations such as inclination flips or resonances in the defect solutions (viewed as homoclinic orbits). We do not consider such cases here. Our assumed parameterization would also fail in the case of a conservative equation as the wavenumber κ would be constant (similarly to the Swift-Hohenberg equation). In such cases, it is possible to amend our current set up using other parameterizations which can be employed separately, or patched together with the one described here, with little change to the overall argument. So we assume that we are in a region where the global parameterization holds.

Hypothesis 3.4.7 does not directly assume any form on the incoming center-stable manifold as we can use Reversibility of the Fenichel normal form to give an explicit representation of this manifold in terms of the incoming center-unstable manifold. From Hypothesis 3.4.7 we know that a point p lies in $\Sigma_- \cap W^{cu}(u_h)$ nearby a front if, and only if, there exist constants $q_- = (\varphi_-, \kappa_-, \theta^s, v_-^{uu})$ such that

$$p = (\varphi_-, \kappa_-, \delta\hat{e}(\theta^s), g^{ss}(q_-, \mu, c, \omega), g^u(q_-, \mu, c, \omega), v_-^{uu}). \tag{3.4.13}$$

When we apply the reverser to this point, we must then have that $\mathcal{R}p$ lies in $\Sigma_+ \cap W^{cs}(u_h)$ as $\mathcal{R}$ maps Σ_- to Σ_+ and the center-unstable manifold to the center-stable (and vice versa). Computing this action we see that

$$\mathcal{R}p = (-\varphi_-, \kappa_-, g^u(q_-, \mu, c, \omega), v_-^{uu}, \delta\hat{e}(\theta^u), g_{ss}(q_-, \mu, c, \omega)). \tag{3.4.14}$$

We can then exactly characterise the opposite intersection as $\bar{p} \in \Sigma_+ \cap W^{cs}(u_h)$ nearby a back if, and only if, there exists constants $q_+ = (\varphi_+, \kappa_+, \theta^u, v_-^{ss})$ such that

$$\bar{p} = (-\varphi_+, \kappa_+, g^u(q_+, \mu, c, \omega), v_+^{ss}, \delta\hat{e}(\theta^u), g^{ss}(q_+, \mu, c, \omega)). \tag{3.4.15}$$

Finally we observe that the location of the fronts and the symmetry operators imply properties of the function g. By assumption the location of fronts are zeros of the component g^u as we require $v^u = 0$ and $v^{uu} = 0$ to lie in the center-stable manifold of the Turing family. Thus, as a consequence of Hypothesis 3.4.7

$$g^u(\Psi, \alpha, \kappa^*(\Psi), 0, z(\Psi), 0, \omega_0) = 0 \tag{3.4.16}$$

for all $\alpha, \Psi \in S^1$. Similarly by acting on the point p in (3.4.12) by the equivariance Γ_α we obtain

$$g^{ss}(\Psi, \alpha, \kappa^*(\Psi), 0, z(\Psi), c, \omega) = T_\alpha v_*^{ss}(\Psi) \tag{3.4.17}$$

for all $\alpha, \Psi \in S^1$. This observation will allow us to find a unique solution for fixed $\theta^s = 0$ and obtain the circle S^1 of its time translations by applying Γ_α.

Finally we need to make non-degeneracy conditions on the bifurcation diagram of the fronts.

Hypothesis 3.4.8 (Non-Degeneracy Condition)**.** The function $\kappa^*(\Psi)$ is bounded away from zero, and the Jacobian matrix $D_{\mu,\kappa} g^u(\Psi, \alpha, \kappa^*(\Psi), 0, z(\Psi), 0, \omega_0)$ is invertible for all $\alpha, \Psi \in S^1$. Also the skeleton function z has the property that its global minima and maxima are unique.

One additional assumption on the skeleton z is required to construct asymmetric defect solutions. Asymmetric defects connect fronts from different locations on the skeleton and so we require that the skeleton z have a property that allows this. We also require one additional invertibility condition to solve the matching equations.

Hypothesis 3.4.9 (Asymmetric Contact Defects)**.** We assume that we can find one parameter families of points $(\varphi_1, \varphi_2) \in S^1 \times S^1$ such that $\varphi_1 \neq \varphi_2 \mod 2\pi$ and $z(\varphi_1) = z(\varphi_2)$. We will assume without loss that these points can be described (locally) by $(\varphi_1, \mathcal{Z}(\varphi_1))$. For the purposes of matching, we will also need to assume that the derivative $D_{\varphi,\kappa} g^u(\Psi, \alpha, \kappa^*(\Psi), 0, z(\Psi), 0, \omega_0)$ is invertible for all $\alpha, \Phi \in S^1$.

Note this hypothesis is effectively a non-degeneracy condition. In the vicinity of local maxima and minima of z one will be able to find such curves. It is this property that leads to the formation of pitchfork bifurcations in snaking systems.

3.5 Proof of Theorem 3.2.1

Our strategy for this proof is to use the periodicity of the skeleton function z to find symmetric defects parameterised by $\varphi \in S^1$ corresponding to their phase coordinate at the midpoint in the neighbourhood $\mathcal{V}$. The major drawback of this approach is that we do not directly show that a contact defect exists for each value of μ. Instead this is implicit in our result through our parameterization of the bifurcation diagram $z(\varphi)$. For any value of $\mu = z(\varphi)$ with a front, we use the construction below to find nearby defect solutions for $\mu = z(\varphi) + \bar{\mu}$ where $\bar{\mu}$ is shown to be exponentially small. Then, so long as we are away from the saddle-nodes of the fronts, and using the assumption that $D_{\mu,\kappa} g^u$ is invertible, we can use the Implicit Function Theorem to write the bifurcation curve as a graph over μ close to $z(\varphi)$. By uniqueness of these solutions, we can patch these graphs for different values of φ together to reassemble the symmetric branches of the diagram as functions of μ.

The advantage of this method is that we naturally obtain the leading order periodic structure of the snaking diagram from the skeleton function $z(\varphi)$, including near its global extrema.

Proof. Our objective is to find an exchange solution $v(x)$ through the neighbourhood $\mathcal{V}$ that connects the center-unstable and center-stable manifolds of the background states which is also $\mathcal{R}$-symmetric. Using this symmetry condition, it suffices for us to solve the following problem: find an exchange solution $v(x)$ such that

$$\begin{aligned} & v(x) \in \mathcal{V} \text{ for all } x \in [-L, L], \\ & v(-L) \in W^{cu}(u_h(\cdot;\cdot)) \cap \Sigma^s, \\ & v(0) \in \mathrm{Fix}\mathcal{R}. \end{aligned} \tag{3.5.1}$$

From Lemma 3.4.5 we know the action of the reverser $\mathcal{R}$ on our Fenichel coordinates and have exact criteria for when the exchange solution $v(x) = v(x; \mu, \kappa_0, \varphi_0, \theta_0^s, \theta_0^u, v_0^{ss}, v_0^{uu})$ is $\mathcal{R}$-symmetric. This is the case if, and only if, $\varphi_0 \in \{0, \pi\}$, $\theta_0^s = \theta_0^u \pmod{2\pi}$, $v_0^{ss} = v_0^{uu}$ and $c = 0$. So for the remainder of this section we restrict to those exchange solutions $v(x; \mu, 0, \kappa_0, \varphi_0, \theta_0, \theta_0, v_0, v_0)$ where $\varphi_0 \in \{0, 2\pi\}$. Since c is forced to be zero, $\omega = \omega_0$ and we ignore the dependence on these parameters from now on.

This reduces the problem to solving the matching condition $v(-L) \in W^{cu}(u_h(\cdot;\cdot)) \cap \Sigma^s$. Lemma 3.4.6 shows that $v(-L)$ can be written as

$$\begin{aligned} & v(-L; \mu, \kappa_0, \varphi_0, \theta_0, \theta_0, v_0, v_0) \\ & = (\varphi_0 - \kappa_0 L + \mathcal{O}(e^{-\eta L}), \kappa_0 + \mathcal{O}(e^{-\eta L}), \delta \hat{e}(\theta_0), v_0 + \mathcal{O}(e^{-\eta L}), \mathcal{O}(e^{-\eta L}), \mathcal{O}(e^{-\eta L})). \end{aligned}$$

Hypothesis 3.4.7 implies that elements of manifold $W^{cu}(u_h(\cdot;\cdot)) \cap \Sigma^s$ are of the form $(\varphi, \kappa, \delta e^{i\theta^s}, g^{ss}(q), g^u(q), v^{uu})$ for $q = (\varphi, \theta^s, \kappa, v^{uu}, \mu)$. Thus, solving the matching condition $v(-L) \in W^{cu}(u_h(\cdot;\cdot)) \cap \Sigma^s$ is equivalent to constructing solutions $(L, \varphi, \theta^s, \kappa, v^{uu}, \mu, \kappa_0, \theta_0, v_0)$ of the system

$$\begin{aligned} & (\varphi_0 - \kappa_0 L + \mathcal{O}(e^{-\eta L}), \kappa_0 + \mathcal{O}(e^{-\eta L}), \delta \hat{e}(\theta_0), v_0 + \mathcal{O}(e^{-\eta L}), \mathcal{O}(e^{-\eta L}), \mathcal{O}(e^{-\eta L})) \\ & \qquad = (\varphi, \kappa, \delta \hat{e}(\theta^s), g^{ss}(q), g^u(q), v^{uu}). \end{aligned} \tag{3.5.2}$$

Since the existence statement should be true for all L sufficiently large, we will look for solutions in the limit as L grows to infinity.

We immediately conclude that $\theta^s = \theta_0 =: \alpha$ is a free parameter unfolding the S^1-equivariant symmetry of our solutions. By fixing α we factor out this symmetry so that we are looking for unique solutions. We can also solve for v^{uu} using the Implicit Function Theorem in the limit as $L \to \infty$ and find that $v^{uu} = \mathcal{O}(e^{-\eta L})$. The remaining equations are:

$$\varphi = \varphi_0 - \kappa_0 L + \mathcal{O}(e^{-\eta L}) \qquad \text{mod } 2\pi, \tag{3.5.3}$$

$$\kappa = \kappa_0 + \mathcal{O}(e^{-\eta L}), \tag{3.5.4}$$

$$g^{ss}(\varphi, \alpha, \kappa, \mathcal{O}(e^{-\eta L}), \mu) = v_0 + \mathcal{O}(e^{-\eta L}), \tag{3.5.5}$$

$$g^{u}(\varphi, \alpha, \kappa, \mathcal{O}(e^{-\eta L}), \mu) = \mathcal{O}(e^{-\eta L}), \tag{3.5.6}$$

for the unknowns $(\varphi, \kappa, \kappa_0, \mu, L, v_0)$. We are looking for a 1-parameter family of solutions for each $\alpha \in S^1$ (we have factored out the equivariance), so this dimension count makes sense. We also have a choice of which variable to use to parameterise the family. The intuitive choice is L as this is our proxy for the width of the core region, however it will prove to be easier if we instead use φ. With this in mind we relabel our unknowns to make use of Hypothesis 3.4.8 and express everything as functions of φ. Let $\mu = z(\varphi) + \bar{\mu}$, $\kappa = \kappa^*(\varphi) + \bar{\kappa}$, $\kappa_0 = \kappa^*(\varphi) + \bar{\kappa}_0$ and $v_0 = T_\alpha v_*^{ss}(\varphi) + \bar{v}$ so that,

$$\varphi = \varphi_0 - (\kappa^*(\varphi) + \bar{\kappa})L + \mathcal{O}(e^{-\eta L}) \qquad \text{mod } 2\pi, \tag{3.5.7}$$

$$\bar{\kappa} = \bar{\kappa}_0 + \mathcal{O}(e^{-\eta L}), \tag{3.5.8}$$

$$g^{ss}(\varphi, \alpha, \kappa^*(\varphi) + \bar{\kappa}, \mathcal{O}(e^{-\eta L}), z(\varphi) + \bar{\mu}) = T_\alpha v_*^{ss}(\varphi) + \bar{v} + \mathcal{O}(e^{-\eta L}), \tag{3.5.9}$$

$$g^{u}(\varphi, \alpha, \kappa^*(\varphi) + \bar{\kappa}, \mathcal{O}(e^{-\eta L}), z(\varphi) + \bar{\mu}) = \mathcal{O}(e^{-\eta L}). \tag{3.5.10}$$

Recall equations (3.4.16) and (3.4.17),

$$g^u(\Psi, \alpha, \kappa^*(\Psi), 0, z(\Psi), 0, \omega_0) = 0,$$
$$g^{ss}(\Psi, \alpha, \kappa^*(\Psi), 0, z(\Psi), 0, \omega_0) = T_\alpha v_*^{ss}(\Psi),$$

providing us known values of g^u and g^{ss} about which we can expand to find

$$\varphi = \varphi_0 - (\kappa^*(\varphi) + \bar{\kappa})L + \mathcal{O}(e^{-\eta L}) \qquad \text{mod } 2\pi \tag{3.5.11}$$

$$\bar{\kappa} - \bar{\kappa}_0 = \mathcal{O}(e^{-\eta L}) \tag{3.5.12}$$

$$\bar{v} + D_{\mu,\kappa} g^{ss}(\varphi, \alpha, \kappa^*(\varphi), 0, z(\varphi)) \begin{pmatrix} \bar{\mu} \\ \bar{\kappa} \end{pmatrix} = R_1(\bar{\mu}, \bar{\kappa}) + \mathcal{O}(e^{-\eta L}) \tag{3.5.13}$$

$$D_{\mu,\kappa} g^u(\varphi, \alpha, \kappa^*(\varphi), 0, z(\varphi)) \begin{pmatrix} \bar{\mu} \\ \bar{\kappa} \end{pmatrix} = R_2(\bar{\mu}, \bar{\kappa}) + \mathcal{O}(e^{-\eta L}) \tag{3.5.14}$$

where R_1 and R_2 are quadratic in $(\bar{\mu}, \bar{\kappa})$ by Taylor's theorem. We have assumed that the derivatives of g are uniformly bounded meaning the other first derivative terms contribute at most $\mathcal{O}(e^{-\eta L})$ and can be absorbed into the higher order terms. We are now looking for a solution $(L, \bar{\kappa}, \bar{\kappa}_0, \bar{v}, \bar{\mu})$ as functions of φ.

Hypothesis 3.4.8 implies that $D_{\mu,\kappa} g^u : \mathbb{R}^2 \to \mathbb{R}^2$ is invertible (recall that the weak unstable subspace is two-dimensional so g^u takes values in $\mathbb{R}^2$). From this we conclude that the linear operator of $(\bar{\mu}, \bar{\kappa}, \bar{\kappa}_0, \bar{v})$ on the left-hand side of the final three equations in (3.5.11) is invertible, and we use the Implicit Function Theorem to solve uniquely for $(\bar{\mu}, \bar{\kappa}, \bar{\kappa}_0, \bar{v})$. Moreover, we have the estimates $(\bar{\mu}, \bar{\kappa}, \bar{\kappa}_0, \bar{v}) = \mathcal{O}(e^{-\eta L})$. All that remains is to solve the first equation, which, upon substituting $\bar{\kappa} = \mathcal{O}(e^{-\eta L})$, is given by

$$\varphi = \varphi_0 - \kappa^*(\varphi)L + \mathcal{O}(e^{-\eta L}) \qquad \text{mod } 2\pi. \tag{3.5.15}$$

Since this is an equation posed on $\mathbb{R}/2\pi\mathbb{Z}$, we write $L = (2\pi n + l)/\kappa^*(\varphi)$ for $n \in \mathbb{Z}$ and $l \in S^1$ where we note that we assumed in Hypothesis 3.4.8 that $\kappa^*(\varphi) \neq 0$. The resulting equation for l is given by

$$\varphi = \varphi_0 - l + \mathcal{O}(e^{-\bar{\eta} n}), \tag{3.5.16}$$

which we can solve for $l = \varphi_0 - \varphi + \mathcal{O}(e^{-\bar{\eta} n})$ as a function of φ and n (recall that $\varphi_0 \in \{0, \pi\}$ is fixed) so that

$$L = \frac{\varphi_0 - \varphi + 2\pi n}{\kappa^*(\varphi)} + \mathcal{O}(e^{-\bar{\eta} n}) \tag{3.5.17}$$

for each $n \in \mathbb{Z}$ large enough. That is, for each front in the bifurcation diagram $\mathcal{B}$ there exist a countably infinite number of defect solutions nearby, indexed by a natural number n, and which spend an increasing amount of time near the Turing family. This proves Theorem 3.2.1.

□

In this proof we reduced the problem to a single matching condition using criteria for $\mathcal{R}$-symmetric solutions in $\mathcal{V}$. We can equally determine such a reduction for $\Gamma_\pi\mathcal{R}$-symmetric solutions. Indeed, an exchange solution v is $\Gamma_\pi\mathcal{R}$-symmetric if, and only if, $\varphi_0 \in \{0, \pi\}$, $\theta_0^s - \theta_0^u = \pi \mod 2\pi$, $v_0^{ss} = T_\pi v_0^{uu}$ and $c = 0$, using the Exchange Lemma asymptotics. Once this identification is made, the remainder of the proof continues in exactly the same way and we find that we have branches of both target and spiral defects as claimed in Section 3.2.

3.6 Proof of Theorem 3.2.2

This proof follows in much the same way as the previous, except that we cannot use symmetry to reduce the matching equations. As a consequence, there are additional degrees of freedom that we need to take account of.

Most importantly, we will need to consider the equations in a comoving frame with a non-zero wavespeed c. As discussed in Section 3.3, we need to be careful in our construction that we end up with contact defects at the end. Recall from Lemma 3.3.3, for all c small enough we can find wavetrains with spatial wavenumber $k = k(c)$ and temporal frequency $\omega = \omega(c)$ which have group velocity c. By setting $\omega = \omega(c)$ we ensure that any defect we find will be a contact defect and we drop the dependence of our manifolds on ω.

We will also find solutions that are parameterised both by a phase φ and a phase offset $\theta^u - \theta^s$. The phase φ will trace out the winding of the snaking diagram as it did in the symmetric case. On the other hand $\theta^u - \theta^s$ will parameterise the circular cross-sections of the tubular neighbourhoods. Note this is distinct from the symmetric case where $\theta^s = \alpha$ parameterized the S^1-equivariance of our solutions for fixed μ. In this case we can again set $\theta^s = \alpha$, which parameterizes this equivariance, but we can also still vary θ^u to make all possible background phase offsets.

Proof. Again we wish to find an exchange solution $v(x)$ through $\mathcal{V}$ that connects the center-unstable and center stable manifolds of the background states. However, this time we cannot simplify the system using reversibility. Instead, we are looking for a solution $(L, c, \varphi, \varphi_-, \varphi_+, \kappa, \kappa_-, \kappa_+, \theta^s, \theta_0^s, \theta^u, \theta_0^u, v_0^{ss}, v_+^{ss}, v_0^{uu}, v_-^{uu})$ to the two matching conditions

$$(\varphi, \kappa, \delta\hat{e}(\theta_0^s), v_0^{ss}, \mathcal{O}(e^{-\eta L}), \mathcal{O}(e^{-\eta L})) = (\varphi_-, \kappa_-, \delta\hat{e}(i\theta^s), g^{ss}(q_-), g^u(q_-), v_-^{uu}), \tag{3.6.1}$$

$$\begin{aligned}(\varphi + 2\kappa L + 2cL^2 + \mathcal{O}(e^{-\eta L}), \kappa + 2cL + \mathcal{O}(e^{-\eta L}), \mathcal{O}(e^{-\eta L}), \mathcal{O}(e^{-\eta L}), \delta\hat{e}(\theta_0^u), v_0^{uu})\\ = (-\varphi_+, \kappa_+, g^u(q_+), v_+^{ss}, \delta\hat{e}(\theta^u), g^{ss}(q_+))\end{aligned} \tag{3.6.2}$$

where $q_- = (\varphi_-, \theta^s, \kappa_-, v_-^{uu}, \mu, c)$ and $q_+ = (\varphi_+, \theta^u, \kappa_+, v_+^{ss}, \mu, c)$.

We immediately have that $\varphi = \varphi_-$, $\kappa = \kappa_-$, $\theta_0^s = \theta^s$, $\theta_0^u = \theta^u$ and we can use the Implicit Function Theorem to solve for $v_-^{uu} = \mathcal{O}(e^{-\eta L})$ and $v_+^{ss} = \mathcal{O}(e^{-\eta L})$. The remaining equations are then

$$-\varphi_+ = \varphi_- + 2cL^2 + 2\kappa_- L + \mathcal{O}(e^{-\eta L}) \qquad \text{mod } 2\pi, \tag{3.6.3}$$

$$\kappa_+ = \kappa_- + 2cL + \mathcal{O}(e^{-\eta L}), \tag{3.6.4}$$

$$g^u(\varphi_-, \theta^s, \kappa_-, \mathcal{O}(e^{-\eta L}), \mu, c) = \mathcal{O}(e^{-\eta L}), \tag{3.6.5}$$

$$g^u(\varphi_+, \theta^u, \kappa_+, \mathcal{O}(e^{-\eta L}), \mu, c) = \mathcal{O}(e^{-\eta L}), \tag{3.6.6}$$

$$g^{ss}(\varphi_-, \theta^s, \kappa_-, \mathcal{O}(e^{-\eta L}), \mu, c) = v_0^{ss}, \tag{3.6.7}$$

$$g^{ss}(\varphi_+, \theta^u, \kappa_+, \mathcal{O}(e^{-\eta L}), \mu, c) = v_0^{uu}. \tag{3.6.8}$$

Excluding the final two equations which are infinite dimensional, we have a 6-dimensional set of equations in the seven unknowns $\varphi_\pm$, $\kappa_\pm$, c, L and μ, meaning we will have to solve for at least one of $\varphi_\pm$. We use Hypothesis 3.4.9 and let $\varphi_+ = \mathcal{Z}(\varphi_-) + \bar{\varphi}_+$, and solve for $\bar{\varphi}_+$. Suppose we choose φ_- away from the global maxima and minima of z. Then like the symmetric case we look to show the resulting solutions are formed at an exponentially small perturbation of the periodic skeleton determined by φ_- and $\mathcal{Z}(\varphi_-)$. Let $\kappa_- = \kappa^*(\varphi_-) + \bar{\kappa}_-$, $\kappa_+ = \kappa^*(\mathcal{Z}(\varphi_-)) + \bar{\kappa}_+$, $\mu = z(\varphi_-) + \bar{\mu} = z(\mathcal{Z}(\varphi_-)) + \bar{\mu}$, $v_0^{ss} = T_{\theta^s}(v_*^{ss}(\varphi_-) + \bar{v}_0^{ss})$ and $v_0^{uu} = T_{\theta^u}(v_*^{ss}(\mathcal{Z}(\varphi_-)) + \bar{v}_0^{uu})$. Substituting these we get

$$-\mathcal{Z}(\varphi_-) - \bar{\varphi}_+ = \varphi_- + 2cL^2 + 2(\kappa^*(\varphi_-) + \bar{\kappa}_-)L \ + \mathcal{O}(e^{-\eta L}) \quad \mod 2\pi \tag{3.6.9}$$

$$\kappa^*(\mathcal{Z}(\varphi_-)) + \bar{\kappa}_+ = \kappa^*(\varphi_-) + \bar{\kappa}_- + 2cL \ + \mathcal{O}(e^{-\eta L}) \tag{3.6.10}$$

$$g^u(\varphi_-, \theta^s, \kappa^*(\varphi_-) + \bar{\kappa}_-, \mathcal{O}(e^{-\eta L}), z(\varphi_-) + \bar{\mu}, c) = \mathcal{O}(e^{-\eta L}) \tag{3.6.11}$$

$$\begin{aligned} g^u(\mathcal{Z}(\varphi_-) + \bar{\varphi}_+, \theta^u, \kappa^*(\mathcal{Z}(\varphi_-)) + \bar{\kappa}_+, \mathcal{O}(e^{-\eta L}), z(\mathcal{Z}(\varphi_-)) + \bar{\mu}, c) \\ = \mathcal{O}(e^{-\eta L}) \end{aligned} \tag{3.6.12}$$

$$\begin{aligned} g^{ss}(\varphi_-, \theta^s, \kappa^*(\varphi_-) + \bar{\kappa}_-, \mathcal{O}(e^{-\eta L}), z(\varphi_-) + \bar{\mu}, c) \\ = T_{\theta^s}(v_*^{ss}(\varphi_-) + \bar{v}_0^{ss}) \end{aligned} \tag{3.6.13}$$

$$\begin{aligned} g^{ss}(\mathcal{Z}(\varphi_-) + \bar{\varphi}_+, \theta^u, \kappa^*(\mathcal{Z}(\varphi_-)) + \bar{\kappa}_+, \mathcal{O}(e^{-\eta L}), z(\varphi_+ \mathcal{Z}(\varphi_-)) + \bar{\mu}, c) \\ = T_{\theta^u}(v_*^{ss}(\mathcal{Z}(\varphi_-)) + \bar{v}_0^{uu}) \end{aligned} \tag{3.6.14}$$

We start by solving the second, third and fourth equations. By expanding the third equation about $q_- = (\varphi_-, \theta^s, \kappa^*(\varphi_-), 0, z(\varphi_-), 0)$ and the fourth equation about $q_+ = (\mathcal{Z}(\varphi_-), \theta^u, \kappa^*(\mathcal{Z}(\varphi_-)), 0, z(\mathcal{Z}(\varphi_-)), 0)$ and rearranging to put the leading order linear operators on the left-hand side, these equations become

$$D_{\varphi,\kappa}g^u(q_+)\begin{pmatrix}\bar{\varphi}_+\\ \bar{\kappa}_+\end{pmatrix}+\frac{\partial g^u}{\partial\mu}(q_+)\bar{\mu}+\frac{\partial g^u}{\partial c}(q_+)c+R_2(\bar{\varphi}_+,\bar{\kappa}_+,\bar{\mu},c)+\mathcal{O}(e^{-\eta L})=0 \tag{3.6.15}$$

$$D_{\kappa,\mu}g^u(q_-)\begin{pmatrix}\bar{\kappa}_-\\ \bar{\mu}\end{pmatrix}+\frac{\partial g^u}{\partial c}(q_-)c+R_1(\bar{\kappa}_-,\bar{\mu},c)+\mathcal{O}(e^{-\eta L})=0 \tag{3.6.16}$$

$$\bar{\kappa}_+-\bar{\kappa}_--2Lc+\mathcal{O}(e^{-\eta L})=\kappa^*(\varphi_-)-\kappa^*(\mathcal{Z}(\varphi_-)) \tag{3.6.17}$$

where the φ,κ and μ subscripts denote partial derivatives, and the functions R_1 and R_2 are quadratic in their arguments by Taylor's theorem. Again we use that the derivatives of g^u are uniformly bounded in Hypothesis 3.4.8 to subsume other derivative terms into the order $\mathcal{O}(e^{-\eta L})$ terms. Our goal is to solve these equations for the unknowns $(\bar{\varphi}_+,\bar{\kappa}_+,\bar{\kappa}_-,\bar{\mu},c)$ by the Implicit Function Theorem which requires that the leading order linear operator on the left-hand side be invertible. We can write this operator as

$$\left[\begin{array}{cc|c} D_{\varphi,\kappa}g^u(q_+) & \begin{matrix}0\\0\end{matrix}\ \ \frac{\partial g^u}{\partial\mu}(q_+) & \frac{\partial g^u}{\partial c}(q_+)\\ \mathbf{0} & D_{\kappa,\mu}g^u(q_-) & \frac{\partial g^u}{\partial c}(q_-)\\ \hline 0\quad 1 & -1\quad 0 & -2L\end{array}\right]=:\left[\begin{array}{cccc|c} & & A & & b\\ \hline 0 & 1 & -1 & 0 & -2L\end{array}\right]. \tag{3.6.18}$$

The main 4×4 block, A, is invertible by Hypotheses 3.4.8 and 3.4.9 where we assume that its diagonal blocks are invertible. To show the full matrix is invertible, we show that it has a trivial kernel for all L sufficiently large. Suppose $(\bar{\varphi}_+,\bar{\kappa}_+,\bar{\kappa}_-,\bar{\mu},c)$ is in the kernel of the operator, then by matrix multiplication and using the invertibility of A we find

$$\begin{bmatrix} \bar{\varphi}_+ \\ \bar{\kappa}_+ \\ \bar{\kappa}_- \\ \bar{\mu} \end{bmatrix} = -cA^{-1}b, \quad \bar{\kappa}_+ - \bar{\kappa}_- - 2Lc = 0. \tag{3.6.19}$$

Using the first equation we can eliminate $\bar{\kappa}_\pm$ from the second equation which yields

$$c(\langle A_3^{-1} - A_2^{-1}, b\rangle - 2L) = 0 \tag{3.6.20}$$

where A_j^{-1} is the j-th row of the matrix A^{-1} and $\langle , \rangle$ is the vector dot product. Since, A and b are made up of derivatives of g^u which we are uniformly bounded, for all sufficiently large L the only solution to this equation is $c = 0$. This implies the vector $(\bar{\varphi}_+, \bar{\kappa}_+, \bar{\kappa}_-, \bar{\mu}, c)$ is exactly zero.

Applying the Implicit Function Theorem, we can find unique solutions $(\bar{\varphi}_+, \bar{\kappa}_+, \bar{\kappa}_-, \bar{\mu}, c)$ to equations (3.6.15)-(3.6.17) which have expansions

$$c = \frac{\Delta\kappa}{2L} + \mathcal{O}(e^{-\eta L}), \tag{3.6.21}$$

$$(\bar{\varphi}_+, \bar{\kappa}_+, \bar{\kappa}_-, \bar{\mu}) = \mathcal{O}\left(\frac{\Delta\kappa}{L} + e^{-\eta L}\right), \tag{3.6.22}$$

where $\Delta\kappa := \kappa^*(\mathcal{Z}(\varphi_-)) - \kappa^*(\varphi_-)$ is the difference between the selected wavenumbers. Using these expansions we can solve equations (3.6.13) and (3.6.14) and again find that $\bar{v}_0^{ss}, \bar{v}_0^{uu} = \mathcal{O}(\Delta\kappa/L + e^{-\eta L})$.

All that remains is to solve the equation (3.6.9) for L. Using our new asymptotics for $\bar{\kappa}_+$ and $\bar{\kappa}_-$ this equation reduces to

$$-\mathcal{Z}(\varphi_-) = \varphi_- + B\Delta\kappa + L(\kappa^*(\mathcal{Z}(\varphi_-)) + \kappa^*(\varphi_-)) + \mathcal{O}\left(\frac{\Delta\kappa}{L} + e^{-\eta L}\right) \mod 2\pi \tag{3.6.23}$$

for some uniformly bounded constant B. Let $L = (l + 2\pi n)/(\kappa^*(\mathcal{Z}(\varphi_-)) + \kappa^*(\varphi_-))$ for $n \in \mathbb{Z}$ large and $l \in S^1$, then by the Implicit Function Theorem we conclude

$$L = \frac{-(\mathcal{Z}(\varphi_-) + \varphi_-) + 2\pi n}{\kappa^*(\mathcal{Z}(\varphi_-)) + \kappa^*(\varphi_-)} + \mathcal{O}\left(\frac{\Delta\kappa}{n} + e^{-\eta n}\right) \tag{3.6.24}$$

completing the proof.

$\square$

This proof only depends on the choice front and back selected assuming we can find valid choices for $\varphi_\pm$. We can exactly recover our result for symmetric contact defects by choosing $\varphi_- = \varphi_+$ for which $\Delta\kappa = 0$, which reproduces both snaking curves corresponding to $\varphi_0 = 0, \pi$. Along with our symmetric contact defects, for each value of $\mu \in J$ we get an S^1 of contact defects with a phase offset $\alpha \in S^1$ in their background oscillations which move at very small wavespeeds of the order $\mathcal{O}(e^{-\eta L})$.

There are also fully asymmetric solutions formed by taking distinct values φ_- and φ_+ which select different wavenumbers. In this case, the defects move at larger speeds $c \approx \Delta\kappa/2L$. They also have asymmetric core regions which have core Turing regions shifted in x and modulated in spatial wavenumber κ. These branches also differ from the regular snaking situation, as they will not lie exponentially close to the position predicted by the skeleton z. Instead, they are a larger $\Delta\kappa/L$ perturbation, which is small for sufficiently large L and for μ close to the symmetric branch saddle-nodes.

3.7 Numerical Computation in the Brusselator

Our motivating example is the two component reaction diffusion system

$$U_t = DU_{xx} + E - (B+1)U + VU^2 \tag{3.7.1}$$

$$V_t = V_{xx} + BU - VU^2 \tag{3.7.2}$$

called the Brusselator. Numerical studies in Tzou et al. (2013) appear to show snaking of symmetric contact defect solutions for parameter values $E = 1.4, B = 3.21$ and D in a small neighbourhood of 0.266. Here we attempt to replicate their numerics for symmetric solutions. In order to find the asymmetric solutions we will need to use a significantly more complex approximation scheme which gives us direct control over the phase offset, temporal frequency and spatial wavenumbers of the various oscillations. The method we chose to accomplish this was the core far-field decomposition developed in Morrissey and Scheel (2015) and Lloyd and Scheel (2017) and already discussed in a simpler setting in Chapter 2. In the next section we propose how one might use this method to find fronts in the Brusselator.

3.7.1 Core-Far Field Decomposition for Fronts

For the moment we ignore the issue of boundary conditions and instead think of (3.7.2) as a general reaction diffusion equation of the form (3.2.3) for $x \in \mathbb{R}$ which is periodic in time. We are interested in solutions which are asymptotic to predetermined background oscillations which we denote by $u_-(x,t)$ and $u_+(x,t)$. We seek to enforce this condition directly by making the ansatz $u(x,t) = \chi_-(x)u_-(x,t) + \chi_+(x)u_+(x,t) + w(x,t)$. Here χ_+ (χ_-) is a smooth cut-off function which is 0 at zero and 1 for x large and positive (resp. x large and negative). Applying this ansatz, we wish to find w solving the equation:

$$w_t = Dw_{xx} - [(\chi_- u_- + \chi_+ u_+)_t - D(\chi_- u_- + \chi_+ u_+)_{xx}] + f(\chi_- u_- \chi_+ u_+ + w) \tag{3.7.3}$$

$$\begin{aligned} &= Dw_{xx} - [(\chi_- u_- + \chi_+ u_+)_t - D(\chi_- u_- + \chi_+ u_+)_{xx} - f(\chi_- u_- + \chi_+ u_+)] \qquad (3.7.4) \\ &\quad + [f(\chi_- u_- \chi_+ u_+ + w) - f(\chi_- u_- + \chi_+ u_+)] \, . \end{aligned}$$

Observe that if we put a localised w into this equations, the corresponding residue will also be localised, as for large x (positive or negative) the second two terms on the right hand side vanish. So, assuming we know the background oscillations, we are now interested in determining the interface function $w(x,t)$ which should be localised in the correct sense and periodic in time. There are two problems to overcome in implementing this ansatz as a numerical tool: 1) while we know that equations $u_\pm$ satisfy we do not know their frequencies (spatial or temporal) beforehand; and, 2) we need to be able to enforce that the solution for w that we find remains localised.

For the remainder of this section we will use the convention that u_- is the spatially homogeneous background oscillation and u_+ is the temporally homogeneous Turing pattern. In finding the interface $w(x,t)$ between these solutions, we are finding the heteroclinic front solution. Note that u_- is a solution to the equation

$$\omega \; u_t = f(u)$$

$$u(0) = u(2\pi)$$

where we should expect only a single possible temporal frequency ω to be selected for any particular value of the bifurcation parameter μ. For the purposes of solving for this temporal frequency, we add an auxiliary phase condition that eliminates the translational symmetry of the equation:

$$\int_0^1 \phi'(\xi)(u(\xi) - \phi(\xi))\mathrm{d}\xi = 0,$$

where ϕ is an appropriately chosen function.

The Turing pattern can be found as a solution to the equation

$$0 = \kappa^2 D u_{xx} + f(u) \tag{3.7.5}$$

$$u_x(0) = u_x(2\pi) = 0 \tag{3.7.6}$$

where κ is the spatial wavenumber of the Turing pattern and we use Neumann boundary conditions to remove translational symmetry. In this case we cannot select the correct value of κ with a simple phase condition due to the presence of the Turing family. As noted above, in reversible systems periodic orbits appear in one parameter families and there is an interval of values for κ which admit Turing patterns u_+. The front solution itself then selects the correct value of κ, and we must solve for κ as part of our scheme.

So we need to determine a good choice of boundary and integral phase-type conditions which will allow the selection of the correct background oscillations. On the real line these boundary conditions correspond to convergence estimates on the tails of $w(x,t)$ by having finite norm in the correctly weighted space.

For large positive x we want to enforce exponential converge to a Turing pattern.

From the theory presented above, we know that our fronts will converge through the strong stable fibres of the Turing family to a single Turing pattern with wavenumber κ. We enforce this by considering an exponentially weighted L^2-norm. Let η be a small, positive rate and define the norm,

$$||u||_\eta = \left(\int_0^\infty e^{\eta x} |u(x)|^2 \mathrm{d}x \right)^{1/2}. \tag{3.7.7}$$

This norm penalises functions that do not converge faster than the exponential function $e^{-\eta x}$ and so excludes the possibility of $w(x,t)$ converging through the centre-directions of the Turing pattern. That is, it excludes convergence to the incorrect phase offset Turing pattern and a Turing pattern of an incorrect wavenumber κ. However, this does not remove the requirement that we can determine the correct Turing wavenumber κ. For this we need an integral phase condition.

We do this by constructing a bounded solution to the adjoint variational equation to (3.7.5), ψ^+. Note that (3.7.5) written as a spatial dynamical system is

$$u_x = v \tag{3.7.8}$$

$$v_x = -D^{-1} f(u) \tag{3.7.9}$$

where we suppress the explicit κ dependence by rescaling the spatial variable x. The adjoint variational equation is then

$$\psi' = \begin{pmatrix} 0 & D^{-1} f_u(u_+) \\ -1 & 0 \end{pmatrix} \psi$$

where we have linearized about the Turing pattern u_+ with wavenumber κ. This bounded solution corresponds a function which is orthogonal to the Floquet exponent 0 eigenfunction $\partial_x u_+$ of the Turing pattern. Our phase condition then specifies that the dynamic motion of w, specified by (3.7.4) in the positive far-field should be orthogonal to ψ. Since ψ is orthogonal to $\partial_x u_+$, the dot-product $\psi \cdot (w, w_x)$ will be positive if it has a component in the centre-direction corresponding to modulation in the Turing wavelength, which is exactly the behavior we want to exclude. That is, we enforce that

$$\int_0^1 \int_M^\infty \begin{pmatrix} w \\ w_x \end{pmatrix} \cdot \psi(\xi) \mathrm{d}\xi \mathrm{d}t = 0$$

where we integrate over the large values of x and one temporal wavelength for numerical accuracy.

A relative Morse index calculation, similar to that described in Lemma 3.3.2, shows that the linearization of the Turing equation (3.7.5) has Fredholm index -1 when posed as an operator on L^2_η. The addition of the unknown κ and the wavenumber phase condition then change the Fredholm index to zero.

For large negative x, we converge to the family of homogeneous oscillations. Recall from Section 3.3 this convergence is necessarily through the centre-unstable manifold of these oscillations. As such we cannot require exponential localisation, as we have algebraic decay at best. It turns out that this is not an obstruction for us, as one can use the fact that the center-manifold reduction about the homogeneous oscillations reveals a radial Laplacian structure whose linearization is Fredholm of index zero when posed on spaces that allow algebraic decay, for example Krondratiev spaces (Jaramillo and Scheel, 2015).

On bounded large domains, we can no longer enforce localisation through the use of norms, as all norms are equivalent. So instead we need to replace the finite-norm conditions by boundary conditions that enforce the correct localisation. On the right hand boundary, we have already excluded the possibility of modulation in wavenumber κ with our phase condition. So we need to exclude the possibility of the interface $w(x,t)$ being translated against the Turing pattern u_+. We do this by applying Neumann boundary conditions in x to both $w(x,t)$ and $u_+(x)$. On the left hand boundary, we need to exclude convergence to the incorrect phase offset of the homogeneous oscillation. As alluded above, the centre-manifold reduction about the homogeneous oscillations looks like radial Laplacian, which contains solutions with asymptotics $w \sim 1$ and $w \sim 1/x$. The order one functions correspond to phase shifts in the background oscillations, while the order $1/x$ functions capture the convergence we are looking for. We exclude the order one functions by applying Dirichlet boundary conditions.

To summarise we are looking for solutions $(w(x,t), \kappa)$ to the system of equations:

$$\begin{aligned} w_t = D w_{xx} - [(\chi_- u_- + \chi_+ u_+)_t - D(\chi_- u_- + \chi_+ u_+)_{xx}] \\ + f(\chi_- u_- \chi_+ u_+ + w), \end{aligned} \tag{3.7.10}$$

$$w(x,0) = w(x,1) \quad \forall x \in [-L, L], \tag{3.7.11}$$

$$\partial_x w(-L,t) = \partial_x w(L,t) = 0 \quad \forall t \in [0, 2\pi], \tag{3.7.12}$$

$$\int_0^{2\pi} \int_M^L \begin{pmatrix} w \\ w_x \end{pmatrix} \cdot \psi(\xi) \mathrm{d}\xi \mathrm{d}t = 0; \tag{3.7.13}$$

where $(u_-, u_+, \psi_+, \varepsilon)$ are solutions to the auxiliary equations:

$$\omega\partial_t(u_-) = f(u_-), \tag{3.7.14}$$

$$u_-(0) = u_-(2\pi), \tag{3.7.15}$$

$$\int_0^{2\pi} \phi'(\xi)(u_-(\xi) - \phi(\xi))\mathrm{d}\xi = 0, \tag{3.7.16}$$

$$0 = \kappa^2 D(u_+)_{xx} + f(u_+), \tag{3.7.17}$$

$$\partial_x u_+(0) = \partial_x u_+(2\pi) = 0, \tag{3.7.18}$$

$$\psi' = \begin{pmatrix} 0 & D^{-1}f_u(u_+) \\ -1 & 0 \end{pmatrix} \psi - \varepsilon \begin{pmatrix} \partial_x u_+ \\ -D^{-1}f(u_+) \end{pmatrix}, \tag{3.7.19}$$

$$\partial_x\psi(0) = \partial_x\psi(2\pi) = 0, \tag{3.7.20}$$

$$\int_0^{2\pi} |\psi(x)|^2\mathrm{d}x - 1 = 0. \tag{3.7.21}$$

Unfortunately current efforts to implement this scheme in practice have not worked. There are a number of possible reasons for this including: the slow convergence on the left hand side of the domain, the large dimension of the system of equations and a lack of good initial data. However, given the success of the scheme in computing fronts in the Swift-Hohenberg equation, we believe these problems are surmountable by using accurate enough discretizations, the correct preconditioners for solving the linear system, and by finding better initial conditions.

Chapter Four

Conclusion

4.1 Summary of Contributions

In this thesis we have presented an extension of the known theory of homoclinic snaking to defect solutions in reaction diffusion equations. We have shown that under certain general assumptions, the presence of a heteroclinic cycle generates families of contact defects which snake as a bifurcation parameter is varied. To our knowledge, these results are the first of their kind and constitute a significant contribution to the literature of homoclinic snaking. The difficulty in producing these results lies is being able to combine intuition from the bifurcation theory of heteroclinic and homoclinic connections, and spatial dynamics. The result is bifurcation diagrams with a large amount of additional structure which can be explained by considering the symmetry of the underlying reaction diffusion equations. These results also mark an unexpected discovery in the theory of spatial dynamics as we are able to find defect solutions with arbitrary background phase offset, which have not been observed prior to this work.

We have also proposed a numerical scheme that we believe should be able to solve for the contact defects we have identified in model equations such as the Brusselator. We have implemented these methods in the simpler example of the Swift-Hohenberg equation, where we are able to test the robustness of the scheme by comparing the results to other numerical methods. These results lead us to believe that this method has the ability to isolate the many degrees of freedom in the snaking problem, and solve for fronts and defects in reaction-diffusion equations.

4.2 Future Directions

The rich phenomenon of snaking of defect solutions presents many new and interesting challenges, and there are multiple directions yet to be explored in this area.

First and foremost, we wish to complete our numerical scheme to solve for both fronts and full defect solutions in the Brusselator. Beyond providing concrete evidence for our predictions, this would also give us information on the precise bifurcation structure of the snaking diagram near the saddle-nodes. In the case of localized solutions to the Swift-Hohenberg equation, Beck et al. (2009) have showed that the asymmetric solutions bifurcate at pitchforks very close to the saddle-node bifurcations. In the case of contact defects, it is not clear even what the saddle-node bifurcations of the symmetric tubular regions looks like. Our proof shows that the symmetric target and spiral defects should go through saddle-node bifurcations precisely as in the finite-dimensional case. But, our asymptotic expansions do not give us any information the comparison of the locations of these saddle-nodes, let alone the behaviour of the full tubular family. The asymmetric rung branches are also a mystery as you approach the saddle-nodes. The asymptotic expansion $c = \mathcal{O}(\Delta\kappa/L + e^{-\eta L})$ suggests that as you near the saddle-nodes, all four branches of the diagram become very close together. It is reasonable to expect that the asymmetric solutions may bifurcate from the symmetric branches, however, it is not at all clear how this might occur. It will be very interesting to see what this bifurcation structure looks like in the case of the Brusselator.

A related question is what the spectral stability of these contact defects look like. By extending the numerics used by Tzou et al. (2013), it is possible to numerically compute the temporal Floquet multipliers closest to one for the symmetric contact defects. For example, see Figure 4.1 where we plot the ten weakest Floquet spectra tracked during the continuation of the snaking diagram in AUTO. In black we plot the snaking diagram itself, with the coloured dots representing the Floquet spectra at each given horizontal cross-section of the snaking curve. There are two Floquet multipliers at one, which we expect for contact defects (Sandstede and Scheel, 2004). Also in (a) there are two multipliers which oscillate about one in phase with the snaking diagram. These should correspond to the saddle-node and pitchfork bifurcation multipliers. Surprisingly in (b) we see a third multiplier very close to one which oscillates out of step with the snaking curve. This eigenvalue is likely an interaction eigenvalue produced by the gluing of heteroclinic fronts and backs similar to those found in Makrides and Sandstede (2019). A second surprising observation is that the bifurcation multipliers can be seen crossing into the absolute spectrum of the patterns, which are marked by the multipliers that form logarithmic looking curves. An extension of the analysis by Makrides and Sandstede (2019) shows that this is not possible for snaking of localized solutions in PDEs without conservative structure. This apparent mismatch with the finite-dimensional intuition, as well as the mystery of the stability of the asymmetric defects, poses a very interesting and open problem.

Finally, we also believe that it is possible that other types of defects are able to form snaking bifurcations. Numerical studies by De Wit et al. (1996) and Perraud et al. (1993), also of the Brusselator, show defect solutions which are asymptotic to outwardly propagating wavetrains. These patterns constitute source defects which have different geometric properties than contact defects (Sandstede and Scheel, 2004). De Wit et al. (1996) are able to find source defects corresponding to both fronts, spiral and target defects, as seen in Figure 4.2. They also observe source defects with core regions of different widths, speaking strongly to the possibility of

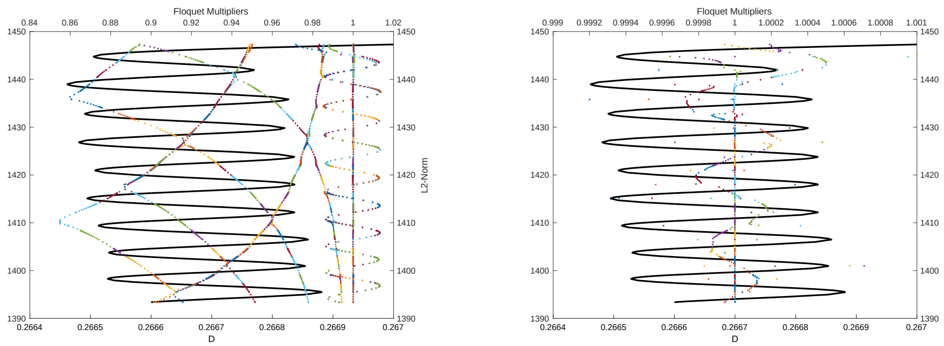

Figure 4.1: Numerically computed Floquet spectra corresponding the snaking bifurcation curve in black. (a) Shows all 10 weakest spectra. (b) Shows a zoom in on a narrow interval around the Floquet multipliers at 1.

snaking in this context as well. Assuming one can find snaking bifurcations in this context, the difference in the geometry of source defect will likely mean that that the bifurcations look different to the contact defect case. In particular, we do not expect to find families parameterised by the phase offset.

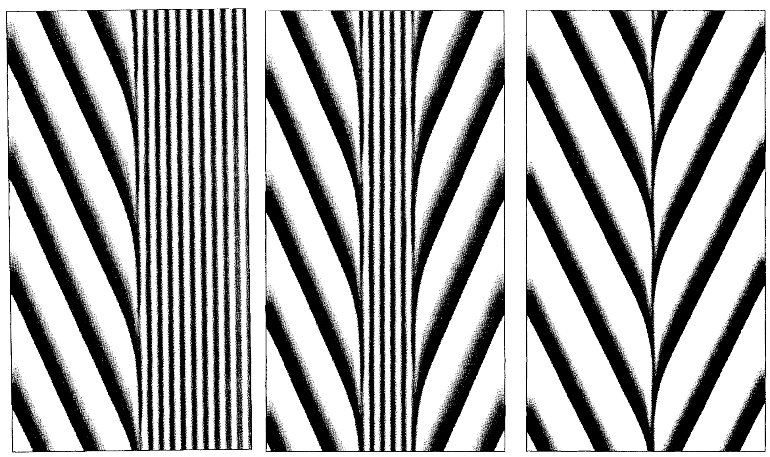

Figure 4.2: Numerical solutions computed in the Brusselator by Perraud et al. (1993). (a) A source defect front. (b) A source defect target pattern. (c) A source defect spiral pattern.

Bibliography

T. Aougab, M. Beck, P. Carter, S. Desai, B. Sandstede, M. Stadt, and A. Wheeler. Isolas Versus Snaking of Localized Rolls. *J Dyn Diff Equat*, 31(3):1199–1222, Sept. 2019. ISSN 1040-7294, 1572-9222. doi: 10.1007/s10884-017-9624-0.

J. F. G. Auchmuty and G. Nicolis. Bifurcation Analysis of Nonlinear Reaction-Diffusion Equations—I. Evolution Equations and the Steady State Solutions. *Bulletin of Mathematical Biology*, 37:323–365, Mar. 1975. ISSN 0092-8240. doi: 10.1016/S0092-8240(75)80036-X.

D. Avitabile. Numerical Computation of Coherent Structure in Spatially-Extended Systems. In *Second International Conference on Mathematical Neuroscience*, Antibes Juan- les-Pins, 2016.

D. Avitabile, D. J. B. Lloyd, J. Burke, E. Knobloch, and B. Sandstede. To Snake or Not to Snake in the Planar Swift–Hohenberg Equation. *SIAM J. Appl. Dyn. Syst.*, 9(3):704–733, Jan. 2010. ISSN 1536-0040. doi: 10.1137/100782747.

P. Ball. Forging Patterns and Making Waves from Biology to Geology: A Commentary on Turing (1952) 'The Chemical Basis of Morphogenesis'. *Philosophical Transactions of the Royal Society B: Biological Sciences*, 370(1666):20140218, Apr. 2015. doi: 10.1098/rstb.2014.0218.

M. Beck, J. Knobloch, D. J. B. Lloyd, B. Sandstede, and T. Wagenknecht. Snakes, Ladders, and Isolas of Localized Patterns. *SIAM J. Math. Anal.*, 41(3):936–972, Jan. 2009. ISSN 0036-1410, 1095-7154. doi: 10.1137/080713306.

J. Burke and E. Knobloch. Localized States in the Generalized Swift-Hohenberg Equation. *Phys. Rev. E*, 73(5):056211, May 2006. doi: 10.1103/PhysRevE.73.056211.

J. Burke and E. Knobloch. Snakes and Ladders: Localized States in the Swift–Hohenberg Equation. *Physics Letters A*, 360(6):681–688, Jan. 2007a. ISSN 0375-9601. doi: 10.1016/j.physleta.2006.08.072.

J. Burke and E. Knobloch. Homoclinic Snaking: Structure and Stability. *Chaos: An Interdisciplinary Journal of Nonlinear Science*, 17(3):037102, Sept. 2007b. ISSN 1054-1500. doi: 10.1063/1.2746816.

J. Burke and E. Knobloch. Multipulse States in the Swift-Hohenberg Equation. *PROC*, 2009(Special):109–117, 2009. ISSN 0133-0189. doi: 10.3934/proc.2009.2009.109.

A. Champneys, Yu. A. Kuznetsov, and B. Sandstede. A NUMERICAL TOOLBOX FOR HOMOCLINIC BIFURCATION ANALYSIS. *Int. J. Bifurcation Chaos*, 06(05):867–887, May 1996. ISSN 0218-1274, 1793-6551. doi: 10.1142/S0218127496000485.

A. R. Champneys. Homoclinic Orbits in Reversible Systems and Their Applications in Mechanics, Fluids and Optics. *Physica D: Nonlinear Phenomena*, 112(1):158–186, Jan. 1998. ISSN 0167-2789. doi: 10.1016/S0167-2789(97)00209-1.

S. Chapman and G. Kozyreff. Exponential Asymptotics of Localised Patterns and Snaking Bifurcation Diagrams. *Physica D: Nonlinear Phenomena*, 238(3):319–354, Feb. 2009. ISSN 01672789. doi: 10.1016/j.physd.2008.10.005.

M. C. Cross and P. C. Hohenberg. Pattern Formation Outside of Equilibrium. *Rev. Mod. Phys.*, 65(3):851–1112, July 1993. ISSN 0034-6861, 1539-0756. doi: 10.1103/RevModPhys.65.851.

A. De Wit, D. Lima, G. Dewel, and P. Borckmans. Spatiotemporal Dynamics near a Codimension-Two Point. *Phys. Rev. E*, 54(1):261–271, July 1996. ISSN 1063-651X, 1095-3787. doi: 10.1103/PhysRevE.54.261.

R. L. Devaney. Homoclinic Orbits in Hamiltonian Systems. *Journal of Differential Equations*, 21(2):431–438, July 1976. ISSN 0022-0396. doi: 10.1016/0022-0396(76)90130-3.

R. L. Devaney. Blue Sky Catastrophes in Reversible and Hamiltonian Systems. *Indiana University Mathematics Journal*, 26(2):247–263, 1977. ISSN 0022-2518.

F. Dias and G. Iooss. Capillary-Gravity Interfacial Waves in Infinite Depth. *European Journal of Mechanics B, Fluids*, 15(3):367–393, 1996. ISSN 0997-7546.

S. Dodson and B. Sandstede. Determining the Source of Period-Doubling Instabilities in Spiral Waves. *SIAM J. Appl. Dyn. Syst.*, 18(4):2202–2226, Jan. 2019. doi: 10.1137/19M1264813.

A. Doelman, B. Sandstede, A. Scheel, and G. Schneider. The Dynamics of Modulated Wave Trains. *Memoirs of the American Mathematical Society*, 199, May 2009. doi: 10.1090/memo/0934.

I. R. Epstein. Nonlinear Oscillations in Chemical and Biological Systems. *Physica D: Nonlinear Phenomena*, 51(1):152–160, Aug. 1991. ISSN 0167-2789. doi: 10.1016/0167-2789(91)90228-2.

G. Ertl. Oscillatory Kinetics and Spatio-Temporal Self-Organization in Reactions at Solid Surfaces. *Science*, 254(5039):1750–1755, Dec. 1991. ISSN 0036-8075, 1095-9203. doi: 10.1126/science.254.5039.1750.

N. Fenichel. Geometric Singular Perturbation Theory for Ordinary Differential Equations. *Journal of Differential Equations*, 31(1):53–98, Jan. 1979. ISSN 0022-0396. doi: 10.1016/0022-0396(79)90152-9.

L. Glass. Dynamics of Cardiac Arrhythmias. *Physics Today*, 49(8):40–45, Aug. 1996. ISSN 0031-9228, 1945-0699. doi: 10.1063/1.881510.

J. Härterich. Cascades of Reversible Homoclinic Orbits to a Saddle-Focus Equilibrium. *Physica D: Nonlinear Phenomena*, 112(1):187–200, Jan. 1998. ISSN 0167-2789. doi: 10.1016/S0167-2789(97)00210-8.

G. Iooss and M. C. Peroueme. Perturbed Homoclinic Solutions in Reversible 1:1 Resonance Vector Fields. *Journal of Differential Equations*, 102(1):62–88, Mar. 1993. ISSN 0022-0396. doi: 10.1006/jdeq.1993.1022.

G. Jaramillo and A. Scheel. Deformation of Striped Patterns by Inhomogeneities. *Math. Meth. Appl. Sci.*, 38(1):51–65, Jan. 2015. ISSN 01704214. doi: 10.1002/mma.3049.

C. K. R. T. Jones, T. J. Kaper, and N. Kopell. Tracking Invariant Manifolds up to Exponentially Small Errors. *SIAM J. Math. Anal.*, 27(2):558–577, Mar. 1996. ISSN 0036-1410, 1095-7154. doi: 10.1137/S003614109325966X.

H. Kidachi. On Mode Interactions in Reaction Diffusion Equation with Nearly Degenerate Bifurcations. *Progress of Theoretical Physics*, 63(4):1152–1169, Apr. 1980. ISSN 0033-068X. doi: 10.1143/PTP.63.1152.

J. Knobloch and T. Wagenknecht. Snaking of Multiple Homoclinic Orbits in Reversible Systems. *SIAM J. Appl. Dyn. Syst.*, 7(4):1397–1420, Jan. 2008. ISSN 1536-0040. doi: 10.1137/070695800.

B. Krauskopf and T. Rieß. A Lin's Method Approach to Finding and Continuing Heteroclinic Connections Involving Periodic Orbits. *Nonlinearity*, 21(8):1655–1690, Aug. 2008. ISSN 0951-7715, 1361-6544. doi: 10.1088/0951-7715/21/8/001.

K. J. Lee. Wave Pattern Selection in an Excitable System. *PHYSICAL REVIEW LETTERS*, 79(15), 1997.

K. J. Lee, E. C. Cox, and R. E. Goldstein. Competing Patterns of Signaling Activity in *Dictyostelium Discoideum*. *Phys. Rev. Lett.*, 76(7):1174–1177, Feb. 1996. ISSN 0031-9007, 1079-7114. doi: 10.1103/PhysRevLett.76.1174.

D. J. B. Lloyd and A. Scheel. Continuation and Bifurcation of Grain Boundaries in the Swift–Hohenberg Equation. *SIAM J. Appl. Dyn. Syst.*, 16(1):252–293, Jan. 2017. ISSN 1536-0040. doi: 10.1137/16M1073212.

D. J. B. Lloyd, B. Sandstede, D. Avitabile, and A. R. Champneys. Localized Hexagon Patterns of the Planar Swift–Hohenberg Equation. *SIAM J. Appl. Dyn. Syst.*, 7 (3):1049–1100, Jan. 2008. ISSN 1536-0040. doi: 10.1137/070707622.

E. Makrides and B. Sandstede. Existence and Stability of Spatially Localized Patterns. *Journal of Differential Equations*, 266(2-3):1073–1120, Jan. 2019. ISSN 00220396. doi: 10.1016/j.jde.2018.07.064.

S. McCalla and B. Sandstede. Snaking of Radial Solutions of the Multi-Dimensional Swift–Hohenberg Equation: A Numerical Study. *Physica D: Nonlinear Phenomena*, 239(16):1581–1592, Aug. 2010. ISSN 01672789. doi: 10.1016/j.physd.2010.04.004.

A. Mielke. *A Spatial Center Manifold Approach to Steady State Bifurcations from Spatially Periodic Patterns*. Pitman Res. Notes Math Ser. 352. Longman, Harlow, UK, Aug. 1996.

D. Morrissey and A. Scheel. Characterizing the Effect of Boundary Conditions on Striped Phases. *SIAM J. Appl. Dyn. Syst.*, 14(3):1387–1417, Jan. 2015. ISSN 1536-0040. doi: 10.1137/15M1012554.

J.-J. Perraud, A. De Wit, E. Dulos, P. De Kepper, G. Dewel, and P. Borckmans. One-Dimensional "Spirals": Novel Asynchronous Chemical Wave Sources. *Phys. Rev. Lett.*, 71(8):1272–1275, Aug. 1993. ISSN 0031-9007. doi: 10.1103/PhysRevLett.71.1272.

D. Peterhof, B. Sandstede, and A. Scheel. Exponential Dichotomies for Solitary-Wave Solutions of Semilinear Elliptic Equations on Infinite Cylinders. *Journal of Differential Equations*, 140(2):266–308, Nov. 1997. ISSN 00220396. doi: 10.1006/jdeq.1997.3303.

B. Sandstede and A. Scheel. Defects in Oscillatory Media: Toward a Classification. *SIAM J. Appl. Dyn. Syst.*, 3(1):1–68, Jan. 2004. ISSN 1536-0040. doi: 10.1137/030600192.

B. Sandstede and A. Scheel. Spiral Waves: Linear and Nonlinear Theory. *Memoirs of the AMS*, 285(1413), May 2023. ISSN 0065-9266, 1947-6221. doi: 10.1090/memo/1413.

B. Sandstede, A. Scheel, ,Department of Mathematics, The Ohio State University, Columbus, OH 43210, and ,Department of Mathematics, University of Minnesota, Minneapolis, MN 55455. Evans Function and Blow-up Methods in Critical Eigenvalue Problems. *Discrete & Continuous Dynamical Systems - A*, 10(4):941–964, 2004. ISSN 1553-5231. doi: 10.3934/dcds.2004.10.941.

S. Schecter. Exchange Lemmas 1: Deng's Lemma. *Journal of Differential Equations*, 245(2):392–410, July 2008a. ISSN 00220396. doi: 10.1016/j.jde.2007.08.011.

S. Schecter. Exchange Lemmas 2: General Exchange Lemma. *Journal of Differential Equations*, 245(2):411–441, July 2008b. ISSN 00220396. doi: 10.1016/j.jde.2007.10.021.

A. M. Turing. The Chemical Basis of Morphogenesis. *Philosophical Transactions of the Royal Society of London. Series B, Biological Sciences*, 237(641):37–72, Jan. 1997. doi: 10.1098/rstb.1952.0012.

J. J. Tyson. Some Further Studies of Nonlinear Oscillations in Chemical Systems. *The Journal of Chemical Physics*, 58(9):3919–3930, Aug. 2003. ISSN 0021-9606. doi: 10.1063/1.1679748.

J. C. Tzou, Y.-P. Ma, A. Bayliss, B. J. Matkowsky, and V. A. Volpert. Homoclinic Snaking near a Codimension-Two Turing-Hopf Bifurcation Point in the Brusselator Model. *Phys. Rev. E*, 87(2):022908, Feb. 2013. ISSN 1539-3755, 1550-2376. doi: 10.1103/PhysRevE.87.022908.

A. Vanderbauwhede and B. Fiedler. Homoclinic Period Blow-up in Reversible and Conservative Systems. *Z. angew. Math. Phys.*, 43(2):292–318, Mar. 1992. ISSN 0044-2275, 1420-9039. doi: 10.1007/BF00946632.

P. D. Woods and A. R. Champneys. Heteroclinic Tangles and Homoclinic Snaking in the Unfolding of a Degenerate Reversible Hamiltonian–Hopf Bifurcation. *Physica D: Nonlinear Phenomena*, 129(3):147–170, May 1999. ISSN 0167-2789. doi: 10.1016/S0167-2789(98)00309-1.